UNIVERSITY OF CALIFORNIA, SAN DIEGO

Infrared study of exotic phases in matter

A dissertation submitted in partial satisfaction of the
requirements for the degree
Doctor of Philosophy

in

Physics

by

Kirk William Post

Committee in charge:

Professor Dimitri N. Basov, Chair
Professor Zhaowei Liu
Professor Brian Maple
Professor Oleg Shpyrko
Professor Michael Tauber

2017

The dissertation of Kirk William Post is approved, and it is acceptable in quality and form for publication on microfilm and electronically:

_____

_____

_____

_____

_____

Chair

University of California, San Diego

2017

DEDICATION

JN

EPIGRAPH

viva la raza

TABLE OF CONTENTS

LIST OF FIGURES

LIST OF TABLES

ACKNOWLEDGEMENTS

Graduate school is typically thought to be a period of life that drains a students sanity. Although this is not entirely incorrect, I have been fortunate to have an incredible infrastructure of friends and mentors who have, along with the beautiful city of San Diego and its bountiful beaches, surf breaks and breweries, made these past seven years far more enriching than I had optimistically anticipated.

- Foremost among these is my advisor, Dmitri Basov, who has always been both exceedingly patient and supportive with a graduate student who (almost) overstayed his welcome.

- Alex McLeod, thank you for teaching me everything I know about SNOM, and a great deal about many other things.

- Brian Chapler, who was always willing to talk about physics, and life in general. Without your guidance I would still be sitting in the middle of the lab, looking around in confusion.

- Alex Schafgans, who taught me to the use both the bruker, and the magnet, and introduced me to topological insulators (for better or worse).

- Michael Goldflam, both an excellent (and tolerant) officemate, and physicist who would not let a problem remain unsolved.

- Erica Carlson and Yifan Wang, It has been a great pleasure working with you, and learning all that can be extracted from nanoscale images of phase transitions through numerous and highly enlightening discussions.

- Ted Stinson and Alex Frenzel, thank you for numerous conversations over coffee, whiskey and beer, about all the important things in life.

- Meigan Aronson, thank you for your guidance and experimental insights; It was always interesting to talk to you and your group members.

- Alexander Goncharov, for showing an inexperienced third year graduate student, how to use a diamond anvil cell, and produce some remarkable results in the process.

- Our collaborators in Germany, including Eva Benckiser and Matthias Hepting. Among the work I've done as a graduate student, that which I am most proud of was enabled by your excellent samples and insightful discussions.

- Antonio Delgado, Although I disregarded your advice and became an experimental condensed matter physicist; your encouragement was always as inspiring, as your class was challenging.

- Deborah Brunt, thank you for believing that I could be a physicist before me. Perhaps I can vindicate your opinion one day.

- Melissa Buck, it was in your class, many years ago, that I learned about Richard Feynman and decided to be a physicist.

In addition to these, many people have not been directly involved in my physics research, but have been an integral part of life.

- Ben Anderson, who despite living across the country has always been present.

- Dan Lenzen, you've never held back an opinion, especially if it contradicts mine.

- Logan Swartz, you might not have been the best surf instructor, but you were the only one I had.

- Brian Shotwell, thank you for putting up with me for so many years, patiently teaching me Spanish, and occasionally high energy physics.

- Eric Geier, we are going to Coachella next year!

And lastly my family, to whom I am eternally grateful,

- Kim and Brent, You have always been there, often at very odd hours when you are needed most. I cannot express how grateful I am that you are my parents, and how encouraging you've been throughout my life, and in particular, these past 25 years of school.

- Maygan, thank you for paving the way, and doing it with such panache, and helping me to become an adult, despite being a 30 year old student.
- Kollen, thank you for undoing all of Maygan's hard work.
- Katherine, you are the type of human I aspire to be.

Chapter 2 is a reprint of material published in *Physical Review B* **88**, 0715121 (2013). K.W. Post, B.C. Chapler, Liang He, Xufeng Kou, Kang L. Wang, and D.N. Basov. The dissertation author was the primary researcher and author of this material.

Chapter 3 is a reprint of material published in *Physical Review B* **91**, 165202 (2015). K.W. Post, Y.S. Lee, B.C. Chapler, A.A. Schafgans, Mario Novak, A.A. Taskin, Kouji Segawa, M.D. Goldflam, H.T. Stinson, Yoichi Ando and D.N. Basov. The dissertation author was the primary researcher and author of this material.

Chapter 4 is a reprint of material published in *Physical Review Letters* **115**, 116804 (2015). K.W. Post, B.C. Chapler, M.K. Liu, J.S. Wu, H.T. Stinson, M.D. Goldflam, A.R. Richardella, J.S. Lee, A.A. Reijnders, K.S. Burch, M.M. Fogler, N. Samarth, and D.N. Basov. The dissertation author was the primary researcher and author of this material.

Chapter 5 is a reprint of material published in *Physical Review B* **94**, 045115 (2016). K.W. Post, Alexander F. Goncharov, Z.P. Yin, J.W. Simonson, Jing Guo, Liling Sun, S. Zellman, M.D. Goldflam, H.T. Stinson, B.C. Chapler, D.E. McNally, Zhongxian Zhao, G. Kotliar, M.C. Aronson, and D.N. Basov. The dissertation author was the primary researcher and author of this material.

Chapter 6 is a reprint of material in preparation for publication. K.W. Post, A.S. McLeod, M. Hepting, M. Blushke, Yifan Wang, G. Cristiani, G. Logvenov, A. Charnukha, A. Pasupathy, A.V. Boris, E. Benckiser, K.A. Dahmen, E.W. Carlson, B. Keimer, and D.N. Basov. The dissertation author was the primary researcher and author of this material.

VITA

2010	B. S. in Physics, University of Notre Dame
2010-2017	Research Assistant, University of California, San Diego
2013	M. S. in Physics, University of California, San Diego
2017	Ph. D. in Physics, University of California, San Diego

PUBLICATIONS

Yinming Shao, **K.W. Post**, Jhih-Sheng Wu, Siyuan Dai, Alex J. Frenzel, Anthony R. Richardella, Joon Sue Lee, Nitin Samarth, Michael M. Fogler, Alexander V. Balatsky, Dmitri E. Kharzeev, and D.N. Basov, "Faraday Rotation Due to Surface States in the Topological Insulator $(Bi_{1-x}Sb_x)_2Te_3$," *Nano Letters* **17**, 980 (2017)

Jingdi Zhang, Xuelian Tan, Mengkun Liu, S.W. Teitelbaum, **K.W. Post**, Feng Jin, K.A. Nelson, D.N. Basov, Wenbin Wu, and R.D. Averitt, "Cooperative photoinduced metastable phase control in strained manganite films," *Nature Materials* **15**, 956 (2016)

K.W. Post, Alexander F. Goncharov, Z.P. Yin, J.W. Simonson, Jing Guo, Liling Sun, S. Zellman, M.D. Goldflam, H.T. Stinson, B.C. Chapler, D.E. McNally, Zhongxian Zhao, G. Kotliar, M.C. Aronson, and D.N. Basov, "Electronic correlations and pressure induced metallicity in $LaMnPO_{1-x}F_x$ revealed via infrared spectroscopy," *Phys. Rev. B* **94**, 045115 (2016)

A. Charnukha, **K.W. Post**, S. Thirupathaiah, D. Pröpper, S. Wurmehl, M. Roslova, I. Morozov, B. Büchner, A.N. Yaresko, A.V. Boris, S.V. Borisenko and D.N. Basov, "Weak-coupling superconductivity in a strongly correlated iron pnictide," *Sci. Rep.* **6**, 18620 (2016)

Z. Fei, M.D. Goldflam, J.-S. Wu, S. Dai, M. Wagner, A.S. McLeod, M.K. Liu, **K.W. Post**, S. Zhu, G.C.A.M. Janssen, M.M. Fogler, and D.N. Basov, "Edge and Surface Plasmons in Graphene Nanoribbons," *Nano Letters* **15**, 8271 (2015)

D.E. McNally, S. Zellman, Z.P. Yin, **K.W. Post**, Hua He, K. Hao, G. Kotliar, D. Basov, C.C. Homes, and M.C. Aronson, "From Hund's insulator to Fermi liquid: Optical spectroscopy study of K doping in $BaMn_2As_2$," *Phys. Rev. B* **92**, 115142 (2015)

K.W. Post, B.C. Chapler, M.K. Liu, J.S. Wu, H.T. Stinson, M.D. Goldflam, A.R. Richardella, J.S. Lee, A.A. Reijnders, K.S. Burch, M.M. Fogler, N. Samarth, and D.N. Basov, "Sum rule constraints on the surface state conductance of topological insulators," *Phys. Rev. Lett.* **115**, 116804 (2015)

M.D. Goldflam, G.X. Ni, **K.W. Post**, Z. Fei, Y. Yeo, J.Y. Tan, A.S. Rodin, B.C. Chapler, Barbaros Özyilmaz, Antonio H. Castro-Neto, Michael M. Fogler, and D.N. Basov, "Tuning and persistent switching of graphene plasmons on a ferroelectric substrate," *Nano Letters* **15**, 4859 (2015)

K.W. Post, Y.S. Lee, B.C. Chapler, A.A. Schafgans, M. Novak, A.A. Taskin, Kouji Segawa, M.D. Goldflam, H.T. Stinson, Yoichi Ando, D.N. Basov,"Infrared probe of the bulk insulating response in $Bi_{2-x}Sb_xTe_{3-y}Se_y$ topological insulator alloys," *Phys. Rev. B* **91**, 165202 (2015)

S. Zapf, C. Stingl, **K.W. Post**, J. Maiwald, N. Bach, I. Pietsch, D. Neubauer, A. Löhle, C. Clauss, S. Jiang, H.S. Jeevan, D.N. Basov, P. Gegenwart, M. Dressel, "Persistent Detwinning of Iron-Pnictide $EuFe_2As_2$ Crystals by Small External Magnetic Fields," *Phys. Rev. Lett.* **113**, 227001 (2014)

D.E. McNally, J.W. Simonson, **K.W. Post**, Z.P. Yin, M. Pezzoli, G.J. Smith, V. Leyva, C. Marques, L. DeBeer-Schmitt, Al Kolesnikov, Y. Zhao, J.W. Lynn, D.N. Basov, G. Kotliar, M.C. Aronson, "Origin of the charge gap in LaMnPO," *Phy. Rev. B* **90**, 180403 (2014)

Conor T. Riley, Tien A. Kieu, Joseph S.T. Smalley, Si Hui Athena Pan, Sung Joo Kim, **K.W. Post**, Alireza Kargar, Dimitri N. Basov, Xiaoqing Pan, Yeshaiahu Fainman, Deli Wang, Donald J. Sirbuly, "Plasmonic tuning of aluminum doped zinc oxide nanostructures by atomic layer deposition," *Physica status solidi* **8**, 948 (2014)

B.C. Chapler, **K.W. Post**, A.R. Richardella, J.S. Lee, J. Tao, N. Samarth, and D.N. Basov, "Infrared electrodynamics and ferromagnetism in the topological semiconductors Bi_2Te_3 and Mn-doped Bi_2Te_3," *Phys. Rev. B* **89**, 235308 (2014)

K.W. Post, B.C. Chapler, L. He, X. Kou, Kang L. Wang, and D.N. Basov, "Thickness-dependent bulk electronic properties in Bi_2Se_3 thin films revealed by infrared spectroscopy" *Phys. Rev. B* **88**, 031605 (2013)

K. Wang, Yanwen Liu, Weiyi Wang, N. Meyer, L.H. Bao, L. He, M.R. Lang, Z.G. Chen, X.Y. Chen, **K.W. Post**, J. Zou, D.N. Basov, K.L. Wang, and Faxian Xiu, "High-quality Bi_2Te_3 thin films grown on mica substrates for potential optoelectronic applications," *App. Phys. Lett.* **103**, 031605 (2013)

J.W. Simonson, G.J. Smith, **K.W. Post**, M. Pezzoli, J.J. Kistner-Morris, D.E. McNally, J.E. Hassinger, C.S. Nelson, G. Kotliar, D.N. Basov and M.C. Aronson, "Magnetic and structural phase diagram of $CaMn_2Sb_2$," *Phys. Rev. B* **86**, 184430 (2012)

J.W. Simonson, Z.P. Yin, M. Pezzoli, J. Guo, J. Liu, **K.W. Post**, A. Efimenko, N. Hollman, Z. Hu, H.-J. Lin, C.-T. Chen, C. Marques, V. Leyva, G. Smith, J.W. Lynn, L.L. Sun, G. Kotliar, D.N. Basov, L.H. Tjeng, and M.C. Aronson, "From antiferromagnetic insulator to correlated metal in pressurized and doped LaMnPO," *Proc. Nat. Acad. Sci.* **109**, E1815 (2012)

A.A. Schafgans, **K.W. Post**, A.A. Taskin, Y. Ando, X.L. Qi, B.C. Chapler, and D.N. Basov, “Landau level spectroscopy of surface state in the topological insulator $Bi_{0.91}Sb_{0.09}$ via magneto-optics," *Phys. Rev. B* **85**, 195440 (2012)

J.W. Simonson, **K.W. Post**, C. Marques, G. Smith, O. Khatib, D.N. Basov, and M.C. Aronson, “Gap state in insulating $LaMnPO_{1-x}F_x$ (x=0.0-0.3)," *Phys. Rev. B* **84**, 165129 (2011)

ABSTRACT OF THE DISSERTATION

Infrared study of exotic phases in matter

by

Kirk William Post

Doctor of Philosophy in Physics

University of California, San Diego, 2017

Professor Dimitri N. Basov, Chair

This dissertation reports on “infrared" measurements of exotic phases in condensed matter systems: topological insulators (TIs), rare earth nickelates (RENs), and the Mn-pnictides. In the first part, I will discuss the experimental interrogation of TI systems, where electrons are confined to two dimensional surface states (SS) and the bulk is anticipated to be semiconducting. To elucidate the properties of TIs, we investigated the variation of bulk properties in TIs as a function of growth parameters. Later, mathematical constraints were placed on the maximum electronic response that could be expected from the SS electrons in general TI systems, with experimental work culminating in the measurement of an infrared absorption, consistent with these expectations. Subsequent magneto-optical investigation clarified infrared response, and identified a significant contribution from the exotic significant SS. In the second part, I will discuss

the Mn-pnictide LaMnPO, which is a material highly similar to the recently discovered family of Fe-pnictide, high temperature superconductors. Guided by theoretical predictions, we used high pressures to induce a correlated metallic state, similar to the state preceding high temperature superconductivity in the Fe-pnictides. The last part of this thesis discusses recent, high resolution imaging experiments of the insulator-metal transition (IMT) in RENs. In these measurements, we revealed the discrete nature of the IMT. Additionally, we uncovered a conducting boundary between insulating, and magnetically ordered domains, which undergoes a distinct phase transition from the rest of the sample.

Chapter 1

Introduction

1.1 Topological Insulators

1.1.1 Background

Over 30 years ago, physicists began describing materials in terms of the topological differences in the band structures [1]. Only recently has the importance of this approach has been realized, as evidenced by the fact that the Nobel prize in physics of 2016, was awarded to three theorists who pioneered this idea. The key point is that a material can be characterized by a single integer, in the same way that topology distinguishes different bodies by the number of holes that they possess. For instance, a coffee cup and a donut have the same topological classification, whereas an apple is different, since it lacks the hole. Additionally, at the boundary of two topologically distinct materials, their must be gapless free carriers, with suppressed backscattering arising from coupled spin and momentum [2]. Typically, these electrons, which are confined to the interface between the materials, are called surface states (SS). It is thought that these electrons could be utilized in quantum computing, or simply to improve the efficiency of contemporary computers [3]. Originally, the topological nature of matter could only be realized under high magnetic fields and low temperatures. An early work posited a scenario where these limitations may be overcome by strong spin orbit coupling in an antiferromagnetic system [4]. An expansion of these early theories predicted numerous materials would manifest topological states of matter, possibly in ambient conditions

[5, 6]. Subsequent experiments identified the presence of the topological SS in numerous materials [7–10], coexisting with an insulating bulk, and thus brought the so-called 'topological insulators' (TI) to the forefront of condensed matter physics. However, a major obstacle to the realization of devices based on TIs has been the fact that the surface states, are a relatively weak electromagnetic response when compared to the intrinsic bulk doping that tends to plague the known topological insulators.

1.1.2 Thickness dependence of bulk electronic properties

Among the known TI materials Bi_2Se_3 emerges as the most viable for device applications because of its large band gap (0.3 eV) and the simple, Dirac-like band structure of its surface state. Despite the intense effort directed at these materials, progress has been plagued by issues with sample growth including inhomogeneous crystals, Se vacancies, and surface doping. These problems shift the Fermi level into the bulk conduction band. Measurements of the relatively weak SS properties are then often masked by the bulk dominated conductivity. Further studies of the bulk electronic properties of this material are required in order to combat the problems in sample growth.

In Chapter 2 we report on optical spectroscopy measurements of epitaxial Bi_2Se_3 thin films ranging in thickness from 15 to 99 quintuple layers (QL). Using infrared spectroscopy, we are able to extract the optical conductivity of the thin films. By studying the optical conductivity as a function of thickness, we can examine how extrinsic properties affect optical conductivity. This process reveals an increase in free carrier plasma frequency and optical energy gap as thickness decreases. A comparison of the optical conductivity to the band structure measured via photoemission reveals the existence of an impurity band below the conduction band as well as Fermi level that systematically changes with thickness. These results reveal systematic changes in the electronic properties of Bi_2Se_3 that must be addressed in the growth of future samples.

1.1.3 Bulk insulating response of topological insulator Alloys

In Chapter 3, we study the optical response, with and without external magnetic field, of two canonical bulk insulating topological insulators $Bi_{1.5}Sb_{0.5}Te_{1.7}Se_{1.3}$

and $BiSbSe_2Te$. To our knowledge, this is the first measurement of infrared optical properties of these two alloys. We find that these two materials are highly insulating, possessing some of the lowest bulk carrier densities reported for TI crystals. In addition, our infrared measurements detect critical points, which are regions where the valence and conduction band are parallel, in the $Bi_{1.5}Sb_{0.5}Te_{1.7}Se_{1.3}$. This is the first observation of critical points in any topological insulator system measured so far. Importantly, the presence of critical points suggests that $Bi_{1.5}Sb_{0.5}Te_{1.7}Se_{1.3}$ is a crystallographically ordered system, despite being an alloy, and may be a prime candidate for future TI studies. Although this work shows the effectiveness of alloying in reducing the bulk carrier concentration, it also reveals that eliminating the bulk carriers does not inherently guarantee surface dominated conductance. We offer a few possible reasons for why the surface conductance is suppressed.

1.1.4 Sum-Rule Constraints on the surface state response

An essential element of research in TI systems is distinguishing the SS response from that of the bulk. In chapter 4 we show the results of combined Terahertz time-domain and Fourier transform spectroscopies on the TI $(Bi,Sb)_2Te_3$. These results reveal a significantly reduced free carrier response, and therefore, the success of alloying in reducing the bulk carrier concentration. Indeed the identified response was smaller than any previous measurements reported in the literature. Additionally, there is a direct relationship between the Fermi energy and the free carrier response within Dirac like systems. Using this relationship, we identified the maximum response that could be anticipated solely from the SS in both generic, and specific TI systems. The response we measured in $(Bi,Sb)_2Te_3$ is consistent with that expected from SS, given the bulk energy gap that we observed. This was the first published observation of a bulk sensitive optical measurement that could be consistently ascribed to SS.

1.2 Insulator to Metal transitions

1.2.1 Background

Within the broad topic of condensed matter physics, the subject of the interactions between electrons has been of intense interest since it was discovered that NiO demonstrated strong insulating behavior, where conventional electron and orbital counting suggested metallic ground state. Sir Neville Mott was able to explain this behavior in terms of interactions between electrons, which adds an energy cost to putting two electrons onto the same atomic orbital. It is this added energy cost that opens up a gap in the band structure, leading to so called Mott insulators. Materials in which the electrons are strongly interacting, as in Mott insulators, show a plethora of exotic phenomena, including high temperature superconductivity (HTSC), colossal magnetoresistance, and insulator-metal phase transitions (IMT), to name a few [11]. In the remainder of this section, I will focus on the IMT within the context of two somewhat disparate systems.

1.2.2 Pnictides

The discovery of high temperature superconductivity (HTSC) was one of the most transformational findings in contemporary physics [12, 13]. For almost twenty years, the cuprates were the only family of material found to host this exotic phenomena. However, there was a rapid paradigm shift when superconductivity was discovered in the Fe-pnictide compounds [14–16], which have recently been found with critical temperatures exceeding 100K [17]. A tremendous amount of research has been devoted to indentifying the common feature between these two disparate materials that gives rise to HTSC. One generic shared feature of these two materials is the presence of electronic correlations, which enhance the carrier mass when compared to the simple density functional theory (DFT) picture [18, 19]. Interestingly, the Fe-based compounds have a metallic ground state, whereas the cuprates parent compounds are insulating. Accordingly, it may be instructive to look at compounds similar to the Fe-pnictide superconductors, where the ground state is insulating, and try to induce a correlated metallic state. One such class of materials are the Mn-pnictides, which host structural and magnetic ordering similar to the pnictides, yet are strong insulators. In Chapter 5, we have probed

the electronic structure of $LaMnPO_{1-x}F_x$ using optical spectroscopy at high pressures and high temperatures, in order to elucidate the character of the ground state.

From these measurements, we unambiguously establish the nature of the electron correlations in $LaMnPO_{1-x}F_x$ by comparing pressure and temperature dependent infrared measurements to density functional theory, augmented with dynamical mean field theory (DFT+DMFT), which included the electron-electron interactions via Hubbard U and Hund's coupling J_H. Second, our high-pressure measurements show a systematic collapse of the bulk energy gap with increasing pressure, yielding a metallic state that is theoretically anticipated to host strong electron correlations. Moreover, the insulator to metal transition observed at high pressure is decoupled from both the structural and magnetic transitions in this material and thus can be definitively attributed to an increase in the electronic bandwidth. To our knowledge, this is the first work to 1) directly compare DFT+DMFT predictions to experimental data at both high pressures and high temperatures and 2) to show a pressure induced band gap collapse in a Mn-pnictide. These results yield an accurate description of the electronic correlations in $LaMnPO_{1-x}F_x$ and identify the nature of the insulator to metal transition.

1.2.3 Rare Earth Nickelates

The rare earth nickelates ($RNiO_3$) are a class of part of the broader class of perovskite oxides, where the transition metal resides in the center of on oxygen octahedra, which surround a rare earth cation. At high temperatures, the $RNiO_3$ form in an orthorhombic structure undergo a monoclinic distortion at a temperature commensurate with the IMT, indicating the connection between structural and electronic properties. Additionally, the temperature at which the IMT occurs (T_{IMT}) can be tuned by adjusting the size of the rare earth ion (R), with smaller R leading to higher T_{IMT} and larger R reducing T_{IMT}. In the case of R=La, the IMT is completely suppressed and $LaNiO_3$ remains metallic at all temperatures. The connection is alternatively understood as a modification to the orbital overlap of the Ni $3d$ and O $2p$ bonds, with smaller R reducing the overlap and thereby enhancing the insulating state. Accordingly, it was initially thought that the IMT was simply a result of the structural transition, which reduced the orbital overlap to such an extent that an insulating state was induced [20]. Additionally,

there is also an interesting, unit cell quadrupling, antiferromagnetic (AF) order, which onsets at the IMT in the case of *R*=Ni,Pr, or at. Notably, when the IMT is commensurate with the AF order, the transition shows first order behavior, whereas it is second order when they emerge seperately. Recent developements in epitaxial growth of $R\mathrm{NiO_3}$ thin films has revived research in this field. Among the contemporary discoveries, more complex mechanisms behind the IMT have been posited, which involve strong electron interactions [21, 22] and potentially new, and exotic phase transitions [23]. The interplay between between AF, and charge order in the IMT is also being explored [24]. Beyond the complexity inherent to the IMT, the $R\mathrm{NiO_3}$ system has been shown to be highly tunable through heterostucturing, and epitaxial strain [25]. Theoretical models have even suggested the possibility of tuning to a superconducting, or topologically non-trivial state [26–28]

Despite the intense interest in this system, derived from the complex interplay of electronic, magnetic and structural degrees of freedom, the nature of the low enegy electronic structure amidst the phase transition has remained unresolved. Accordingly, to resolve this omission in the literature, we have measured the electronic properties of $\mathrm{NdNiO_3}$ with nanometer resolution using near field optical microscopy, as described in Chapter 6. From the local information, we have established that the bulk IMT in $\mathrm{NdNdO_3}$ is ideally first order, in that the local electronic properties transition discretely from the insulating state, to the metallic state, in contrast to other related oxides [29, 30]. Despite the discrete transition in the bulk o fthe material, conducting domain walls (DW) were observed, which were found to undergo a continuous, second order type IMT. These results were interpretted within the framework of a Landau free energy, with coupled AF and CO. This analysis could consistently ascribe these DW arise to boundaries between AF domains of different orientation. These results may help to clarify the relevence of AF in the IMT of $\mathrm{NdNiO_3}$. More importantly, this is only the second realization of conducting DW existing in an AF insulating matrix, and the only known observation of coexisting first and second order phase transitions within the same material.

Chapter 2

Thickness dependent bulk electronic properties in Bi_2Se_3 thin films revealed by infrared spectroscopy

Abstract

We have investigated the electronic structure of Bi_2Se_3 epitaxial thin films with thicknesses between 15 and 99 quintuple layers (QL) on a Si substrate using a combination of variable angle spectroscopic ellipsometry (VASE) and infrared transmission spectroscopy. The results we have obtained are consistent with a Fermi level that shifts relative to the conduction band as a function of sample thickness. We also present evidence that the bulk energy gap in these thin films is as much as 0.1 eV smaller than the value of 0.3 eV predicted by band structure calculations and confirmed by photoemission experiments. The thickness dependence of material properties in Bi_2Se_3 observed in this work reveal thickness to be a parameter that can be tuned to control and possibly optimize the bulk properties of Bi_2Se_3 thin films.

2.1 Introduction

Topological insulators (TIs) are materials that have spin polarized, topologically protected surface states (TPSS) with Dirac-like dispersion yet are insulating in the bulk [2, 5, 6, 31, 32]. A number of materials have been identified as TIs via photoemission and scanning tunneling microscopy experiments [7, 33–35]. Among the currently known TI materials, Bi_2Se_3 emerges as the most viable material for device applications. It is a stoichiometric material and among all known TIs, it has the largest band gap with a TPSS band structure that most closely resembles a simple Dirac cone with the Dirac point lying directly above the valence band valley [2]. Furthermore, theory has predicted that Bi_2Se_3 is an insulator with the Fermi level (μ_F) lying directly at the Dirac point [36]. In practice, these materials are n-doped with μ_F positioned in the conduction band likely because of anti-site doping via Se vacancies [37]. The net result is that the exotic properties of the TPSS are masked by the bulk conduction.

2.2 Materials and Methods

Molecular beam epitaxy (MBE) is a promising method for improving sample quality and resolving the issue of unintentional doping in TI candidate materials because the growth process is precisely controlled [38–43]. However, even with the high level of control attained in MBE growth, samples grown using this method have been plagued by high carrier densities and impurity band conduction [40]. For instance, transport measurements have found that the carrier density in Bi_2Se_3 thin films (and crystals) is inversely proportional to the square root of thickness [44]. To examine the electronic structure and dynamics as thickness is tuned, we have spectroscopically investigated Bi_2Se_3 thin films with thicknesses ranging from 15 to 99 quintuple layers (QL) using a combination of optical probes.

The Bi_2Se_3 thin films of our study were grown in an ultrahigh vacuum (UHV) system by MBE. Double-side-polished Si (111) wafers are first cleaned with the standard RCA method. Hydrofluoric acid wet etching is carried out in order to saturate the surface dangling bonds and enhance the film quality. The growth is conducted under a Se-rich environment; a nominal Se to Bi ratio of 10:1 is used so that the Se vacancy

defects are suppressed. In-situ growth dynamics are monitored by reflection high energy electron diffraction (RHEED) measurements. Sharp streaky patterns, which indicate a 2D epitaxial structure, are observed during the growth. Meanwhile, RHEED oscillations of the intensity as well as the width of the specular dot as a function of time can be observed. Each oscillation period corresponds to one QL layer of Bi_2Se_3, as shown in our previous works [40, 41]. Thus, by monitoring the RHEED oscillations, the growth rate and thin film thickness can be accurately controlled. We prepared samples with the thickness of 15, 22, 45 and 99 QL. Optical characterization of the thin films and substrates was achieved using variable angle spectroscopic elipsometry (VASE) in the range 5,000 cm^{-1} to 50,000 cm^{-1} and normal incidence transmission for the range 40 cm^{-1} to 8,000 cm^{-1}.

2.3 Results

Transmission spectra for the Bi_2Se_3 on Si substrate, are shown in Fig. 2.1. In panel (a) the transmission at 20K is displayed for the samples of thicknesses 15 QL, 22 QL, 45 QL and 99 QL. We first describe the transmission spectrum of 99QL Bi_2Se_3. The spectrum is dominated by three main features labeled in Fig. 2.1 (a) as ζ, β, and γ. ζ is the sharp dip in the transmission spectra at approximately 63 cm^{-1}, due to absorption by an infrared active phonon. The phonon is superimposed on feature β, which is the broad absorption typical of free carriers, that extends above 1000 cm^{-1}. Feature γ is the suppression of transmission at higher wavenumbers ($\omega > 1400 cm^{-1}$), and is characteristic of excitations across an energy gap. The onset energy of the γ feature at E_γ is indicated by the arrows in Fig. 2.1 (a) colored to match their respective spectra. The method for determining the E_γ is discussed later in the text. The transmission features we observed have also been seen in bulk crystals [45].

We now examine the trends of the features described above with thickness. Both β and γ structures are less pronounced in thinner samples. Transmission (T) is exponentially related to the thickness (t) and the absorption coefficient (α) of a medium via $T \propto e^{-\alpha t}$. Thus, the reduced transmission in thicker samples is expected. However, we observed that E_γ is inversely related to t. This type of systematic shift in E_γ cannot be

explained by simply changing t in the exponential equation for transmisson. Rather, this indicates α is changing with the sample thickness.

Fig. 2.1 (b) shows the transmission for the 99QL sample at four different temperatures, offset from the 295K data by 0.03. Features ζ, β and γ that were discussed previously, are observed at all temperatures. The arrows indicate E_γ for the 99QL sample at 295 K and 20 K, revealing a blue shift between the highest and lowest temperatures. In Fig. 2.1 (c), the temperature dependence of the phonon feature for the 99 QL sample is highlighted. The phonon sharpens and red shifts with decreasing temperature, similar to what was seen in reflectivity measurements on Bi_2Se_3 crystals [45, 46]. The low wavenumber transmission for the 99 QL sample is shown without offset in Fig. 2.1 (d). The transmission increases with cooling, indicating there is less absorption and therefore fewer free carriers. The temperature dependence of the transmission spectra for the 99 QL thin film, shown in Fig. 2.1 (b) through (d), is representative of the other samples.

Transmission measurements of our samples were limited to energies below the onset of interband absorption in the Si substrate at 1.2 eV. However optical spectra were extended into the visible and ultraviolet range by using the standard VASE technique in a homebuilt UHV chamber to achieve cryogenic temperatures [47]. VASE is well suited for these measurements because it is self referencing, and it is sensitive to thin films. Furthermore, it yields information on both real and imaginary parts of the dielectric constant [48]. In VASE experiments, the measured value is ρ, which is the ratio of the complex reflectance values for light polarized in the $\vec{p}$ and $\vec{s}$ directions, *i.e.* $\rho = \frac{r_p}{r_s}$. Typically this value is converted into Ψ, and Δ which are related to ρ by the equation below:

$$\rho = \frac{r_p}{r_s} = \tan\Psi e^{i\Delta}. \tag{2.1}$$

The measured values of Ψ and Δ for all samples at 20K are shown in Fig. 2.2. In the case of an infinite, isotropic, homogeneous medium, ρ can be directly inverted to obtain the complex dielectric function $\hat{\varepsilon} = \varepsilon_1 + i\varepsilon_2$. However, we measured a multilayer system, so it was necessary to model the data in order to extract the optical constants as described in [49, 50].

To model the two layer system of Bi_2Se_3 on a Si substrate, the optical constants of the Si substrate were obtained first. With the properties of the Si substrate established,

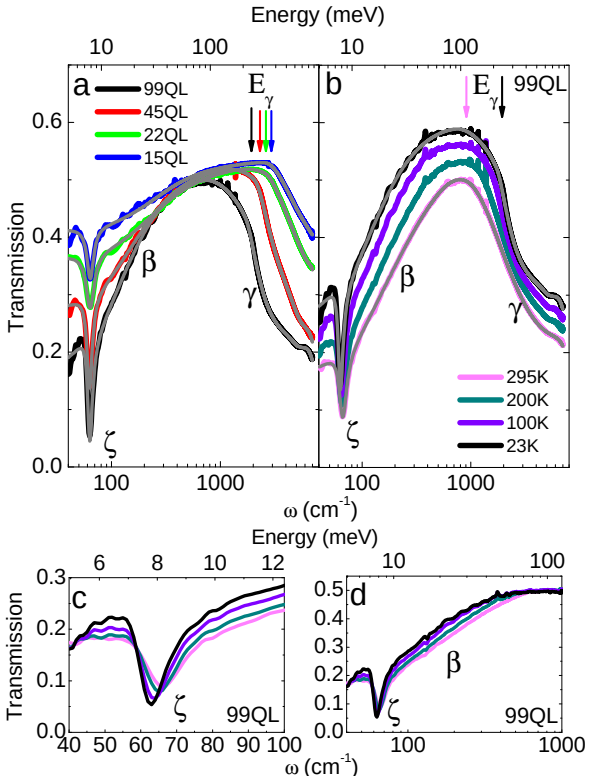

Figure 2.1: (a) Transmission spectra of Bi_2Se_3 thin films for all thicknesses at 20K. (b) Transmission of 99QL Bi_2Se_3 thin film at four temperatures with the spectra offset by 0.03 for clarity. In both plots, the modelled transmission spectra is the solid gray line overlaid on the experimental spectra. Also, the colored arrows labeled E_γ indicate the optical gap corresponding to like colored spectra. The E_γ values were via ε_2^2 analysis described later in the text. (c) Transmission spectra in the region of the phonon mode for the 99 QL sample highlighting the temperature dependence of this feature. (d) The transmission in the 99 QL sample for $\omega < 1000cm^{-1}$ without offset to more clearly show the systematic change in low ω absorption with temperature.

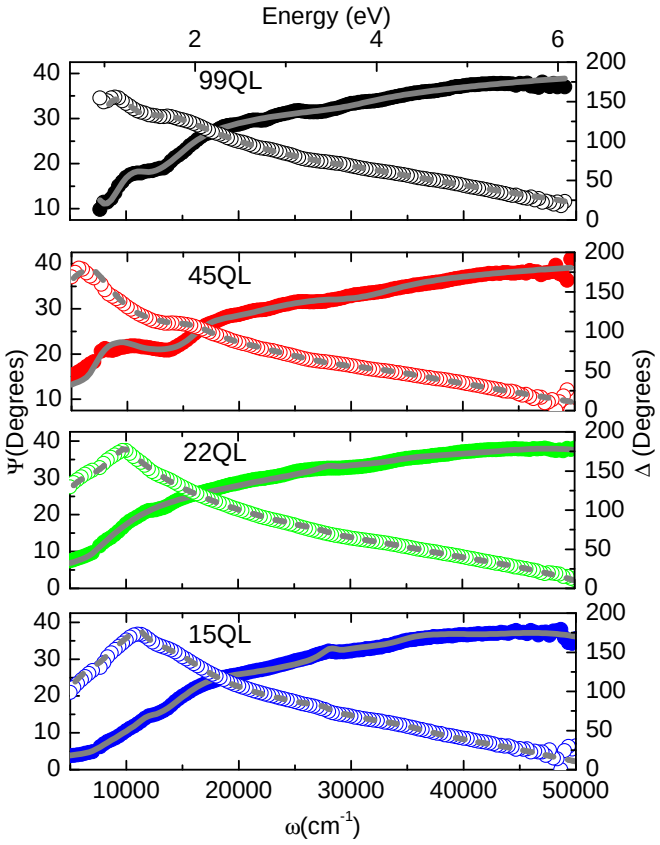

Figure 2.2: The experimental ellipsometry of the four Bi_2Se_3 sample with different thickness at 20K are shown above. The open circles correspond to the measured value of Ψ (left axis) and the solid circles correspond to the measured values of Δ (right axis). The model is the gray line on top of the experimental data

measurements of the Bi_2Se_3 thin film on Si substrate were modeled with one additional layer to capture the Bi_2Se_3 properties. The models consisted of Kramers-Kronig (KK) compatible oscillators that were simultaneously fit to reproduce both the transmission and ellipsometry data. The values of Transmission, Ψ and Δ extracted from the KK consistent model of $\hat{\varepsilon}(\omega)$ are the gray lines on top of the experimental (colored) lines in Fig. 2.1 and Fig. 2.2. The accuracy of $\hat{\varepsilon}$ is evident from the close match between the modeled values and the experimental data. The combination of VASE and transmission measurements provided a complete characterization of the optical constants of our thin films from 5 meV to 6,000 meV.

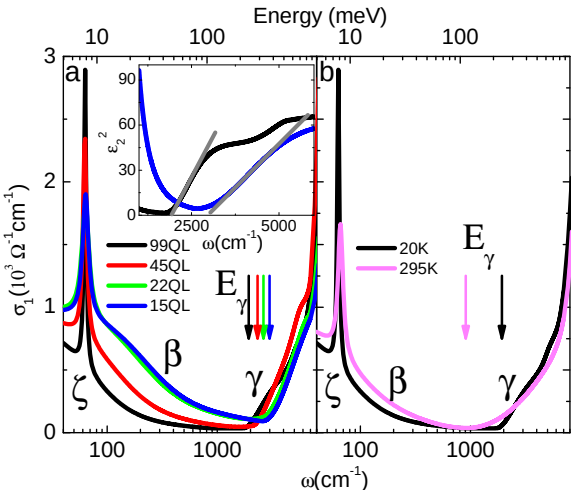

Figure 2.3: The optical conductivity of four Bi_2Se_3 thin film with varying thicknesses at 20K. The solid arrows indicate the energy gap (E_γ). The right panel shows the optical conductivity of 99QL Bi_2Se_3 at room temperature and 20K with the E_γ indicated by the arrows. The inset in the left panel shows the linear fit of ε_2^2 in the region near the band gap for determination of the direct energy gap (E_γ).

2.4 Discussion

The real part of the optical conductivity ($\sigma_1(\omega)$) was extracted from the models of $\hat{\varepsilon}$ via the relationship

$$\sigma_1 = \frac{\omega\varepsilon_2}{60\Omega}. \tag{2.2}$$

σ_1 in particular is shown because it corresponds to dissipative processes in the material. The conductivity spectra for the four samples at 20K are shown in Fig. 2.3 (a). Describing first the spectrum of the 99QL film, we see the manifestations of features ζ, β, and γ that were observed in the raw transmission spectra and have labelled them accordingly. At approximately 63 cm^{-1} the prominent peak in conductivity corresponds to ζ. The same sharp phonon resonance was also seen in reflectivity of bulk crystals [45, 46] and time domain terahertz transmission of thin films [51, 52]. There is also a broad conducting region at low ω related to feature β. The low ω optical conductivity is due to the response of free carriers and in the case of a single charge carrier contribution, it can be modelled by the equation [53]:

$$\sigma(\omega) = \frac{\omega_p^2\tau}{4\pi}\frac{1}{1-i\omega/\tau}. \tag{2.3}$$

where ω_p is the plasma frequency and $1/\tau$ is the scattering rate for the free carriers. However, in complex materials it is often impossible to fit the low-frequency intraband response with a single Drude oscillator. Instead, an effective ω_p^2 can be extracted via integration of σ_1 up to a cut off frequency (ω_c), above which there are interband contributions to σ_1 [53, 54]:

$$\frac{\pi}{2}\varepsilon_0\omega_p^2 = \int_0^{\omega_c} \sigma_1(\omega)d\omega \tag{2.4}$$

ω_p is particularly important because it is directly related to the ratio of the carrier density (n) to the effective mass (m*) via the equation:

$$\omega_p = \left(\frac{4\pi ne^2}{m^*}\right)^{1/2}. \tag{2.5}$$

We now discuss the sharp rise in optical conductivity above 1,000 cm^{-1}. This rise is a manifestion of the γ feature seen in transmission and is attributed to interband transitions. In the case of a direct band gap ($\Delta\vec{k} = 0$), $\varepsilon_2 \propto \sqrt{\omega - E_\gamma}$ where E_γ is the energy gap [55]. A linear extrapolation of ε_2^2 near the onset of feature γ shows that the interband absorption is due to a direct gap and yields the value of E_γ. The linear extrapolation of the $\varepsilon_2^2(\omega)$ spectra is shown for the 15 and 99 QL samples in the inset to Fig. 2.3. The value of E_γ determined using this procedure varies between the smallest value of 1927 cm^{-1} (0.239 eV) in the 99QL sample, to 2976 cm^{-1} (0.369 eV) in the 15 QL samples.

In Fig. 2.3 (b), the optical conductivity for the 99QL sample at 295K and 20K is shown. Optical conductivity for the intermediate temperatures is not shown because ellipsometry measurements were done only at the highest and lowest temperatures. With decreasing temperature we see a few changes to the spectra. First the Drude conductivity decreases while the ζ feature narrows and red shifts slightly. Also, the γ feature becomes more defined and E_γ blue shifts. The behavior with cooling observed in these spectra is representative of the other samples. Similar features in conductivity have been observed in bulk crystals via infrared reflectance measurements [45, 46]

Since σ_1 is a material property that is generally independent of the sample dimensions, it is natural to expect the conductivity spectra to be nominally the same for the various thicknesses of thin films that we measured. Instead we observe many significant modifications to the spectral features with thickness. To illustrate these changes,

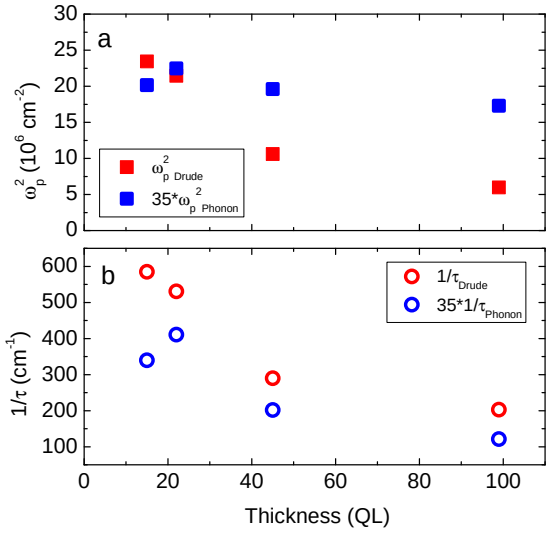

Figure 2.4: Oscillator parameters from Drude Lorentz fit of infrared spectra are shown for the samples of various thickness. The top panel shows the experimental oscillator strength for the Drude peak ($\omega^{2,Avg}_{p,Drude}$) in red and the phonon $\omega^2_{p,phonon} * 35$ in blue plotted against thickness. The dashed red line indicates the fit to ($\omega^{2,Avg}_{p,Drude}$ assuming that we are probing an average response of the sample as described in the text. The solid red line is the actual value for ω_p^2 determined from the fit.

some parameters extracted from the fitting are shown in Fig. 2.4. In Fig. 2.4 (a), the oscillator strength of both the free carriers ($\omega^2_{p,Drude}$) and the phonon ($\omega^2_{p,phonon}$) are shown. $\omega^2_{p,phonon}$ is multiplied by 35 to make it similar in magnitude to $\omega^2_{p,Drude}$ such that relative changes can be directly compared. Recently, analysis of ω_p^2 and $1/\tau$ with thickness and In doping was used to reveal surface states via Terahertz spectroscopy in Bi_2Se_3 thin films [51, 52]. What is immediately obvious is that while $\omega^2_{p,phonon}$ remains relatively constant, whereas $\omega^2_{p,Drude}$ is inversely related to the thickness. Likewise, the scattering rate for both the Drude ($1/\tau_{Drude}$) and phonon ($35 * 1/\tau_{phonon}$) are plotted in panel (b). Here we see that the scattering rate for both oscillators increases as thickness decreases. The similarity of trends seen in the scattering rate and plasma frequency with thickness indicates that the source of the free carriers is from impurity doping which is strongest in thinner samples. In this scenario, if there are more carriers, there are more defects, resulting in an enhanced scattering rate for both the phonon and the free carriers, as we observe. These results are consistent with picture described in previous works that have identified anti-site defects, *i.e.* Se vacancies, as being the primary source of

doping in Bi_2Se_3 [37].

In our analysis, we considered the possibility that TPSS impact the optical response. The presence of TPSS could be identified in optical conductivity as described in [56]. In particular, since the TPSS bands are approximately linear, interband transitions would occur near $2\mu_F$. Furthermore, theoretical analysis predicts that the conductivity resulting from transitions between the Dirac bands is 0.06 $\frac{2\pi e^2}{h}$ [56]. However, the minimum conductance we observed, for any sample, within the bulk gap region was an order of magnitude greater than the predicted conductance for transitions between the TPSS. Therefore, it was impossible to distinguish the surface states from the bulk contribution in the optical conductivity spectra. TPSS could also be identified by their unique magneto optic response that gives rise to Landau level dispersion curves [57] or quantized Faraday rotation [58, 59]. However, neither of these features were observed in magneto optic measurements of identically grown thin films on single side polished Si substrate, confirming the notion that the TPSS are overwhelmed by bulk conduction in our samples.

We also took into consideration the recently proposed possibility that there is strong band bending in the Bi_2Se_3 that shifts the conduction band (CB) relative to the Fermi level [60–63]. The result of this shift would be a carrier density (n) that decreases with distance into the sample. However, it was not possible to recover the systematic behavior of the features we observe in the free carrier response with a distance dependent n.

Prior measurements have established that the bulk energy gap (E_{bulk}) lies betweeen 0.25 and 0.35 eV depending on the Se vacancy concentration [46]. However, the most recent optical spectroscopy and ARPES measurements have consistently found that E_{bulk} is near 0.30 eV [7, 45, 46, 62, 64]. Under this framework, the expected optical gap for Bi_2Se_3 would be at least equal to the minimum bulk energy gap of 0.25 eV plus the Fermi energy relative to the bottom of the band edge (μ_F), and commonly $E_\gamma \simeq E_{bulk} + 2\mu_F$ (see Fig. 2.5). Instead $E_\gamma < 0.25$ eV was observed in the 99 QL sample. The low wavenumber conductivity reveals these samples to be conducting (*i.e.* $\mu_F > 0$) so that the $E_\gamma < E_{bulk}$ inequality is even more surprising since a non-zero μ_F would be expected to push $E_\gamma > E_{bulk}$.

Using a parabolic band approximation and the effective mass for the bulk band structure extracted from photoemission in [63], it is possible to predict the value μ_F relative to the bottom of the conduction band via the integration [65]:

$$n = \int_0^{\mu_F} \frac{1}{2\pi^2} \left(\frac{2m*}{\hbar^2} \right)^{3/2} E^{1/2} dE. \tag{2.6}$$

Since the transitions were identified as direct from the linear extrapolation of ε_2^2, we determined the energy difference for the smallest possible transitions that conserve momentum ($\vec{k}$) as depicted in Fig. 2.5 (b). The energy of these transitions predicted from the extracted μ_F, and the band structure in [63], (E_γ^{Pred}) are shown along with the measured value of E_γ in Fig. 2.5 (a). The plot reveals a strong difference between E_γ^{Pred} and E_γ especially in the 99QL sample. A possible explanation for the discrepancy between E_γ^{Pred} and E_γ could be due to a variations in E_{bulk} between samples. To explore this possibilitiy, we have also plotted the value of E_{bulk} required to explain our results (assuming a constant effective mass) in Fig. 2.5 (a). The energy gaps required to match our results were between 0.19 eV and 0.25 eV, depending on the sample. All of these values were smaller than the typically measured value of 0.3 eV [7, 45, 46, 62, 64]. The anamolously small energy gap seen in these samples could be explained by the presence of in-gap states, possibly an impurity band (IB), that lies slightly above the valence band. Transport and optics have both hinted at the existence of an IB in Bi_2Se_3 and related materials, but generally the IB has been close to the conduction band [40, 45, 46, 66–68], whereas our results indicate that the IB would lie near the valence band.

2.5 Conclusion

In conclusion, we have performed optical spectroscopy measurements from 5 meV to 6 eV on Bi_2Se_3 thin films of varying thickness. These measurements have revealed unconventional thickness dependent behavior such as increasing ω_p^2, $1/\tau$ with decreasing thickness. The simultaneous increase in ω_p^2 and $1/\tau$ is consistent with impurity doping that is strongest in thinner samples. We also find that the bulk energy gap is smaller in these thin films than the frequently cited value of 0.3 eV [7, 45, 46, 62, 64], possibly due to in-gap impurity states. These unexpected observations hint at

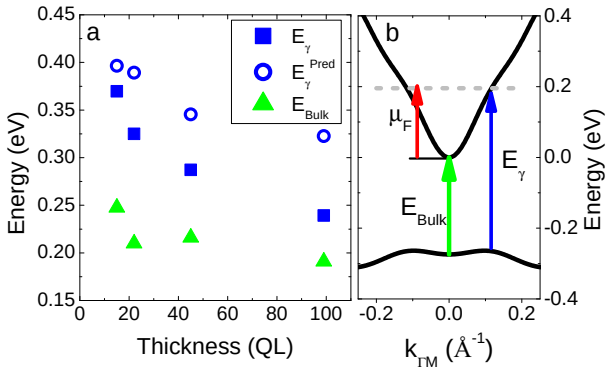

Figure 2.5: The electronic structure corresponding to oscillator fits. The left panel shows the value of E_γ^{Exp} determined from the fit of ω_p^2 and E_γ^{Pred} that was determined by combining optical data with photoemission studies. We also show the bulk energy gap (E_{bulk}) that was determined by comparing the values of E_γ^{Exp} and ω_p^2 and E_γ^{Pred} as described in the text. The overall trend is that the energy gap decreases with increasing thickness to a value substantially below the commonly measured value of 0.3 eV.

the complex behavior of the Bi_2Se_3 band structure that must be controlled to isolate the elusive surface states. Recent progress in thin film quality has been achieved using a few nanometers of capping layer to reduce surface contamination [42, 43]. It would be useful to repeat these measurements to see if the capping layer reduces the thickness dependence of the material properties.

2.6 Acknowledgements

This work at UCSD is supported by DARPA.

Chapter 2 is a reprint of material published in *Physical Review B* **88**, 0715121 (2013). K.W. Post, B.C. Chapler, Liang He, Xufeng Kou, Kang L. Wang, and D.N. Basov. The dissertation author was the primary researcher and author of this material.

Chapter 3

An infrared probe of the bulk insulating response in $Bi_{2-x}Sb_xTe_{3-y}Se_y$ topological insulator alloys

Abstract

We have investigated the electronic structure and carrier dynamics of the topological insulator $Bi_{2-x}Sb_xTe_{3-y}Se_y$, for x=0.5, y=1.3 and x=1, y=2, using infrared spectroscopy. Our results show that both of these BSTS alloys are highly insulating in the bulk, with analysis of the infrared data indicating an upper limit to the carrier density of $4.4x10^{17}$ cm^{-3}. Furthermore, analysis of the interband transitions of $Bi_{1.5}Sb_{0.5}Te_{1.7}Se_{1.3}$ revealed distinct band structure critical points, which suggest high crystallographic order of our crystals. Motivated by the low carrier density and crystallographic order identified in these compounds, we searched for the Landau level transitions associated with the surface states through magneto-optical measurements in the far infrared range. We failed to observe any indications of the Landau level resonances at fields up to 8 T in sharp contrast with our earlier finding for a related $Bi_{1-x}Sb_x$ alloy [57]. We discuss factors that may be responsible for suppressed magneto-optics response of these single crystals.

3.1 Introduction

The initial theoretical predictions [5, 6, 31, 36, 69, 70] and subsequent experimental realization [7, 8, 10, 33, 71, 72] of Dirac-like surface states (SSs) in topological insulators (TIs) has rapidly brought this new class of materials to the forefront of condensed matter physics [2, 73, 74]. The SSs in TIs are unique in that they host electrons that are resistant to direct backscattering and localization [5, 6, 31]. Moreover, SSs possess unique magnetoelectric properties that are predicted to yield a number of exotic effects, including an induced magnetic monopole, and quantized Kerr rotation [3, 58, 59, 74–76]. It has also been proposed that these numerous exotic properties of SSs could be utilized in a plethora of technologies including quantum computing, spintronics, and improving current computer technology [2].

The key to studying the exotic intrinsic properties of TIs, is isolating the SS charge carriers from the bulk response, thereby achieving SS dominated conductivity. However, SS dominated conductivity has remained elusive, being observed only in a few cases [42, 77, 78] despite the large body of work focused on this issue. More commonly, vacancies and anti-site defects push the chemical potential (μ_F) into the bulk bands [37] so that the relatively weak SS conduction is masked by bulk dopants. One method for overcoming this issue is to combine n-type TIs (Bi_2Se_3 and Bi_2Te_3) with the p-type TI Sb_2Te_3 in alloys of form $Bi_{2-x}Sb_xTe_{3-y}Se_y$ [79–81], such that the p and n type defects compensate each other, resulting in a bulk insulating TI. A systematic transport study of $Bi_{2-x}Sb_xTe_{3-y}Se_y$ alloys has found high low temperature resistivity values in $BiSbTeSe_2$ (BSTS1) and $Bi_{1.5}Sb_{0.5}Te_{1.7}Se_{1.3}$ (BSTS2) of 5.5 and 4.5 Ω cm, respectively. These findings imply that bulk carriers are largely eliminated, and are highly promising materials for studies of SSs and potential applications [79] Furthermore, photoemission measurements of identically grown BSTS1 and BSTS2 alloys have revealed that μ_F is located within the bulk energy gap, at or near the SS Dirac point, indicating that these materials are ideal for surface dominated conductance.

Here we report infrared (IR) spectroscopy measurements on bulk BSTS1 and BSTS2 crystals grown as described in Ref. [79]. We initially characterized the bulk electronic properties of these samples using IR techniques, in the absence of an externally applied magnetic field. Analysis of the optical constants extracted from these mea-

surements, detailed later in the text, reveals that both BSTS1 and BSTS2 are strongly insulating with effectively no signature of free carriers or impurity bands in the optical conductivity. Additionally, the analysis reveals that BSTS2 has both an exceptionally large energy gap of 0.35 eV, and shows characteristics IR features attributable to distinct critical points in the band structure. These band structure critical points (BSCP) are indicative of a high degree of crystallographic order, which is unusual for an alloyed system. Furthermore, we have used our optical conductivity spectra to establish upper limits on the bulk carrier density (n), revealing that the maximum value of n for both alloys is relatively small, being at most 4.5 x 10^{17} cm^{-3}. To directly study the SS properties, we performed infrared reflectivity measurements in high magnetic fields, a technique which has been used to characterized SSs in other TI materials [57]. In spite of the promising findings of the initial zero field infrared measurements, we did not observe the characteristic LL dispersion of SSs in these BSTS compounds. These data and possible reasons for this null result are discussed later in the text.

3.2 Experimental Techniques and Discussion

3.2.1 Infrared spectroscopy and optical conductivity

We obtained the zero-field IR spectra of BSTS samples using a combination of normal incidence reflectance and variable angle spectroscopic ellipsometry (VASE), which is discussed in more detail in the appendix. The sample optical constants were extracted by performing a Kramers-Kr onig (KK) inversion of the combined reflectance (R(ω)) and VASE datasets. The real part of the complex conductivity ($\sigma_1(\omega)$) was extracted from the KK fitting of the infrared data at all measured temperatures and the resulting spectra are shown in Fig. 3.1. These $\sigma_1(\omega)$ spectra can be divided into four regions of interest, with the corresponding label indicated in parenthesis: the low ω region (α), the phonon peak (β), the intragap region (γ) and the interband absorption region (δ), as indicated in Fig 3.1. The α region is related to the free charge carrier dynamics, and in the case of a simple Drude metal is described by the formula [82]:

$$\sigma_1(\omega) = \frac{ne^2\tau}{m^*}\frac{1}{1+(\omega\tau)^2} \tag{3.1}$$

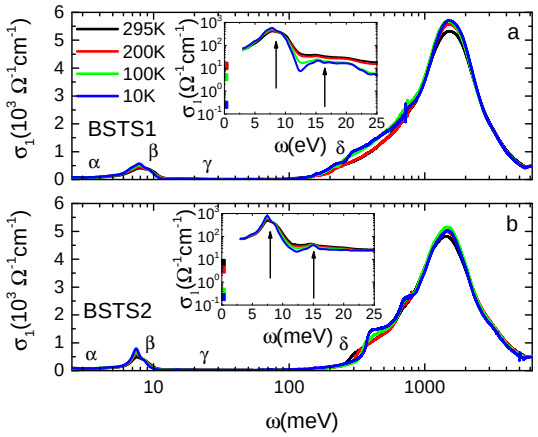

Figure 3.1: Optical conductivity spectra of $Bi_{2-x}Sb_xTe_{3-y}Se_y$ for x=1,y=1(a) and x=0.5,y=1.7 (b). The salient features of the spectra are the low ω region (α), the phonon peak (β), the intergap region (γ) and the onset of interband conductivity (δ). The α and β regions are detailed in the insets of (a) and (b), with the phonon center frequencies indicated by the arrows. The measured DC conductivities of identically grown samples are indicated by the squares along the y-axis, colored to match the corresponding temperature.

where m^* is the effective mass and τ is the scattering rate. However, the α region of our $\sigma_1(\omega)$ spectra show no indication of a Drude lineshape; rather the optical conductivity at low ω is small and decreases towards the measured DC value of conductivity, indicative of a band insulator. In the higher energy β region, there are two peaks in $\sigma_1(\omega)$ corresponding to the IR active phonons that have been observed previously in other similarly structured TI materials [45, 46]. These two phonons, indicated by the arrows in the insets to Fig. 3.1a and 3.1b, are centered at 62 cm^{-1} and 120 cm^{-1} (63 cm^{-1} and 117 cm^{-1}) for BSTS1 (BSTS2), and sharpen with cooling. An inspection of the phonon lineshapes reveals that the peaks are broader in BSTS1 than in BSTS2, implying lower disorder in the latter alloy. The conductivity in the interband region, γ, is small and featureless for both materials, as is typical of semiconductors. Importantly, we observed no indication of the impurity band which was observed in the related compound Bi_2Te_2Se [67, 83], and in identically grown $Bi_{2-x}Sb_xTe_{3-y}Se_y$ alloys [77].

3.2.2 Interband transitions

The onset of interband transitions, which occur in the higher energy region δ, are indicated by the increase in $\sigma_1(\omega)$ near 2000 cm^{-1} for both BSTS1 and BSTS2. The energy gap (E_{Gap}) of these systems is precisely determined by the x-axis intercept of a linear fit to $(\varepsilon_2(\omega))^2$ as prescribed in [55], where $\omega[s^{-1}]\cdot\varepsilon_2(\omega[s^{-1}])/4\pi = \sigma_1(\omega)[s^{-1}]$ [82]. We show the $(\varepsilon_2(\omega))^2$spectra for both BSTS1 and BSTS2 in Fig. 3.2a and Fig. 3.2b, respectively, along with the linear fit that was used to determine E_{Gap}. This analysis reveals significant differences in the lineshape of the optical constants corresponding to the interband transitions near 2000 cm^{-1}. In BSTS1, cooling the sample from 300K to 200K, shifts the linear region in $(\varepsilon_2(\omega))^2$ to slightly higher ω. Decreasing the temperature further produces two significant changes; the energy gap is shifted to lower energies, and a second linear region appears in $(\varepsilon_2(\omega))^2$, indicating a the appearance of a second interband transition, which persists down to 10K. The energy gap is plotted as a function of temperature in Fig. 3.2c as the black squares, with the second interband transition energy also indicated by the black circles. In contrast, there is only a single linear region in the $(\varepsilon_2(\omega))^2$ spectra of BSTS2, which monotonically increases in energy with decreasing temperature. Accordingly, the extracted value of E_{Gap}, plotted in Fig. 3.2c as the red squares, shifts from 2050 cm^{-1} (0.27 eV) at 300K to the relatively large value 2800 cm^{-1} (0.35 eV) at 10K. One possible explanation for the two transitions identified in BSTS1 is that they originate from slightly different regions in the band structure. At high temperatures, the band structure may be slightly smeared out making the two transitions indistinguishable. With cooling, the possible sharpening of the band structure could reveal the two distinct interband transitions we observe. Unfortunately, there are no temperature dependent measurements of the band structure that could confirm this speculation. An alternative possibility is that we are probing two regions of distinct stoichiometry with our infrared light.

3.2.3 Band structure critical point: observation and analysis

An additional interesting feature is the step-like region in the optical conductivity of BSTS2, detailed in Fig. 3.3a. These features are reminiscent of the theoretically

derived lineshape for the optical constants arising from regions in the band structure where the conduction band ($E_C(\vec{k})$) and valence band ($E_V(\vec{k})$) are parallel [55]. The parallel bands produce a BSCP, where there is a divergence in the joint density of states, resulting in a unique dielectric constant lineshape in the optical response [55, 84].To identify possible locations of these BSCP transitions, we examined the calculated band structure of the related compound, Bi_2Se_3, which was taken from Ref. [36] and plotted in Fig. 3.3d . From this band structure, we identified four different possible BSCP transitions, which are indicated by the arrows in Fig. 3.3d. Two of the transitions have almost identical energies, and are therefore likely to manifest as a single BSCP transition. Accordingly both of these transitions have been labeled as CP1 in the schematic, with the remaining two are labeled CP2 and CP3. The BSCP that produce the step-like features in the $\sigma_1(\omega)$ spectra, are indicated in Fig. 3.3a. The solid lines in Fig. 3.3e indicate the theoretical energies of the various BSCP transitions. To characterize the measured optical conductivity in terms of BSCP, $\hat{\varepsilon} = \varepsilon_1 + i\varepsilon_2$ was fit using the standard lineshape for a 3-dimensional BSCP [84]:

$$\frac{d^2(\varepsilon_1 + i\varepsilon_2)}{d\omega^2} = \frac{1}{4} A e^{i\phi} (\omega - \omega_0 + i\xi)^{-3/2}. \tag{3.2}$$

The fitting parameters of this equation are: the amplitude (A) which is related to the reduced mass of the two bands, the energy difference between the bands at the BSCP (ω_0) and broadening (ξ), which corresponds to the quasiparticle lifetime [49], and lastly, the phase (ϕ), a value that is related to the band structure in the region near the critical point. The experimentally obtained $d^2\varepsilon_1/d\omega^2$ and $d^2\varepsilon_2/d\omega^2$are plotted in Fig. 3.3b and 3.3c, respectively, along with the best fit lineshape (gray) which consisted of three BSCP. Moreover, the BSCP that produced the resonances in the $d^2 eps\hat{i}lon/d\omega^2$ spectra are indicated in Fig. 3.3b and 3.3c. The parameter ω_0, which was extracted from the fitting of the BSTS2 data, is plotted as a function of temperature in Fig. 3.3e alongside the transition energies determined from the calculated band structure. Comparing the theoretical values of ω_0 to those extracted from the experimental data reveals that the theoretical energies of CP1 and CP2 differ significantly from the measured values. In contrast, the expected energy of CP3 differed by less than 0.03 eV from the experimental values. These results may indicate that band structure of this system is well understood at energies greater than the energy gap, but is strongly modified from theoretical calculations

at lower energies. Currently, no band structure calculations on the $Bi_{2-x}Sb_xTe_{3-y}Se_y$ alloys have been published, but these critical points may serve as useful constraints for future work.

Observation of BSCP requires two ingredients: conservation of momentum ($\vec{k}$), which typically implies a structurally ordered material, and a location in the band structure where a band below E_F is parallel to a band above E_F. The lack of BSCP in BSTS1 indicates that this compound is missing one of the above elements. Our infrared measurements reveal significant differences in the optical response of these two systems, especially near E_{Gap}. The modification to the band structure as the Bi:Sb and Se:Te ratios change may then eliminate the critical points in the band structure. Unfortunately, since photoemission measurements only probe below E_F, experimentally measuring changes to the conduction band with alloying, that could eliminate the CP are very difficult [85]. The crystallographic order, however, has been measured via x-ray diffraction in [79], which demonstrated that the characteristic (1,0,7) and (0,0,12) peaks, indicative of ordering in the chalcogen layers, are present for both BSTS1 and BSTS2. Therefore, the lack of CP in BSTS1 is likely due to the inherent band structure, rather than a reduced crystallographic order.

3.2.4 Discussion

Although our findings and complimentary photoemission measurements of identically grown samples suggest μ_F resides within the bulk energy gap [85], transport measurements have indicated the presence of an impurity band, in addition to the SS and a surface accumulation layer, that could contribute free carriers to bulk conduction [77]. To quantify the possible role of bulk carriers in these samples, it is useful to independently quantify the free carrier concentration (n). While infrared data cannot precisely measure the value of n, we can estimate n based on the R(ω) spectra at low ω, using the procedure described in the appendix. Our analysis shows that the largest carrier concentration that could be present in this system, yet still be consistent with our experimental reflectance is 4.4×10^{17} cm^{-3}. This value, despite being an upper estimate, places this system among the most insulating TI crystals that have been measured so far [78, 83]. Furthermore, this estimate is based solely on reflectance data and is not

anchored by the DC conductivity values measured in [79], which, if included, would reduce this estimate even further.

The CP and spectral analysis discussed above is indicative of a few important aspects of the $Bi_{2-x}Sb_xTe_{3-y}Se_y$ system. First, our measured optical constants show that these alloys are insulators, with a band structure that is strongly modified with cooling. For instance, in BSTS1, a second interband transition is revealed at lower temperatures that is 50% larger in energy than lowest energy transition, E_{Gap}. In BSTS2, E_{Gap} is 0.274 eV at room temperature, but increases by 35% to 0.35 eV with cooling, becoming significantly larger than the 0.3 eV value that is often quoted for pure Bi_2Se_3 [7]. Second, the BSTS2 system confirmed to be a structurally ordered material, as CPs are only observed in systems where $\vec{k}$ is a good quantum number [49, 84]. Since conventional alloying wipes out critical points, the observation of sharply defined CPs in Figs. 3.3b and 3.3c are quite remarkable and suggest non-trivial ordering in the BSTS2 alloy. Third, the observation of critical points in BSTS2, which are consistent with transitions at the Γ point, firmly establishes that μ_F is in the bulk energy gap, since any doping into the conduction band would result in occupied states near the Γ point, making them unavailable to transitions from the valence band. Lastly, the upper limits we establish on n place this system among the most insulating TI crystals reported, thereby confirming the effectiveness of alloying in reducing the carrier concentration. The picture that emerges from these findings is that these crystals possess some of the key ingredients thought necessary for observation of surface states, including crystallographic ordering, large energy gap, and low carrier density. Therefore, we tested for the presence of surface states in these materials using magneto optical techniques, which have been demonstrated to be effective tools for the measurement of SS [57, 86, 87].

3.2.5 Magneto-optical spectroscopy

Magneto-optical spectroscopy is an experimental technique that utilizes the fact that electrons undergo cyclotron motion in the presence of crossed electric and magnetic fields at a characteristic frequency $\omega_c = eB/m^*$ [88]. Importantly, the cyclotron motion results in the splitting of the energy bands into discrete Landau levels (LL), which are distinguished by their index, l. These LL disperse with field depending on the effective

mass of the charge carriers [57, 88, 89]. Using infrared spectroscopy, it is possible to excite transitions between LL under the constraint that $|\Delta l| = 1$, yielding absorption features in optical spectra. To compare our magneto optical response, to that expected for LL arising from SS, we calculated the expected LL dispersion using the theoretical framework in [57, 89], and the SS bands described in [77].

In the case of BSTS1, E_F resides at the Dirac point [85], thereby allowing inter-LL transitions, *i.e.* transitions from l_{-n} to l_{n+1}, as illustrated in Fig. 3.4a. Accordingly we measured the reflectance spectra of both BSTS1 and BSTS2 in the range from 10 meV to 80 meV, where these transitions are expected. The resulting zero-field normalized ($R(H)/R(H = 0T)$) spectra, are shown in Fig. 3.4b and 3.4c, for BSTS1 and BSTS2, respectively. There is a noticeable modification to the reflectence with increasing field near 200 cm^{-1}, corresponding to a dip in reflectance arising from the phonon. At higher energies there is some additional noise with increasing H, but overall the spectra are unaffected by the magnetic field. In previous measurements of $Bi_{1-x}Sb_x$, the LL transitions produced changes in the $R(H)/R(H = 0T)$ spectra on the order of 0.01, at fields as small as 3T [57]. Furthermore, these transitions were found to be much more evident in the dR/dH spectra. To illustrate the expected behavior of the magneto-optic features associated with the LL, the calculated energy of the $0 \rightarrow 1$, $-1 \rightarrow 2$ and $-2 \rightarrow 3$ inter-LL transitions are indicated in Fig. 3.4b and 3.4c at each field by the gray squares, circles and triangles, respectively. However, these data reveal no anomaly at the expected inter-LL transition energy, nor any feature that shows the expected field dependent behavior. To confirm this, we performed the same dR/dH analysis used in [57] and found the dR/dH spectra to be effectively featureless, lacking any indication of the LL transitions.

Alternatively, we considered the case of BSTS2, where E_F is positioned well above the Dirac point [85], and many of the inter-LL transitions are blocked. Instead, the so called intra-LL transitions occur between adjacent LLs of the same sign, *e.g.* $l_n \rightarrow l_{n+1}$, as illustrated in Fig. 3.4d. To test for the signatures of the intra-LL transitions, we extended the magneto-reflectance measurements to lower energies (2.5 meV to 12 meV) where they were expected to be most prominent. These low energy $R(H)/R(H = 0T)$ spectra, are shown in Fig. 3.4e and 3.4f, for BSTS1 and BSTS2, respectively. As in the

discussion of inter-LL transition, the expected intra-LL transition energy at each field is indicated by the gray diamond. Again, there is no feature in these spectra that is consistent with the expected behavior of LL transitions.

The lack of either intra-LL or inter-LL transitions in our magneto optical measurements was an unexpected finding and deserves some consideration. Prior STM measurements of the LL dispersion in the related TI material, Bi_2Se_3, found LLs form only with positive indices ($l \geq 0$) because the lower LLs merge with the bulk valence band [90]. Therefore, when E_F is small, as in BSTS1, the missing LL would inhibit all transitions except for $0 \rightarrow 1$. Moreover, for this transition to be observeable, the E_F would have to be ideally position near the Dirac point, within the small range between the $l = 0$ and $l = 1$ LL, which is approximately 70 meV, at 8T (see Fig. 3.4a). Even though photoemission has indicated E_F is at the Dirac point in BSTS1[85], aging effects have been observed in similar samples [77], and E_F may simply vary slightly between crystals, possibly making this inter-LL transition unobservable. However, if E_F was shifted upwards by 70 meV, we would still expect to see intra-LL transitions. Since we see neither intra-LL or inter-LL transitions in either sample, there must be an alternative explanation. Interestingly, the observation of critical points in the BSTS2 crystal suggests that it is structurally ordered in the bulk, with a low scattering rate. This observation, in conjuction with the lack of observeable LL transitions implies that the SS are more strongly disordered than the bulk states, with a correspondingly higher scattering rate ($1/\tau$), which would result in the suppressesion of LL formation, as we observe. Since there was no in-situ cleaving system available in our magneto-optic setup, our samples were cleaved in ambient conditions, and then placed in vacuum for magneto-optic measurements. Possibly, exposure to the environment for this brief time was enough to degrade the BSTS surfaces and introduce strong disorder into the SS, while the crystal bulk remained unaffected. There is support for the hypothesis that the surface electrons are strongly scattered in transport measurements of identically grown BSTS2 crystals [77]. These measurements revealed the scattering time (τ) of the SS electrons was $4.2 \times 10^{-14} s$, corresponding to $1/\tau \approx 800 cm^{-1}$ [91].

Another issue that compounds the difficulty of observing the SS LLs via magneto-optical spectroscopy is the small surface carrier density (n_{2D}) of these materials. In the

case of identically grown BSTS2 crystals, n_{2D} was found to be approximately 10^{12} cm^{-2} [77]. Such a small carrier density would also reduce the signature of cyclotron motion in reflectance, even with relatively low scattering rates. Indeed Models of the magneto-optical response, detailed later in the text, show that the cyclotron resonance signature in reflectance would be below our measurable range with scattering rates near 200 cm^{-1}. A further discussion of how the scattering rate affects the reflectance measurement at such low carrier densities is presented in the appendix. Likewise, the appendix also contains an explanation for how the high mobility reported in [77], could coexist with the large scattering rate.

3.3 Conclusions

Our comprehensive infrared measurements and corresponding analysis of BSTS1 and BSTS2 have revealed both materials to be highly insulating, with the upper limits on the carrier concentration that are among the lowest measured values in crystalline TIs. In addition, the observation of critical points in BSTS2 identifies this alloyed material as crystallographically ordered, which may yield high mobility in the SSs, if the current unknown issues hindering the SSs in $Bi_{2-x}Sb_xTe_{3-y}Se_y$ are resolved. Together, these results indicate that BSTS1 and especially BSTS2 are promising candidates for surface dominated electronic response. However, no signs of SSs were observed in magneto optical measurements, suggesting that μ_F is positioned above the Dirac point, or that the transitions are suppressed by a high scattering rate. Importantly, many of the exotic properties predicted to emerge in TI systems require that μ_F be precisely at the Dirac point, thereby allowing a gap can to be opened in the SSs with a magnetic field [58, 59, 76, 92]. Furthermore, it is likely that these phenomena would require high crystallographic order and a low scattering rate for SS electrons. The capability to simultaneously probe each of these elements via IR spectroscopy makes this technique indispensible for identification of ideal TI materials.

3.4 Appendix

3.4.1 Raw reflectance data

The raw reflectance data of BSTS1 and BSTS2 is shown in Fig. 3.5a and 3.5b, respectively. Like conductivity, the reflectance spectra exhibit four main regions of interest, with their corresponding label indicated in parenthesis: the low ω region (α), the phonon peak-dip (β), the intragap region (γ) and the interband absorption region (δ). In region α, the reflectivity levels at R=0.76 (0.78) for BSTS1 (BSTS2) at 300K. When cooling to 10K, there is a slight upturn in the reflectivity of BSTS1, and it approaches 0.82 at the lowest accessible frequencies, whereas in BSTS2, reflectivity remains nearly constant with cooling at a level of 0.82. Our observation of R(ω) < 1 at the lowest measured frequencies identifies these materials as non-metallic.

In both samples, we observe a peak dip structure in the β region of reflectivity, indicative of a strong phonon. The peak-dip structure sharpens as temperature is reduced, revealing two slight shoulder features at 68 cm^{-1} and 124 cm^{-1} (63 cm^{-1} and 117 cm^{-1}) in BSTS1 (BSTS2). The phonon structure we observe has been seen in other TI materials [45, 46, 67]. In the intragap region γ of BSTS1, we observe an increasing slope as the temperature is lowered from 200K to 100K. The intergap region δ is identified by the peak in conductivity near 2,000 cm^{-1}, which sharpens and blue shifts with decreasing temperature.

In BSTS2, the reflectivity in the intra-gap region γ, remained flat and featureless with decreasing temperature, typical of an insulating material. The higher energy region δ, can be clearly identified as the peak in reflectivity, corresponding to the onset of interband absorption, which sharpens and blue shifts with decreasing temperature. A second peak in reflectivity is noticeable at 5000 cm^{-1} indicating a second interband transition. This peak, in contrast to the lower energy feature, does not shift noticeably with temperature.

3.4.2 Carrier density upper limit

In the presence of free carriers, R(ω) will approach 1 as $\omega \to 0$, corresponding to the so called Drude peak in optical conductivity. Conversely, in the absence of free

carriers, R(ω)will remain constant at a value smaller than 1 (see Fig. 3.5). It is important to note that within our experimental range of, there is no evidence to suggest that R(ω) approaches 1. However, we have considered the scenario that there are free carriers in these materials, but the characteristic increase in R(ω) towards 1 simply occurs below our experimental range. Accordingly, we show the experimental reflectance at 10K for BSTS1 and BSTS2, in Fig. 3.6a and 3.6b, along with two alternative low extrapolations. The corresponding values of $\sigma_1(\omega)$, obtained from the extrapolated R(ω) spectra via KK inversion, are plotted Fig. 3.6c and 3.6d. As expected, the low frequency extrapolation to 1 results in a finite value of $\sigma_1(\omega)$ as $\omega \to 0$, producing a weak Drude peak. On the other hand the flat extrapolation results in $\sigma_1(\omega)$ spectra that approaches 0 at low ω. We modeled the extracted spectra of $\sigma_1(\omega)$ with a single Drude oscillator and a Lorentz oscillator to capture the phonon peak. These fits are indicated in Fig. 3.6c and 3.6d by the dashed gray lines on top of the experimental data. Since the Drude oscillator strength (ω_p^2) is directly related to the carrier density (n) via [91]:

$$\omega_p^2 = \frac{ne^2}{\varepsilon_0 m^*}, \tag{3.3}$$

the carrier density arising from the Drude peak could be extracted assuming an effective mass of $0.11m_e$ as measured in Bi_2Te_2Se [83]. Theresulting maximum carrier concentrations (n_0^{max}), indicated in Fig. 3.6c and 3.6d, are $1.57 \times 10^{17} cm^{-3}$ and $4.36 \times 10^{17} cm^{-3}$ for BSTS1 and BSTS2, respectively. These values, despite being upper limits, are among the lowest values of n reported for TI crystals [78, 83, 93]. Additionally, the maximum Fermi energy (E_F^{max}), within the bulk conduction band, could be extracted from the carrier density, assuming parabolic bands [65]. The resulting values of E_F^{max} are 9 meV (19 meV) for BSTS1 (BSTS2). Using these values of E_F^{max}, it was possible to also estimate the maximumsurface carrier density (n_{2D}^{max}) in these crystals. To make this estimations we assumed that the valence band edge is at the Dirac point, as indicated by photoemission measurements [85]. Then, the Fermi energy of the SS (E_F^{ss}), relative to the Dirac point, would be given simply by $E_F^{max} + E_g$, as illustrated in Fig. 3.6e and 3.6f. Once E_F^{ss} is determined, n_{2D}^{max} is then simply given by [94]:

$$n_{2D}^{max} = \left(\frac{E_F}{\hbar v_0}\right)^2 \frac{1}{4\pi}. \tag{3.4}$$

The resulting values of n_{2D}^{max} are $7.7 \times 10^{11} cm^{-2}$ ($3.9 \times 10^{12} cm^{-2}$) for BSTS1 (BSTS2). The intra-LL dispersions, associated with these Fermi energies, are plotted in Fig. 3.6g. These energy dispersion curves lie within our measurable range, as shown in Fig. 3.4, yet wereunobservable. Importantly, the values of n_{2D}^{max} should only be considered as upper limits, rather than definite estimates. Likewise, the scattering rateassociated with these values of n_{2D}, 33 cm^{-1} (41 cm^{-1}) in BSTS1 (BSTS2) should be considered lower limits. Indeed, the intra-LL dispersion associated with these values of n_{2D}^{max} should be observable with such low scattering rates. Instead, the overall lack of measurable LL features suggests the SS have a much higher scattering rate, with a correspondingly smaller carrier density.

3.4.3 Mobility and scattering rate

The relatively high mobility of 9.8×10^2 $cm^2/(V \cdot s)$ reported for BSTS1 seems to conflict with the large scattering rate of 800 cm^{-1} [77]. However, this can be understood by considering the relationship between mobility(μ), carrier density (n) and scattering rate (τ) in Dirac electron systems [95]:

$$\mu = \frac{e\tau v_F}{2\hbar\sqrt{\pi n}} \tag{3.5}$$

While μ is directly proportional to the scattering time, it is also inversely proportional to the carrier density. Thus, a low carrier density will overcome the small scattering time to yield a relatively high mobility. To illustrate the effects of a large scattering rate on our experimental data, we have modeled the reflectance spectra using a 2D surface carrier density of 10^{12} cm^{-2}, as was found in similarly grown crystals, with various scattering rates. To illustrate the changes that would be expected assuming different scattering rates, the modeled reflectance ratios R(H=8T,Γ)/ R(H=0T,Γ) shown in Fig. 3.7. There is a noticeable modification to the reflectance spectra when Γ=20 cm^{-1}, but when Γ approaches more reasonable values of 200 cm^{-1}, the signature becomes much weaker, and is likely undetectable, based on signal to noise limitations.

3.5 Acknowledgements

This work was partially supported by DOE-BES (DE-FG03-00ER45799), UCOP and JSPS (KAKENHI 25220708), MEXT (Innovative Area "Topological Quantum Phenomena" KAKENHI 22103004), and AFOSR (AOARD 124038). YSL was supported by NRF-2013R1A2A2A01068567.

Chapter 3 is a reprint of material published in *Physical Review B* **91**, 165202 (2015). K.W. Post, Y.S. Lee, B.C. Chapler, A.A. Schafgans, Mario Novak, A.A. Taskin, Kouji Segawa, M.D. Goldflam, H.T. Stinson, Yoichi Ando and D.N. Basov. The dissertation author was the primary researcher and author of this material.

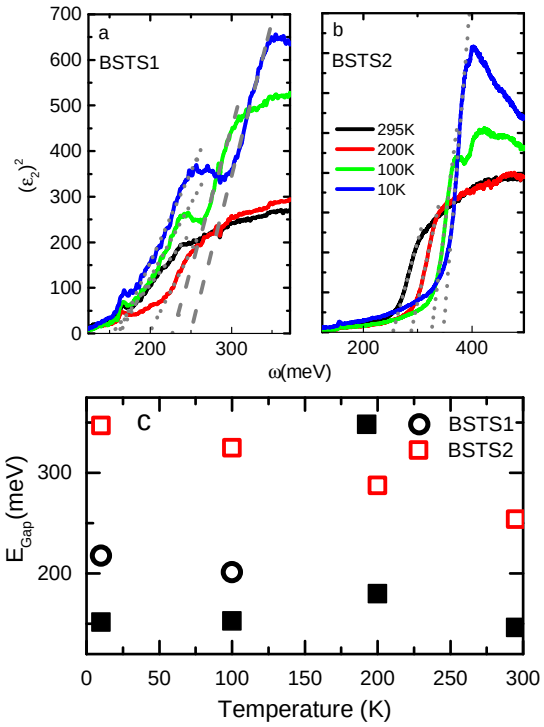

Figure 3.2: The $(\varepsilon_2)^2$ spectra of $Bi_{2-x}Sb_xTe_{3-y}Se_y$ are shown for x=1,y=1 in (a) and and for x=0.5,y=1.7 in (b). The linear region of $(\varepsilon_2)^2$ indicates the direct band gap, and the x-axis intercept of the linear fits, indicated by the dotted gray lines, gives a numerical value for E_{Gap}. The values of E_{Gap} extracted using this method are plotted as a function of temperature in (c). With cooling, a second linear region emerges in BSTS1, which was fit at 100K and 10K as indicated by the dashed gray lines. The energy corresponding to this second interband transition is plotted in (c) as the black open circles.

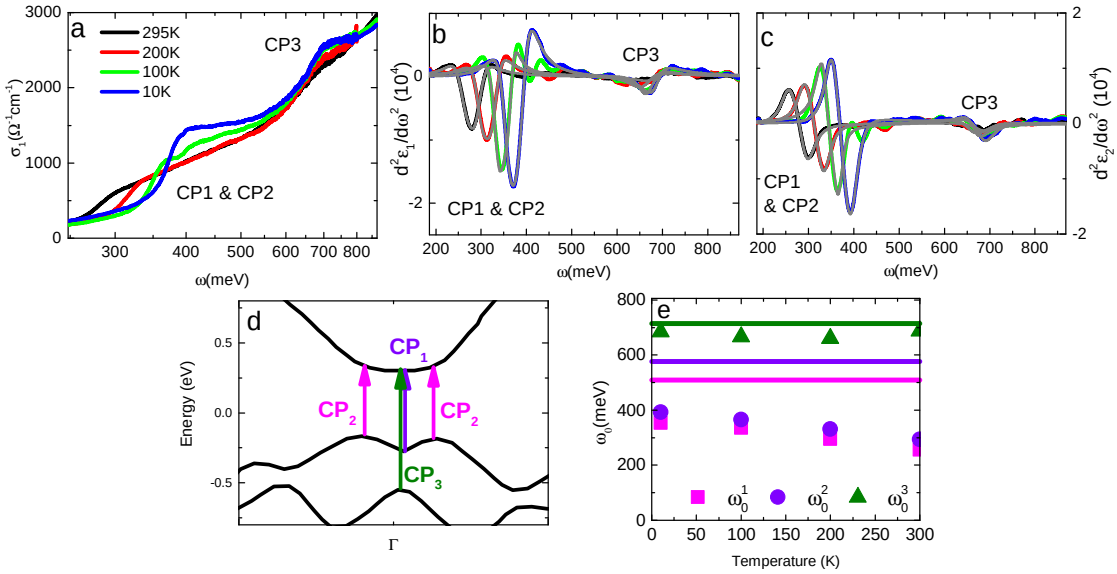

Figure 3.3: Critical point analysis of $Bi_{1.5}Se_{0.5}Te_{1.7}Se_{0.3}$. The step like features in the optical conductivity of BSTS2 is shown in (a). The theoretical band structure of Bi_2Se_3 in (d) contains four possible critical points with three different energies that could generate the step like behavior of $\sigma_1(\omega)$. The $d^2\varepsilon_1/d\omega^2$ and $d^2\varepsilon_2/d\omega^2$ spectra of BSTS2 are plotted in (b) and (c), respectively. The colored lines are the experimental data, and the gray lines are fits to the critical point lineshape (Eq. 4). The critical points corresponding to the step like features in the $\sigma_1(\omega)$ spectra, and the resonances in the $d^2\hat{\varepsilon}/d\omega^2$ are indicated in a,b, and c. The energy of the critical points determined from band structure calculations are indicated by horizontal lines, colored to match their respective transition in (d).

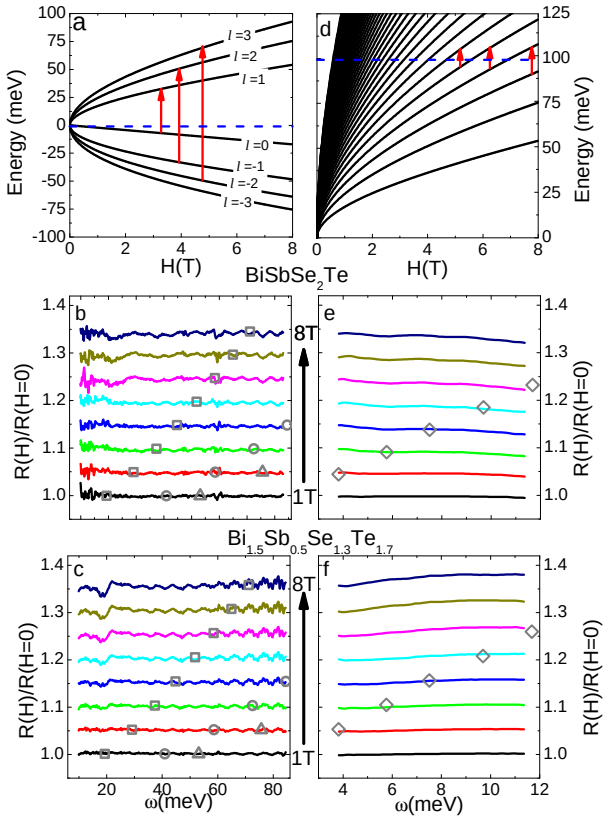

Figure 3.4: Magneto-Optic measurements of $Bi_{1.5}Se_{0.5}Te_{1.7}Se_{0.3}$. The LL dispersion of the SS is plotted in (a) along with the allowed transitions (red arrows) assuming E_F (dashed blue line) is at the Dirac point. The field normalized reflectance ($R(H)/R(H=0)$), with increasing fields offset by 0.05, is plotted in (b) and (c) for BSTS1 and BSTS2, respectively. The gray squares, circles and triangles on the experimental (colored) data indicate the expected position of inter-LL transitions, based on the disperion shown in (a). In (d) we schematically show the intra-LL transitions when E_F is well above the Dirac point, with the red arrows indicating transitions between adjacent LL. The low energy $R(H)/R(0)$ spectra for BSTS1 and BSTS2, is shown in (e) and (f), respectively, offset by 0.05. The energy of the intra-LL transitions were calculated assuming $E_F =$ 100 meV, and are indicated by the gray diamonds on the experimental data.

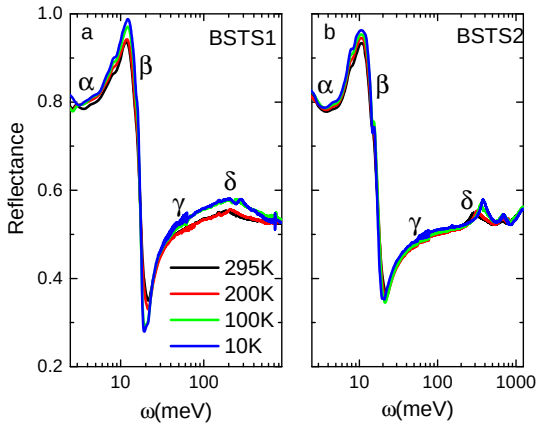

Figure 3.5: Raw reflectance spectra of $Bi_{2-x}Se_xTe_{3-y}Se_y$ for x=1,y=1 in panel (a) and x=0.5,y=1.3 (b), respectively. The regions α, β, γ, and δ, that were noted in conductivity, are also indicated here.

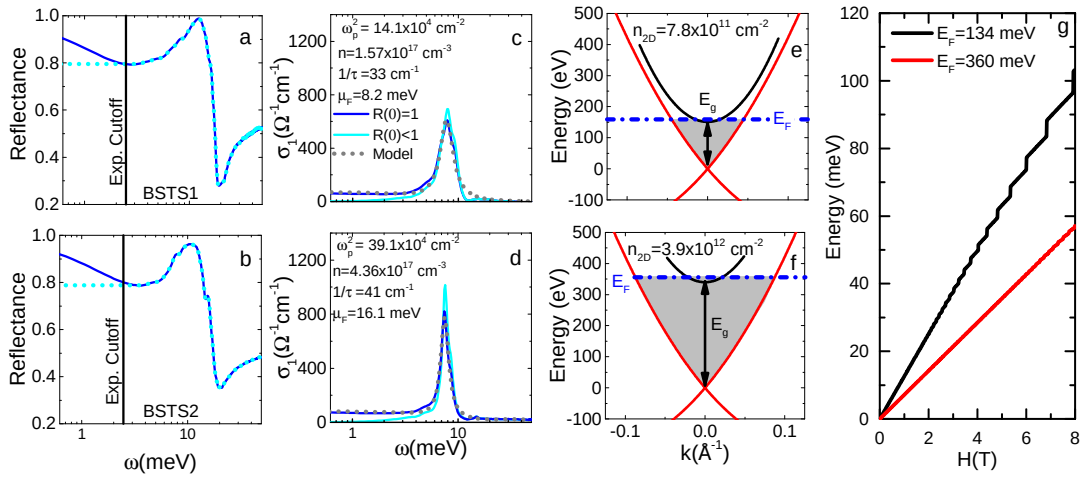

Figure 3.6: Low frequency extrapolation of extrapolation of the reflectance spectra of $Bi_{2-x}Se_xTe_{3-y}Se_y$ was modified to capture the possible existence of surface state carriers. The measured reflectance of BSTS1 (a) and BSTS2 (b) are shown with the low two types of low frequency extrapolations. The solid blue line assumes reflectance goes to 1 at low frequencies, as is typical for metals, whereas the dashed cyan line assumes a flat reflectance, as expected for an insulator. The $\sigma_1(\omega)$ extracted via KK inversion for either type of extrapolation is shown in (c) and (d) for BSTS1 and BSTS2, colored to match the reflectance data. A simple Drude-Lorentz fit to $\sigma_1(\omega)$ is also plotted as the dashed gray line. The Drude oscillator strength (ω_p^2) obtained from this fit, and indicated in (c) and (d), was used to determine the maximum bulk carrier density (n_0^{max}) in each system. Likewise, the scattering rate associated with this Drude oscillator is also indicated. The maximum value of the Fermi energy in the bulkconduction bands (E_F^{max}) was then determined from n_0. And is indicated in (e) and (f) for BSTS1 and BSTS2, respectively. The two dimensional surface carrier density (n_{2D}) corresponding to E_F^{max} in both systems was then determined and is also shown in (e) and (f). The expected field dispersion of the intra-LL transitions, corresponding to the carrier densities obtained in (e) and (f) are plotted in (g).

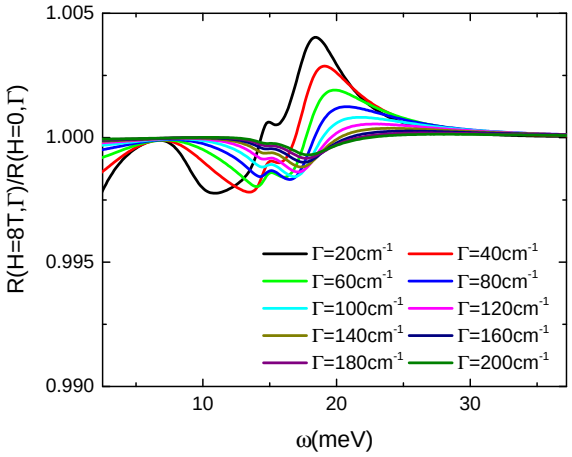

Figure 3.7: The modeled reflectance ratios of $Bi_{1.5}Se_{0.5}Te_{1.7}Se_{1.3}$ are plotted at H=8T, assuming a 2D carrier density of 10^{12} cm^{-2} and different scattering rates (Γ). As Γ increases from $20cm^{-1}$ to 200 cm^{-1} , the modification to the reflectance spectra is reduced from 0.4% to below 0.05%.

Chapter 4

Sum rule constraints on the surface state conductance of topological insulators

Abstract

We report the Drude oscillator strength (D) and the magnitude of the bulk band gap (E_g) of the epitaxially grown, topological insulator $(Bi,Sb)_2Te_3$. The magnitude of E_g, in conjunction with the model independent f-sum rule, allowed us to establish an upper bound for the magnitude of D expected in a typical Dirac like system composed of linear bands. The experimentally observed D is found to be at or below this theoretical upper bound, demonstrating the effectiveness of alloying in eliminating bulk charge carriers. Moreover, direct comparison of the measured D to magneto-resistance measurements of the same sample support assignment of the observed low-energy conduction to topological surface states.

4.1 Introduction

The prediction and discovery of Dirac-like gapless surface states (SSs) (see Fig.4.1) at the interface between a topological insulator (TI) and trivial insulator have

vaulted TIs to the vanguard of condensed matter physics [2]. Surface probes such as angle resolved photoemission spectroscopy (ARPES) and scanning tunneling spectroscopy (STS) have been extremely successful in verifying and discovering novel phenomena associated with the SSs (*e.g.* Refs. [7, 8, 34, 96]). However, progress in the field has been plagued by native defects, resulting in significant concentrations of bulk charge carriers. These bulk dopants inhibit isolation and utilization of SS phenomena [97]. In order to realize many of the novel scientific and technological advances that could blossom from the unique electronic, spin, and optical properties of SS in TIs, it is paramount to eliminate the bulk dopants.

Two archetypal strong TIs (topological invariant ν_0=1 [2]) that are known to suffer from materials issues related to bulk dopants are Bi_2Te_3 and Sb_2Te_3. However, epitaxial films of Bi_2Te_3 can be *n*-type bulk conductors [97, 98], whereas Sb_2Te_3 films are *p*-type bulk conductors [99]. Based on this observation, TI materials have been grown where the ratio of Bi:Sb in $(Bi,Sb)_2Te_3$ (BST) is tuned to produce a compensated material with bulk insulating properties[67, 100, 101]. Here we prove, using optical spectroscopy, the acute effectiveness of alloying in reducing or eliminating bulk charge carriers. The advantage of our optical experiments is that they give direct access to the frequency dependent electrodynamic response of free carriers in a metal via the Drude peak. In our $(Bi,Sb)_2Te_3$ film we find the Drude oscillator strength D sufficiently low as to lie at or below the upper bound that theoretically anticipated for an isolated Dirac SS Drude response (*i.e.* a Drude response with no bulk contribution) (see Table 4.2). These infrared data are complemented by charge carrier density n and mobility μ from Hall effect measurements, as well as magnetoresistance, which are all consistent with low-energy conduction arising from the topological SS.

4.2 Simplified Model of Conductance

We begin by describing the optical response of Dirac electrons in a strong TI, neglecting potential interband bulk→SS transitions (or *vice versa*). The simplest Dirac electron system is composed of linear bands (LB), without spin or valley degeneracy, where the dispersion is given by $E(k) = kv_F$, as illustrated schematically in Fig.

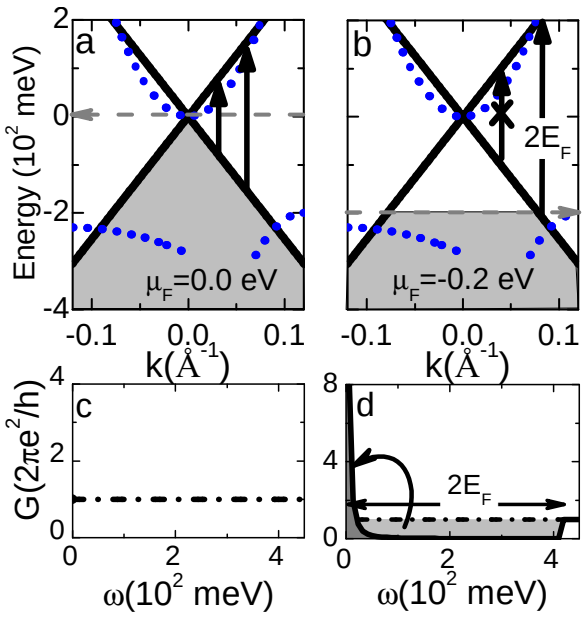

Figure 4.1: Sum rule constraints on the infra-red response of a TI from a schematic band structure. Panel (a) and (b) show the band structure of a model TI, where the SS is composed of simple linear bands. The bulk band structure is also indicated by the dotted blue lines, consisting of two hole bands and an electron band. In (a) E_F is at the Dirac point, while in (b), E_F is 0.20 eV below the Dirac point, where the arrows in both panels schematically show the allowed transitions. In (a), interband transitions are allowed at all energies, giving rise to the conductance spectra shown in (c). When E_F is shifted below the Dirac point, transitions cannot occur from the depopulated region. Thus, transitions are suppressed below $2|E_F|$, giving rise to the conductance spectra shown in (e).

4.1a, and 4.1b. In this system, the total conductance ($G^{\mathrm{LB}}_{\mathrm{tot}}$) is the sum of an intraband ($G^{\mathrm{LB}}_{\mathrm{intra}}(\omega)$) and an interband ($G^{\mathrm{LB}}_{\mathrm{inter}}(\omega)$) component. When the Fermi energy (E_F) is at the Dirac point, theory predicts SS interband transitions give rise to a frequency independent conductance of $G^{\mathrm{LB}}_{\mathrm{inter}} = \frac{1}{8}\frac{\pi e^2}{h}$ [56]. However, the area of the Fermi surface is zero yielding $G^{\mathrm{LB}}_{\mathrm{intra}} = 0$. When E_F is shifted away from the Dirac point, empty states suppress interband transitions at energies below $2|E_F|$, as illustrated in Fig. 4.1b, resulting in $G^{\mathrm{LB}}_{\mathrm{inter}}(\omega) = 0$ for $\omega < 2|E_F|$. Importantly, the f-sum rule [54] demands that the total spectral weight of the Dirac electrons ($\int_0^\infty G^{\mathrm{LB}}_{\mathrm{tot}} d\omega$) is conserved [102, 103]. Therefore, the loss of spectral weight in $G^{\mathrm{LB}}_{\mathrm{inter}}(\omega)$ must be compensated by a gain in $G^{\mathrm{LB}}_{\mathrm{intra}}(\omega)$, leading to:

$$G^{\mathrm{LB}}_{\mathrm{inter}} \cdot 2|E_F| = \int_0^\infty G^{\mathrm{LB}}_{\mathrm{intra}} \hbar d\omega. \tag{4.1}$$

It is customary to express the relationship between intraband spectral weight and Drude oscillator strength (D^s_{LB}) as:

$$\int_0^\infty G_{intra,LB}(\omega)\hbar d\omega = \frac{\pi}{30\Omega} D^s_{LB}, \tag{4.2}$$

which implies the simple relationship between E_F and D^s_{LB}:

$$D^s_{LB} = \frac{60\Omega}{\pi} G^{\mathrm{LB}}_{\mathrm{inter}} |E_F|. \tag{4.3}$$

The conductivity of the TI is dominated by the surface states, provide E_F is located outside of the bulk bands. It is customary to measure E_F relative to the Dirac point. Then, for p-type conductivity, E_F, defined relative to the Dirac point, cannot lie within the bulk bands. Therefore, for p-type (n-type) SS conduction, the maximum value of D^s_{LB}, occurs when the Dirac point is at the conduction band minimum (valence band maximum), and E_F is at the valence band maximum (conduction band minimum). Then, the energy that corresponds to the maximum value of E_F is simply E_g, with the maximum value of D^s_{LB} ($D^s_{\mathrm{LB,max}}$) given by $D^s_{\mathrm{LB,max}} = (N_S)\frac{60\Omega}{\pi} G_{\mathrm{TI}} E_g$, where N_S is the number of probed interfaces between systems with different topological indices. Here, $N_S = 2$ since optical transmission probes two topological surfaces, *i.e.* the interface between the film and the vacuum, and the film and the substrate.

The straightforward relationship between D_{LB} and E_F in Eqn. 4.3 is useful for estimating the Drude spectral weight that could arise from SS, and for intuitively understanding the spectral weight transfer in TI systems. Importantly, the resilience of the f-sum rule to external parameters has been experimentally verified numerous times in a prototypical surface state conductor: graphene. Even with gating, where additional charge carriers are introduced, the f-sum rule is found to be correct within the experimental error bars [94]. The reason for this is that the dominant effect of gating is a redistribution of spectral weight, while the increase in carriers is a relatively small perturbation. Importantly, TI materials are often not well modeled by linear bands. Instead, significant hexagonal warping effects are observed in Bi_2Te_3 and $(Bi,Sb)_2Te_3$ as well as asymmetry between the upper and lower portions of the Dirac cone [8, 100]. These combined effects modify the conductance from the constant value shown in Fig. 4.1c, and therefore change the value of D^s for a given E_F [56]. To more accurately estimate D^s_{max}, we have considered the optical response of a more realistic SS dispersion of a

similarly doped sample [56, 100]. This additional analysis suggests that $D^{s}_{\max}$ could be enhanced by approximately 25%, depending on the sample in question Sec. 4.5.

4.3 Results and Discussion

In light of the constraints on D imposed by the f-sum rules, we experimentally determined D and E_g of $(Bi,Sb)_2Te_3$ through a combination of terahertz time-domain spectroscopy (THz-TDS) and Fourier transform infrared spectroscopy (FTIR). Details of the sample growth and experimental techniques are included in Sec. 4.5. In Fig. 4.2a, we plot the frequency dependent conductance spectra $G(\omega)$ (real part of $\tilde{\sigma}(\omega) \times$ thickness) of our $(Bi,Sb)_2Te_3$ film from 2–18 meV, the relevant energy scale for the Drude response. The most prominent feature at all temperatures is the narrow resonance centered near 6 meV, which is attributed to a phonon. There is another, weaker phonon resonance, slightly higher in energy, at roughly 8 meV. The assignment of these phonon modes is discussed in Sec. 4.5 At energies below these features, we observe a relatively flat but finite $G(\omega)$ related to the Drude response.

To quantify the Drude oscillator strength D, we construct a Drude-Lorentz model to describe the conductance of the BST system:

$$G(\omega) = \frac{1}{15\Omega}\frac{D\tau}{1+(\omega\tau)^2} + \sum_{j=1}^{n}\frac{A_j\Gamma_j\omega^2}{(\omega^2-\omega_{0j}^2)^2+(\Gamma_j\omega)^2}, \tag{4.4}$$

where the first term describes the Drude response and the second term corresponds to Lorentzian resonances with amplitude A, width Γ, and center frequency ω_0. A representative Drude-Lorentz model fit is shown in Fig. 4.2b for the 6 K spectrum. The Drude-Lorentz models and the corresponding data at higher temperatures are shown in Sec. 4.5. To independently confirm the values of D obtained from the model, we also considered a multilayer model where the BST system consisted of two conducting surface layers and an insulating bulk Sec. 4.5. The Drude oscillator strength attributed to these conducting surface layers was consistent with the value of D extracted from the measured $G(\omega)$ spectra.

Above 150 K, both D and $1/\tau$ for $(Bi,Sb)_2Te_3$ (black points Fig. 4.2c and 4.2d) decrease as temperature is reduced. Since $D \propto \sqrt{n}$, for 2D Dirac states, the reduction in

D indicates a reduction in charge carriers, consistent with thermal activation at higher temperatures. The charge carrier density (n) extracted from Hall effect measurements on this film indicate p-type conduction, as is typical of $(Bi_{1-x}Sb_x)_2Te_3$ systems [100, 101], with thermal activation at T>150K (open red squares Fig. 4.2c). Moreover, the magneto-resistance data at 200K and 300K, shown in the inset to Fig. 4.2a, show a nonlinear trend with magnetic field B, suggesting multi-band transport, also consistent with the notion of thermally activated bulk states coexisting with SS. Furthermore, since thermally activated charge carriers are not topologically protected, it is likely that their presence would yield a lower mobility (larger $1/\tau$). Therefore, the simultaneous decrease in D and $1/\tau$ as the temperature is lowered, supports the notion that thermally activated charge carriers are frozen out, leaving only high mobility carriers. The Hall parameters n and μ for these high temperature data in Fig. 4.2 were fit only in the linear regime (-1 T<B<1 T).

Below 150 K, D and $1/\tau$ remain relatively constant near 0.13 meV and 2 THz, respectively. Importantly, our low temperature D value lies right at the threshold of $D^s_{\mathrm{LB,max}}\pm 10\%$ for $(Bi,Sb)_2Te_3$, indicated by the light gray bar in Fig. 4.2c. This latter fact indicates that the measured Drude spectral weight is consistent with a SS dominated response. Moreover, the low temperature value of D is roughly 5 to 10 times lower than most of those previously reported for other representative TIs (see Table 4.2), with the exception of a recent report in Cu-doped Bi_2Se_3 [105]. The next lowest experimentally measured D come from Bi_2Se_3 [52], in which the D values suggest E_F is in the bulk conduction band. However in this latter case, corrections to the Bi_2Se_3 SS band structure mentioned earlier [52] and the persistence of 2D topological SSs to well above the conduction band minimum [63], do imply D is consistent with a significant SS transport component in Bi_2Se_3.

To verify that the measured parameters D^{exp}=0.13 meV and n_{2D}^{exp}=$1.3\times10^{13}\mathrm{cm}^{-2}$ are consistent with surface dominated transport, we can compare our results to that expected from experimentally obtained SS dispersion of TI materials with a similar $(Bi,Sb)_2Te_3$ composition [100, 101]. For this comparison we will utilize Eqn. 4.3, and the relationship between E_F and and the carrier density of a single surface (n_{SS}) [94]:

$$E_F = \hbar v_0 \sqrt{4\pi n_{SS}}, \tag{4.5}$$

to directly relate E_F, n_{SS} and D via:

$$D^s_{LB} = (N_s)\frac{60\Omega}{\pi} G_{TI}\hbar v_0 \sqrt{4\pi n_{SS}}. \tag{4.6}$$

For direct comparison between transport and optics, we use $n_{SS} = n^{exp}_{2D}/2$, assuming the carriers were divided between two surfaces and v_0=3.8×10^{5}m/s, consistent with both photoemission and transport measurements of p-type SS carriers [77, 101]. These values yield D^s_{LB}=0.13 meV, exactly reproducing our measured value. Moreover, this analysis corresponds to E_F=0.22 eV, in close agreement with the measured E_G of 0.206 eV, suggesting the optical response is close to the constraints imposed by the sum rule analysis. If the additional contribution to D from the bulk bands is taken into account, in the regime where $E_F \approx E_G$, we recover our experimentally measured value of D when $E_F = 0.211$eV. This analysis, which is detailed in Sec. 4.5, suggests E_F penetrates only up to 5 meV into the bulk bands, and bulk carriers constitute only 2% of the total n_{2D}. Hexagonal warping, and other modifications to the SS dispersion, discussed more in Sec. 4.5, suggest that even smaller values of E_F, where $E_F < E_G$, may reproduce the measured D and n^{exp}_{2D} values. Alternatively, we considered the case that the optical response arises from the bulk valence bands. Prior work has shown that the bulk valence band structure in the $(Bi,Sb)_2Te_3$ system consist of of a light hole band (LHB) and heavy hole band (HHB) [34, 106, 107]. The effective masses of LHB and the HHB are 0.11m$_e$ and 1.0 m$_e$ respectively, and the top of the HHB is approximately 30 meV below the LHB [106, 107]. To recover the correct value of D for this sample, E_F would be 30 meV below the top of the LHB, However, this would yield an n_{2D} of 5 × 10^{12}cm^{-2}, over a factor of two smaller than what was measured.

Prior experiments have also pointed out that conventional SS may coexist with the topologically protected SS of a TI [63]. Typically, the conventional SS appear as a result of band bending, and are close in energy to the bulk bands, and contribute to conductivity when $E_F \approx E_G$. Therefore, the large magnitude E_F required to access the conventional SS, combined with their additional metallic response, would likely push D well above the limit imposed by f-sum rule analysis. It is therefore unlikely that our measured response has a significant component from the conventional SS.

Further evidence of a dominant topological SS contribution to the response of the $(Bi,Sb)_2Te_3$ system is identified in magneto-resistance measurements, plotted in the

inset to Fig. 4.2. At low temperature, the magneto-resistance data show linear behavior with B, indicative of single band transport. Moreover, the figure reveals weak antilocalization in (symmetrized) magnetoresistance measurements (*i.e.* the cusp at low-B field in the 2K data), which has been thought to be a hallmark signature topological SS transport [6]. However, theoretical work has shown that antilocalization may occur even in systems with bulk dominated transport, and therefore, anti localization by itself, cannot be considered conclusive evidence for surface states [108]. Despite this stipulation, the magneto-resistance data, in conjuction with the low value of D revealed from optics, are consistent with low temperature transport that is dominated by topologically protected SS.

The picture that emerges from the comparison of transport, optics and previously measured photoemission is that tdhe Dirac point is near the bottom of the conduction band, with E_F near the top of the valence band, as is illustrated in Fig. 4.1b. Likewise, we illustrate the bulk band structure consisting of two hole bands offset from the Γ point, with an electron band at the Γ point, as measured previously [100, 101, 107]. The relative positioning of E_F, the Dirac point, and bulk bands that we propose has been observed in similar, albeit more highly doped, $(Bi_{1-x}Sb_x)_2Te_3$ thin films [101]. Indeed, the distance from the Dirac point to the top of the Valence Band, as well as the v_0 in this latter work is consistent with our measurements. It is important to note that photoemission measurements of similarly doped samples often show that the Dirac point is below E_F [100], in contrast to our measurement of p-type carriers. This discrepancy can be understood in light of the aging effects, often observed TI systems, which generally shift the Dirac point downward relative to E_F. It is then likely that the capping layer of Se prevents the band bending, and the resulting accumulation layers, observed in other samples [63, 77] yielding a response dominated by p-type SS carriers. Unfortunately, this same capping layer prevents direct verification of this hypothesis in our particular sample via photoemission.

4.4 Conclusion

The totality of our data clearly show that $(Bi,Sb)_2Te_3$ alloys are a promising vehicle for advancing the field of TIs. In particular, the Drude oscillator strength lies at the threshold of the SS response upper bound, demonstrating the effectiveness of the alloy in reducing or eliminating bulk charge carriers. Furthermore, comparison of Drude parameters from optics to transport parameters from the Hall effect, coupled with weak antilocalization observed in low-temperature magneto-transport, shows consistency with surface transport with $v_0 \sim 4 \times 10^5$ m/s, in accord with ARPES results [101]. Therefore, our data imply $(Bi,Sb)_2Te_3$ is an optimal candidate for isolating SS properties in further studies of keen interest, such as magneto-optical measurements [57–59] and electrostatic modification of SS charge carrier density in electric field effect devices [109–111].

4.5 Supplementary Information

4.5.1 Optical conductivity of surface states

Optical conductivity in Dirac like systems, when E_F is at the Dirac point, arises from interband transitions, as illustrated in Fig. 1 of the main text. The standard Kubo formalism for calculating optical conductivity is given by [82]:

$$\sigma_1(\omega,\vec{q}) = \frac{1}{4\pi\omega}\int |\langle s|\,\hat{j}_x\,|s'\rangle|^2 \delta(\hbar\omega - \hbar\omega_{s,s'})d\vec{k} \tag{S1}$$

$$\hat{j}_x = ev\sigma_x \tag{S2}$$

where s and s' are the final and initial states, respectively, $\omega_{s,s'}$, is the difference in energy between the initial and final states, and $\hat{j}_x$ is the current operator. Importantly, $\langle s|\,\hat{j}_x\,|s'\rangle$ is related to the derivative of the overlap between s and s', with respect to energy. For the case of our modeled topological insulator (TI) system, the hexagonal warping and non-linearity increases the rate at which s and s' change as a function of momentum, therefore increasing the overlap of $\langle s|\,\hat{j}_x\,|s'\rangle$, and the corresponding conductivity at higher wavenumbers.

Within the framework of Kubo formalism, and taking into account the spin and momentum locking in TIs [89], we calculated the optical conductivity, assuming a sur-

face state dispersion of:

$$E(k,\theta) = \beta k^2 \pm \sqrt{v_0^2 k^2 + \lambda^2 k^6 \cos^3(3\theta)}. \tag{S3}$$

The parameters β and v_0 are the quadratic and linear component of the dispersion, respectively, while λ is related to the hexagonal warping. Eqn. S3 is similar to that used in [56], with the addition of a quadratic correction. Utilizing the relationship between momentum and spin of SS carriers [89], the wavefunction of the SS charge carriers can be determined and evaluated in the Kubo framework, described by Eqn. S1. Moreover, when E_F is at the Dirac point ($E_F = 0$), interband transitions are allowed at all energies. The resulting conductivity is then given by:

$$\sigma_1(\omega) = \frac{e^2}{32\hbar\pi\omega^2} \int_0^{2\pi} v_0^2 k^2 \frac{\omega^2/4 - 2\lambda^2 k^6 \cos^3(3\theta) + 9\lambda^2 k^6}{\omega^2/4 + 2\lambda^2 k^6 \cos^3(3\theta)} d\theta, \tag{S4}$$

where k is a function of θ, and is obtained by solving the equation

$$v_0^2 k^2 + \lambda^2 k^6 \cos^3(3\theta) = \frac{\omega^2}{4}. \tag{S5}$$

A closed form of $\sigma_1(\omega)$ can then be obtained by expanding about small λ. This derivation was guided in large part by prior theoretical work on the optical response of Dirac electron systems [56, 112].

4.5.2 Extended sum rule analysis of surface states

The modifications to the optical conductance described in the previous section are useful for extending the sum rule constraint, described in the main text, to systems characterized by hexagonal warping and band asymmetry. Accordingly, we have considered the optical conductance arising from three different SS dispersions, shown in Fig. 4.3a, 4.3b and 4.3c. The dispersion shown in Fig. 4.3a is the same as that used in the main text for establishing the sum rules. In Fig. 4.3b, the dispersion is modified to include minor hexagonal warping, and a smaller v_0. Lastly, in Fig. 4.3c, we show the surface state dispersion of an n-type $(Bi_{0.5}Sb_{0.5})_2Te_3$ crystal, extracted from photoemission data in [100], which was characterized by significant hexagonal warping and band asymmetry. Although not comprehensive, examining these dispersions and their

corresponding optical response may provide some intuition as to how features of the SS dispersion influence the optical conductance.

In these schematics, we have also indicated the bulk band dispersion with the blue dotted lines. The bulk band structure we show is based on combined photoemission and transport [100, 106, 107]. These data indicate the presence of a light and heavy hole band that are both offset from the Γ-point, and an electron band centered in the Brillouin zone. The relative positioning of E_F, the Dirac point, and the bulk bands in Fig. 4.3a and 4.3b illustrate scenarios consistent with our experimental observation of p-type carriers. The alternative n-type picture that was measured in [100] is illustrated in Fig. 4.3c.

The conductance spectra, calculated when $E_F = 0$, corresponding to the SS dispersions shown in Fig. 4.3a,4.3b and 4.3c are plotted as the dotted line in Fig. 4.3d, 4.3e and 4.3f, respectively. However, the schematic shown in Fig. 4.3a-c shows E_F shifted away from the Dirac point, yielding a system where hole (electron) states are depopulated (populated), as in Fig. 4.3a and 4.3b (Fig. 4.3c). For interband transitions to occur in these systems, it must be possible to excite an electron from a populated hole state, to a depopulated electron state, while conserving momentum ($\vec{k}$). Thus, the populated or depopulated states block interband transitions below a threshold energy (ω_{th}). For symmetric bands, $\omega_{th} = 2|E_F|$. In an asymmetric SS dispersion, ω_{th} must be determined on a case by case basis. The blocked interband transitions below ω_{th} suppresses the optical conductance. However, the f-sum rule, described in the main text demands that spectral weight cannot be lost, but is instead transferred into the Drude oscillator. The conductance spectra corresponding to the schematics in Fig. 4.3a-c, where $|E|F = E_g$, are indicated by the solid lines in Fig. 4.3d-f, respectively.

A salient feature in these conductance spectra is that increasing the hexagonal warping, increases the upturn in Conductance as ω increases. Accordingly, a higher hexagonal warping corresponds to a larger area of suppressed spectral weight, resulting in a larger Drude spectral weight (D), which is indicated in Fig. 4.3d-f. In addition, for comparison with our experimental data, we can extract the SS carrier density (n_{SS}) from the extracted SS dispersion via:

$$n_{SS} = \frac{1}{8\pi^2}\int_0^{2\pi} k_F^2(\theta)d\theta.$$

Since we are probing two surfaces, the total two dimensional carrier density (n_{2D}) is

given by $n_{2D} = 2 \cdot n_{SS}$, and is indicated in Fig. 4.3d-f. The experimentally obtained values were $D^{exp} = 0.13meV$ and $n_{2D}^{exp} = 1.3 \times 10^{13} cm^{-2}$. The schematic shown in Fig. 4.3a predicts D and n_{2D} values that closely match what was measured, however, for an exact match E_F would have to be within the bulk valence band. In contrast, slight modifications to the SS dispersion as in Fig. 4.3b overestimates the values of D and n_{2D} when $|E_F| = E_G$. Instead, our experimental values are reproduced when $|E_F| = 0.19eV$, a value smaller than E_G, suggesting our measurements are consistent with a completely surface dominated response, without bulk contributions. Interestingly, the n-type schematic shown in Fig. 4.3c corresponds to a D even larger than what we measured, but significantly underestimates n_{2D}, due to the reduced area of the Fermi surface. Thus, this picture is inconsistent with our measurements.

4.5.3 Comparison of D and n_{2D} for linear SS bands

In the main text, our analysis of D and n_{2D}, implied an $|E_F|$ of 221 meV, thereby suggesting E_F resides 16 meV in the bulk valence band (BVB). However, this estimate is incomplete since it neglects contributions to D and n_{2D} from the bulk bands, which are significant when E_F is at the edge of the (BVB). To illustrate this latter effect, we have seperately calculated D and n_{2D}, as a function of E_F for the three elements comprising the composite system: SS bands, the light hole band (LHB), and the heavy hole band (HHB). The effective masses of the LHB and the HHB, as well as their relative position, were taken from [106, 107] and used to assemble the schematic band structure shown in Fig. 4.4a. To calculate D and n_{2D} from this schematic band structure, we utilized the well known relationships between m^*, E_F, n_{2D} and D for bulk bands [54, 65, 98], and the analagous relationships for linear bands detailed in the main text. The resulting E_F dependent values of D and n_{2D} are plotted in Fig. 4.4b and 4.4c, respectively. The black, red, and green lines indicate the individual contribution from the SS, the LHB and the HHB, respectively. The value of D or n_{2D} that we would expect to measure is the sum of these these latter three contributions, which is indicated by the dotted gray line. Lastly, the blue line indicates our experimentally obtained value. Therefore, a more realistic value of E_F, where the combined bulk and surface contributions are taken into account corresponds to the point where the dotted gray line intersects the blue line. In the case

of the D, the intersection occurs at E_F=211 meV, which is only 5 meV into the LHB. The total carrier density corresponding to this value E_F is $1.16\times10^{13}\text{cm}^{-2}$, in close agreement with our experimentally measured value of $1.28 \times 10^{13}\text{cm}^{-2}$. Moreover, the surface carriers in this scenario account for approximately 98% of the total carriers, suggesting a highly surface dominated response.

Alternatively, we considered the possibility that the carriers we measure arise solely from the bulk bands, where the resulting E_F dependent D and n_{2D} spectra are plotted in Fig. 4.4d and 4.4e, respectively. Again, the red and green lines indicate the contributions from the LHB and the HHB, and the sum of these two bulk contributions is the dotted gray line. In these plots, the dotted gray line intersects the measured D at $E_F = 30\text{meV}$. However, this value of E_F would imply an n_{2D} of $5 \times 10^{12}\text{cm}^{-2}$, less than half of what was measured. In fact, it was found that neither of the bulk valence bands, in isolation, could consistently reproduce our measured D and n_{2D} values. Even so, it was possible to adjust the relative positioning of these bands to produce a multi-band response that matches our measurements. However, such a multi-band system would contradict the linear behavior of the Hall resistance, discussed in the main text, which indicates a single carrier species. This analysis emphasizes the notion that our data can be consistently described by assuming a SS dominated response, but not bulk.

4.5.4 Drude-Lorentz fitting of the conductance spectra

In the main text, only the Drude-Lorentz fitting of the 8K conductance data was shown. The same fitting procedure was employed to extracte the value of D and scattering time τ for all data sets that are shown in Fig. 2c and 2d of the main text. For completeness, the Drude-Lorentz fits to the conductance spectra at all measured temperatures are shown in Fig. 4.5

The most prominent features of these spectra are the two phonons at 6 meV and 8 meV. The lower energy resonance has a center frequency in close agreement with the E_u^1 phonon mode of Bi_2Te_3 [113], while the weaker higher energy mode has two possibilities. The center frequency of this latter mode suggests assignment to either the E_u^1 mode of Sb_2Te_3, or the A_{1g}^1 mode, which is at similar energies in both stoichiometric compounds [113]. The A_{1g}^1 mode is typically only Raman active, however, this mode

may become IR active in the $(Bi,Sb)_2Te_3$ alloy due to the broken translational symmetry introduced via Bi:Sb substitution.

4.5.5 Sample Growth

The $(Bi,Sb)_2Te_3$ films in this study were prepared using molecular beam epitaxy, with a composition of approximately 54% Sb to 46% Bi. These films were grown along the c-axis with a thicknes of 58nm on an insulating InP (111) substrate, where the InP oxide was desorbed under a flux of As to retain a smooth surface for the TI growth. Our films were grown under a Te overpressure, with a Te/(Bi+Sb) beam equivalent pressure ratio of about 7. These growth conditions were determined to yield samples that could be gated through the Dirac point, and possessed insulating resistance vs. temperature curves. The film was capped with a 10nm insulating amorphous Se layer at room temperature, which prevents oxidation and has negligible effects on low energy optical spectroscopy measurements, as demonstrated in [52]. We confirmed the opticaly inert nature of the Se capping layer by also measuring an InP substrate with a thin layer of Se, and comparing it to bare InP. Further characterization of the film was done using x-ray diffraction, and low temperature magneto-transport. Likewise, the film thickness was determined by X-ray reflectivity, and the composition by secondary ion mass spectroscopy measurements on similar samples.

4.5.6 Spectroscopic Technique

The energy range covered by the Terahertz-Time domain spectroscopy (THz-TDS) and fourier transform infrared (FTIR) experiments are roughly 2-10 and 5-900 meV, respectively. The complex, frequency dependent optical constants of the film ($\tilde{\varepsilon}(\omega)$,$\tilde{n}(\omega)$,$\tilde{\sigma}(\omega)$, which are all algebraically related [82]), were determined seperately for the THz-TDS and FTIR experiments, and then merged together. To obtain the optical constant of the film for this two layer system (film+substrate), it was necessary to first precisely determine the optical constants of the InP substrate at each temperature. For the FTIR data, we constructed a multi-layer, multi-oscillator, Kramers-Krònig consistet model fit of the raw transimssion data, yielding the optical constants of the film [114].

In the THz-TDS experiment, we measure the time-resolved transmitted electric field, from which the optical constants are calculated directly [115].

4.5.7 Energy Gap

Establishing the maximum Drude spectral weight required a value for E_G, which can be readily determined from our data. In Fig. 4.6a we plot $(\varepsilon_2(\omega))^2$ from 75-900 meV, where $\varepsilon_2(\omega)$ is the imaginary part of the complex, frequency dependent dielectric function, $\tilde{\varepsilon}(\omega) = \varepsilon_1(\omega) + i\varepsilon_2(\omega)$. E_G is found from the x-intercept of a linear fit to $(\varepsilon_2(\omega))^2$ in the linear onset regime, $\simeq 200-250$ meV [55]. The resulting value of E_G is plotted as a function of temperature in Fig. 4.6b. The data show a relatively temperature independent E_G of 206.5$\pm$3.4 meV, in contrast to the significant temperature dependence of E_G observed in other works [116]. Also noticeable in the $(\varepsilon_2(\omega))^2$ spectra are distinct resonant features at $\omega > E_G$, which are suggestive of Van Hove singularities in the $(Bi,Sb)_2Te_3$ band structure, but are not discussed in detail in this work [55].

4.5.8 Three layer model of the TI system

Our method of extracting the optical constants, and thus D, are consisten with silimar analysis in the literature [52, 87, 104]. However, an assertion of SS conductance requires a 3-layer model for the TI film, *i.e.* two conductive surfaces and one insulating bulk layer, whereas in the main text, the value of D is extracted using a model consisting of one layer and a single Drude, where a single layer accounts for the effect of both surfaces. Thus, to confirm the plausibility that theDrude conductance is due to SS electrons, the THz-TDS transmission was alternatively modeled assuming 3-layers + substrate: (1) 1 nm surface layer, (2) 58 nm bulk layer, (3) 1 nm surface layer, and (4) 0.5 mm InP substrate, as illustrated schematically in Fig. 4.7. The Se capping layer was neglected since, as stated earlier, it was found to have a negligible effect on the optical response of the system. We ascribe single (identical) Drude oscillators to layers (1) and (3), with the bulk layer (2) having two lorentzian oscillators to describe the phonons. The choice of 1nm for the surface layers is based on theoretical predictions [36], though the choice in SS thickness has negligible effect, as long as it is much less than the optical

penetration depth [67]. Under this 3-layer modeling, the D extracted for each surface of the 6K THz-TDS transmission is 0.07 meV, for a total (D^s_{3layer}) of 0.14 meV. This is in good agreement with D=0.13 meV extracted from the conductance that was calculated directly from the THz-TDS data. The agreement between these two methods, and the proximity to the threshold of D^s_{max}, confirms the plausibility that the Drude conductance observed is dombinated by the topological SSs.

4.5.9 Boltzmann derivation of the Drude spectral weight

The f-sum rule analysis, detailed in the main text, offers an intuitive way to understand limits on the Drude spectral weight in Dirac systems. However, the value of D can be alternatively derived using the Boltzmann equation, which requires only that the shape of the Fermi surface is known, rather than the entire band structure. With this knowledge of the Fermi surface, σ_{xx} is given by the Boltzmann equation:

$$\sigma_{xx} = \frac{e^2}{i\omega - 1/\tau} \int v_x^2 \frac{k_F}{|\partial E/\partial k|} d\phi \tag{S6}$$

where D is given by:

$$D = e^2 \int v_x^2 \frac{k_F}{|\partial E/\partial k|} d\phi. \tag{S7}$$

With this equation, D can be calculated simply from the SS dispersion, given by Eqn. S3. We therefore extracted the SS dispersion of a number of TI systems from photoemission data, which are shown in Fig. 4.8b, with the corresponding Fermi surface at $E_F = E_G$ shown in Fig. 4.8c. The resulting values of D are plotted as a function of E_F in Fig. 4.8c, with the energy gap of the different materials indicated by the arrows, colored to match their respective system. Using the same reasoning as in the main text, the estimated maximum value of D without bulk contributions is achieved when $E_F = E_G$. The maximum values of D obtained from the Boltzmann derivation ($D^s_{Boltz,max}$) are shown next to the experimentally obtained values of D in Table 4.2, a modified verion of the table shown in the text. The results of this complementary analysis of D are consistent with our previous conclusions.

4.6 Acknowledgements

Sample growth and characterization at Penn State was supported by DARPA (N66001-11-1-4110), ONR (N00014-12-1-0117), ARO-MURI (W911NF-12-1-0461) and (ECS-0335765). Work at UCSD is supported by DOE-BES.

Chapter 4 is a reprint of material published in *Physical Review Letters* **115**, 116804 (2015). K.W. Post, B.C. Chapler, M.K. Liu, J.S. Wu, H.T. Stinson, M.D. Goldflam, A.R. Richardella, J.S. Lee, A.A. Reijnders, K.S. Burch, M.M. Fogler, N. Samarth, and D.N. Basov. The dissertation author was the primary researcher and author of this material.

Table 4.1: Comparison of experimental Drude oscillator to sum rule limit. Bulk band gap E_g, experimental Drude oscillator strength D from transmission based experiments, modeled Drude oscillator strength D^s_{3layer} where conductance is assumed to be from 2 topological surfaces with an insulating bulk, and theoretical upper bound of the free Dirac SS Drude oscillator strength $D^s_{\text{LB,max}}$ of prototypical strong TIs obtained using the bulk energy gap, and assuming bands with linear dispersion. Values of D are all taken from low-temperature data (6–20 K). All units are meV. †The results of Ref.[67] are from reflection based experiments, and thus only one topological surface is considered.

TI material	E_g	D	D^s_{3layer}	$D^s_{LB,\text{max}}$	Refs.
Bi_2Se_3	300	0.5–0.70	–	0.17	[7, 52]
Bi_2Te_3	142	1.26	–	0.08	[98]
$Bi_{1.5}Sb_{0.5}Te_{1.8}Se_{1.2}$	340	1.42	–	0.20	[104]
$Bi_2Te_2Se^{\dagger}$	290	–	0.83	0.08	[67]
$Bi_{0.92}Sb_{1.08}Te_3$	207	0.13	0.14	0.12	This work
Bi_2Se_3	300	0.09	–	0.17	[105]

Table 4.2: Comparison of experimental Drude oscillator to limit from Boltzmann derived conductivity. The Bulk band gap E_g, experimental Drude oscillator strength D^{exp} from transmission based experiments, modeled Drude oscillator strength D^s_{3layer} where conductance is assumed to be from 2 topological surfaces with an insulating bulk, and theoretical upper bound of the Drude oscillator strength $D^s_{\text{Boltz,max}}$ of prototypical strong TIs obtained using the Boltzmann derived conductivity, the bulk energy gap, and the SS dispersion shown in Fig. 4.8a. Values of D are all taken from low-temperature data (6–20 K). All units are meV. †The results of Ref.[67] are from reflection based experiments, and thus only one topological surface is considered.

TI material	E_g	D^{exp}	D^s_{3layer}	$D^s_{\text{Boltz,max}}$	Refs.
Bi_2Se_3	300	0.09–0.70	–	0.17	[7, 52, 87, 105]
Bi_2Te_3	142	1.26	–	0.09	[98]
$Bi_{1.5}Sb_{0.5}Te_{1.8}Se_{1.2}$	340	1.42	–	0.34	[104]
$Bi_2Te_2Se^{\dagger}$	290	–	0.83	0.14	[67]
$Bi_{0.92}Sb_{1.08}Te_3$	207	0.13	0.14	0.15	This work

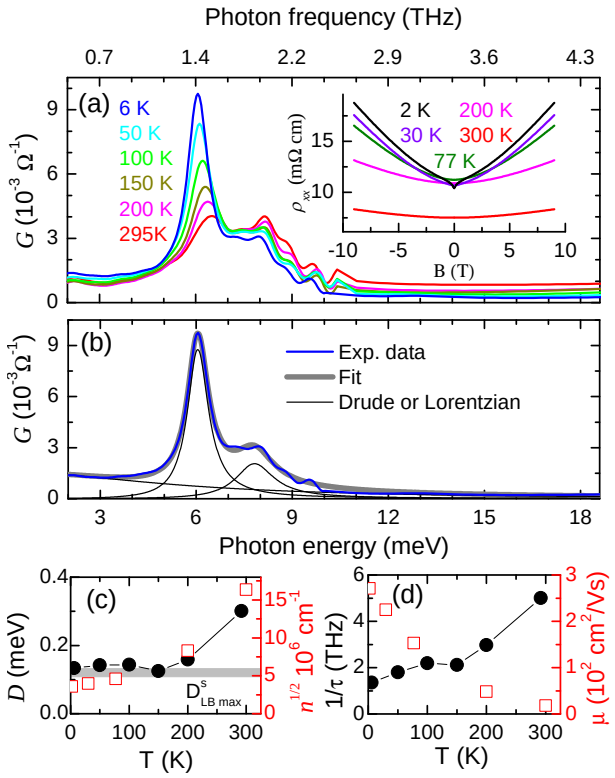

Figure 4.2: Measured conductance spectra and extracted oscillator parameters from a TI thin film. a) Temperature dependent spectrum of the conductance of $(Bi,Sb)_2Te_3$ obtained from THz-TDS and FTIR. The inset shows (symmetrized) DC magneto-resistivity data for this film. The "cusp" at low-B field in the 2 K data is indicative of weak antilocalization. b) Drude-Lorentz model fit (Eq. 4.4) (gray) of the 6 K experimental conductance (blue). Individual Drude or Lorentzian oscillators are displayed as thin black lines. c) Temperature dependence of the Drude oscillator strength D (black points) corresponding the the left axis, and square root of the charge carrier density n (open red squares) extracted from Hall effect measurements, corresponding the the right axis. The upper bounds for the Drude response of the linear SS ($D^s_{\mathrm{LB,max}} \pm 10\%$), and more realistic estimate of the SS contribution including hexagonal warping ($D^s_{\mathrm{BST,max}}$) in $(Bi,Sb)_2Te_3$, are indicated by the light gray and dark gray bars, respectively. d) Temperature dependence of the free carrier scattering rate $1/\tau$ from optics (black points, left axis) and charge mobility μ from Hall effect measurements (open red squares, right axis).

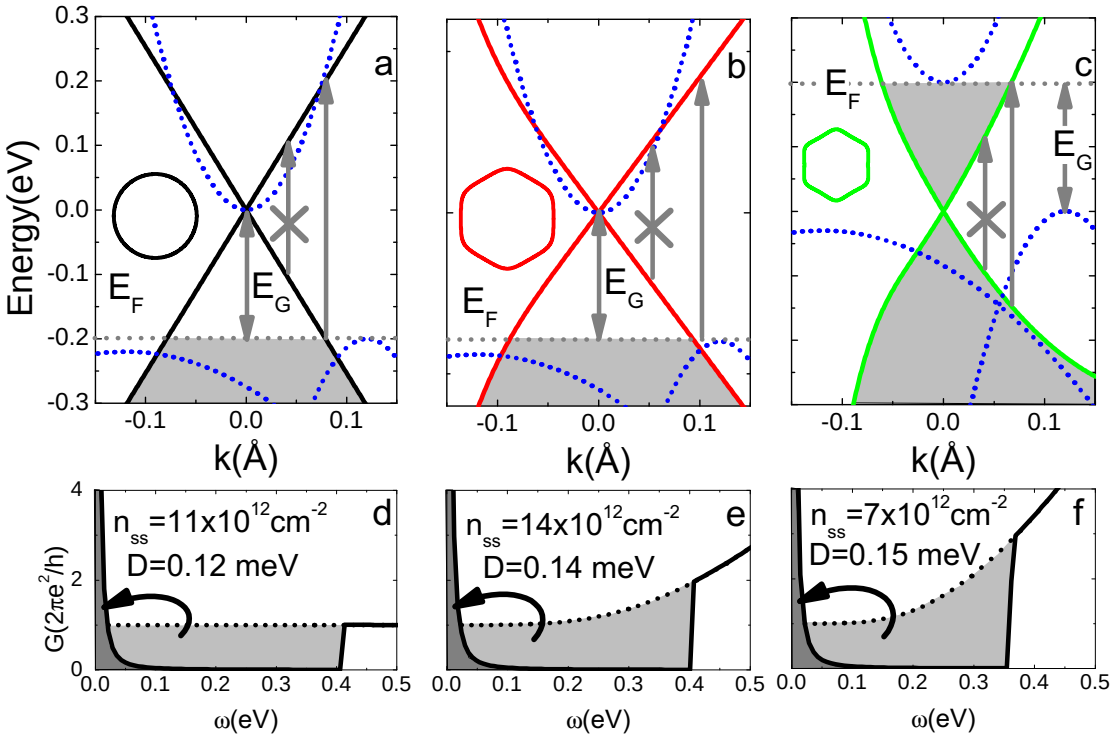

Figure 4.3: Sum rule constraints on surface state response for three modeled band structures. Panels (a), (b) and (c) schematically show the SS dispersion and bulk band structure corresponding to different experimental scenarios. (a) shows a SS dispersion without hexagonal warping, where the Dirac point is at the bottom of the bulk conduction band. (b) shows a dispersion similar to (a), with the addition of minor hexagonal warping and a slightly smaller v_0. (c) shows the SS dispersion, extracted from [100], where the Dirac point as at the same energy as the bulk valence band, and E_F is at the bottom of the bulk conduction band. The optical conductance corresponding to each of the schematics (a), (b) and (c), are shown in (d), (e) and (f), respectively. In (d),(e) and (f), the dotted line shows the predicted conductance when E_F is at the Dirac point, whereas the solid line indicates the conductance expected when $|E_F| = E_G$, as indicated in the corresponding schematics.

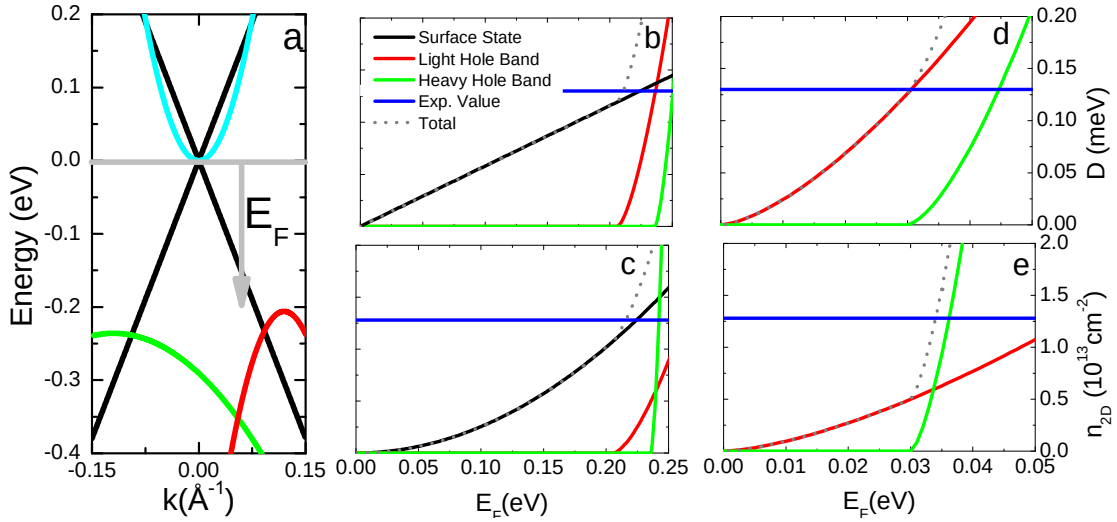

Figure 4.4: A schematic band structure of the measured $(Bi,Sb)_2Te_3$ thin film is shown in (a). The surface state band, the conduction band, the light hole band and the heavy hole band are indicated by the black, cyan, red and green lines, respectively. The E_F dependent values of D and n_{2D} that would be expected to arise from the composite bulk and surface response of this system are plotted in (b) and (c), respectively. In (b) and (c), E_F is defined relative to the Dirac point. Alternatively, the E_F dependent D and n_{2D} that would be expected in the absence of the SSs are plotted in (d) and (e), respectively. In these latter two panels, E_F is defined relative to the top of the light hole band. In panels (b-e) the blue line indicates the experimentally measured value, while the black, red and green lines indicate the isolated contribution to the D or n_{2D} spectra from the SS, the light hole band and the heavy hole band respectively while the dotted gray line indicates the sum of these latter three contributions, and the value that we would expect to measure.

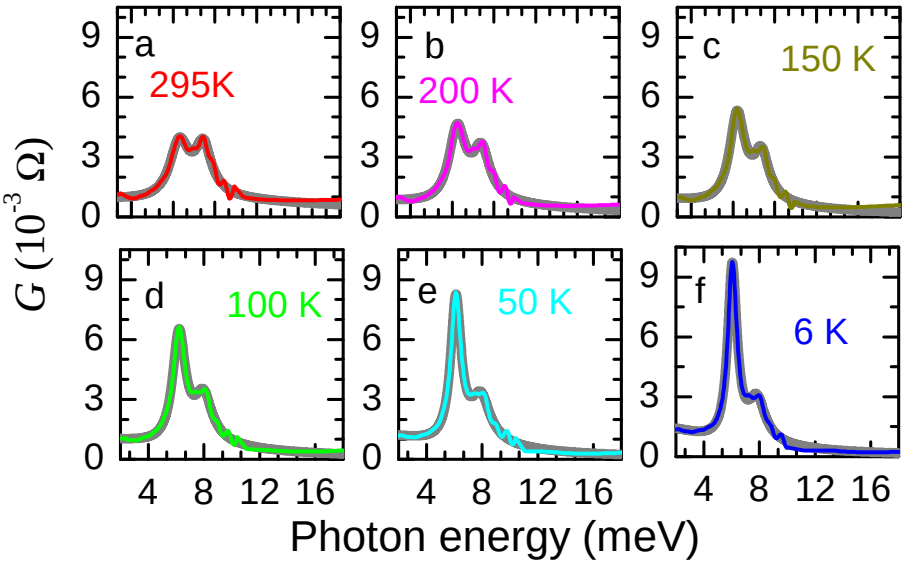

Figure 4.5: The experimental conductance spectra of $(Bi,Sb)_2Te_3$ (colored lines) are shown for all measured temperatures, along with the Drude-Lorentz fit (gray lines).

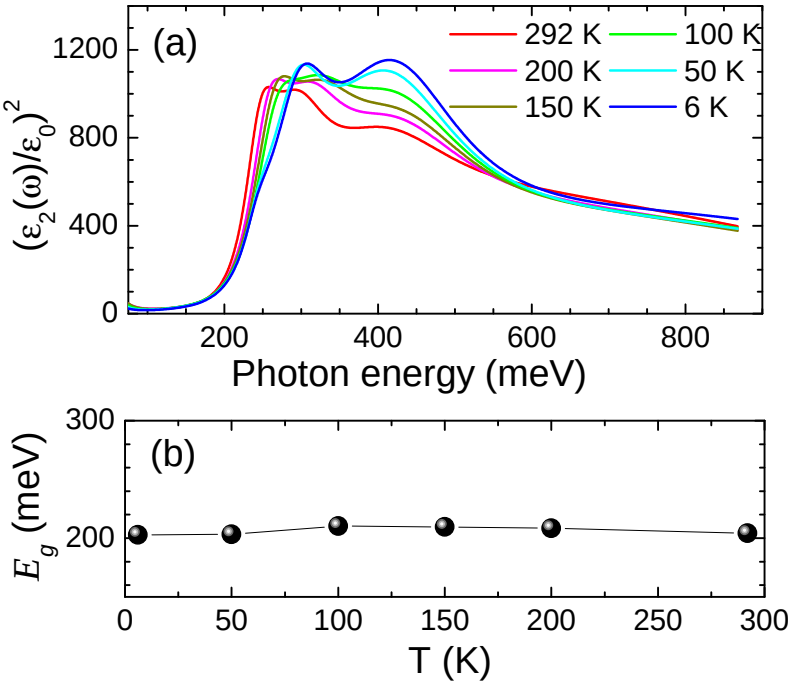

Figure 4.6: The energy gap of $(Bi,Sb)_2Te_3$ thin film determined from $(\varepsilon_2/\varepsilon_0)^2$. Panel (a) shows the $(\varepsilon_2/\varepsilon_0)^2$ spectra at all measured temperatures, where the lienar region near 200 meV indicates the onset of interband transitions. The magnitude of E_G is extracted from these spectra using a linear fit to $(\varepsilon_2/\varepsilon_0)^2$ where teh x-axis intercept corresponds to the value of E_G. E_G extracted using this procedure is plotted as a function of temperature in (b).

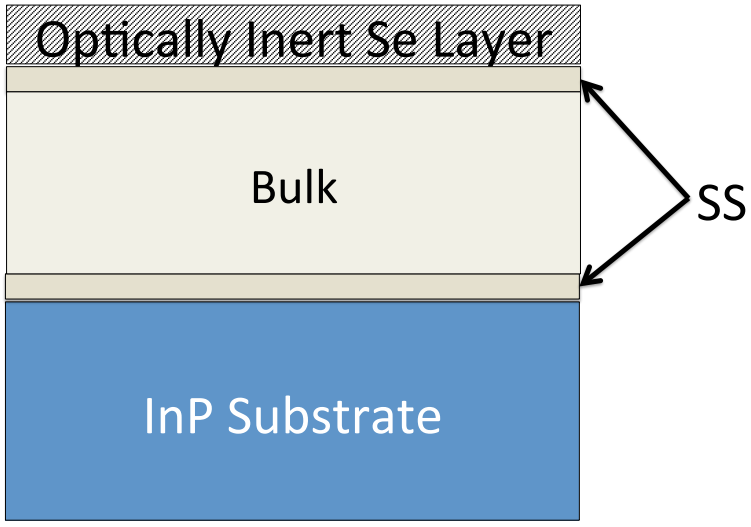

Figure 4.7: A schematic of the 3 layer BST+Substrate model that was used for extracting D. The top Se capping layer is optically inert, and was thus not considered in the model. The BST SS layers consisted ofa single Drude oscillator, with identical values of D and τ. The model for the BST bulk included only two lorentzian oscillators to capture the phonon modes. The InP substrate was measured and characterized separately, without the BST system.

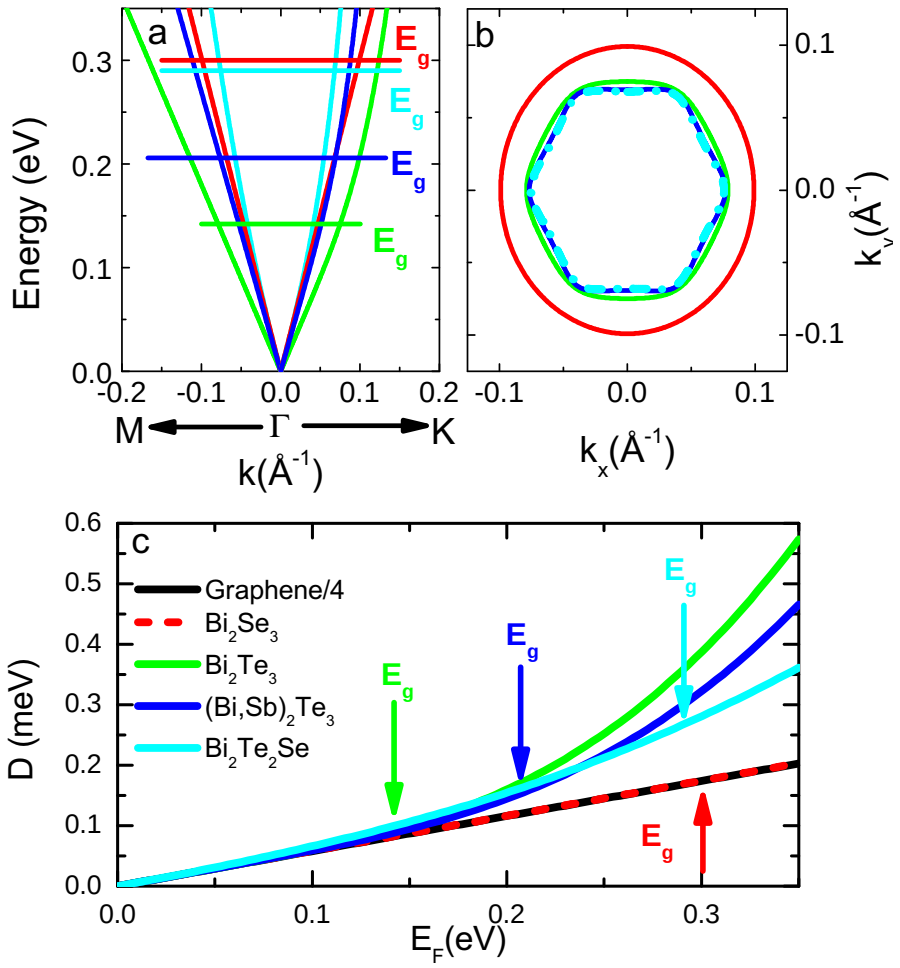

Figure 4.8: The SS dispersion above the Dirac point, which was extracted from photoemission data for four different TI systems[7, 8, 34, 80, 85, 100], is shown in (a). The lines, colored to match their respective system, indicate the bulk energy gap, with the Fermi surface corresponding to $E_F = E_G$ plotted in (b). The value of D, extracted from the SS dispersion using Eqn. S7, is plotted as a function of E_F in (c), with the bulk energy gap indicated by the arrows, colored to match their respective system.

Chapter 5

On electronic correlations and pressure induced metallicity in $LaMnPO_{1-x}F_x$ revealed via infrared spectroscopy

Abstract

We spectroscopically investigated the energy gap of the correlated antiferromagnetic insulator $LaMnPO_{1-x}F_x$ (x=0.0 and 0.04) as a function of temperature and pressure, separately, in conjunction with many body electronic structure calculations. These results show that the electronic structure in all measured regimes is well described by a model that includes both Mott-Hubbard interactions and Hund's rule coupling. Moreover, we find that by appying external pressure, thereby reducing the effective Mott-Hubbard interaction and Hund's coupling, the energy gap in $LaMnPO_{1-x}F_x$ can be fully closed, yielding a metallic state.

5.1 Introduction

Progress in the physics of correlated electron systems is often initiated by the discovery of new materials that feature complex interplay between charge, spin and orbital degrees of freedom. One such class of materials are the recently synthesized Mn-pnictides. Initial reports on the insulating materials $BaMn_2As_2$, $CaMn_2Sb_2$, LaMnPO, LaMnAsO and LiMnAs suggests that these compounds possess rich phase diagrams, highlighting the importance of electronic correlations [117–125]. Typically, these systems form as antiferromagnetically (AF) ordered insulators with many bands residing in the vicinity of the Fermi energy. The electronic correlations of such multi-band systems are often not well described solely with the Hubbard interaction (U), which only considers Coulomb repulsion of interacting carriers. Rather, the interaction of the carriers through the spin channel, via Hund's coupling (J_H) may also be necessary [126]. In the case of LaMnPO, recent work has suggested that it is a Mott-Hund's insulator, meaning both U and J_H act in concert to reproduce the observed insulating ground state[127, 128]. Accordingly, this new system warrants detailed examination, as many exotic phenomena, such as quantum criticality, phase separation, and high temperature superconductivity often appear when correlated antiferromagnetic systems are metallized.

In this work, we have spectroscopically probed the energy gap (E_{Gap}) of the AF insulator LaMnPO in the high pressure (HP) and high temperature (HT) regimes. The power of infrared spectroscopy, in the context of unresolved issues related to LaMnPO, is that it is the only experimental technique that can directly probe the electronic band structure at both high pressures and elevated temperatures. These measurements were also carried out on $LaMnPO_{0.96}F_{0.04}$, as doping in other correlated AF systems has frequently led to exotic phenomena [53]. Our results reveal that E_{Gap} in both undoped and doped LaMnPO, is reduced from 1.0 eV in the AF state, to 0.85 eV in the para-magnetic (PM) state at 725K, a reduction of only 15%. In contrast, by applying pressure, E_{Gap} in $LaMnPO_{1-x}F_x$ (x=0.0, 0.04) is systematically reduced, yielding a full gap collapse above 20 GPa. The combined high pressure and high temperature measurements show that the band collapse is not caused by the elimination of AF order or the pressure induced structural transition near 16.2 GPa. The optical data, combined with DFT+DMFT calculations establish a realistic description of the LaMnPO ground state, and provide

quantitative estimates of the U and J_H that govern the electronic structure. Additionally, we can unambiguously show that the emergent charge carriers at high pressures arise from a collapsed band within the bulk, thereby excluding alternative interpretations of the metallic state [121, 129].

5.2 Experimental Techniques and Discussion

5.2.1 Sample Growth.

Single crystals of $LaMnPO_{1-x}F_x$ were grown from a NaCl-KCl eutectic flux. The crystals formed as thin plates of dark luster with typical dimensions of 1mm $\times$ 1mm $\times$ 5μm. The sample thickness of $5\mu m$ was confirmed both by modelling the raw transmittance spectra while matching the periodicity of the interference fringes and by inspection. Doping with fluorine was accomplished by introducing MnF_2 powder to the samples prior to the crystal growth process. The F concentration of the synthesized crystals was determined via potentiometric measurements, as described previously [121], and the crystal structure was confirmed by single crystal x-ray diffraction.

5.2.2 High Temperature Measurements

Transmittance spectra of undoped and doped LaMnPO were measured from 0.01 to 1.5 eV, at temperatures ranging from 295K to 450K. The measurements of undoped LaMnPO, in the spectral range near E_{Gap} (0.8 eV $< \omega <$ 1.1 eV) were extended up to 725K using a custom elevated temperature sample stage. The raw transmittance data for undoped and doped LaMnPO, at 295K, are shown in Fig. 5.1a and 5.1b, respectively. The magnitude of E_{Gap} is extracted from the absorbance (αt), where α is the absorption coefficient of the material, and t is the sample thickness. Assuming incoherent transmittance, as appropriate in the case of limited experimental resolution or non-parallel crystal surfaces, absorbance is related to the absolute transmittance $T(\omega)$ and reflectance $R(\omega)$ via [130]:

$$T(\omega) = \frac{(1-R(\omega))^2 e^{-\alpha t}}{1-R(\omega)^2 e^{-2\alpha t}}. \tag{5.1}$$

Near the energy gap, where $R(\omega)$ is a nearly frequency independent value of R_0 [82], the lineshape of αt is approximately given by $-\ln(T(\omega))$. The $(1-R_0)^2$ correction to the $(\alpha t)^2$ spectra, which accounts for the reflectivity at the interface between the sample and the high pressure medium, is within the error bars of E_{Gap}, as discussed in section5.5. Likewise, since αt is large near the band gap, the denominator $1-R(\omega)^2 e^{-2\alpha t} \approx 1$. In the case of a direct gap material, the x-axis intercept of a linear fit to $(\alpha t/\omega)^2$ yields E_{Gap} [55]. The $(\alpha t)^2$ spectra (colored lines), corresponding to the measured values of transmittance, are plotted in Fig. 5.1c and 5.1d, along with the linear fits to $(\alpha t/\omega)^2$ (dashed gray lines).

The values of E_{Gap} obtained from the absorption spectra are plotted as a function of temperature in Fig. 5.1e. The shadowed region in the inset of Fig. 5.1e highlights an area in the vicinity of the bulk Neél temperature (T_N) of 375K$\pm$5K. There is no abrupt change in E_{Gap} upon crossing the bulk AF to paramagnetic (PM) transition in either the undoped or doped samples. Additionally, E_{Gap} of the doped samples follows a trajectory very similar to the undoped sample, albeit at a slightly lower energy.

The resilience of E_{Gap} to temperature suggests that long-range AF correlations do not play a major role in defining the electronic structure of LaMnPO. However, prior work has demonstrated that short range AF correlations persist up to 700K [127]. We explored the effect of these remaining AF correlations on E_{Gap} by measuring the transmittance of undoped LaMnPO, at temperatures up to 725K. There is a slight discontinuity in the temperature dependence of E_{Gap} between 450K and 500K, which we attribute to changes in the experimental setup, necessary to accommodate temperatures above 450K. In this extended temperature range, E_{Gap} of undoped LaMnPO monotonically decreases with increasing temperature. Upon reaching the completely PM state at 725K [127], the energy gap is only 0.85 eV, which is 0.15 eV lower than E_{Gap} at 295K.

The value of E_{Gap} predicted from DFT+DMFT calculations in the AF (PM) state is indicated by the blue triangles at 300K (700K) with the corresponding band structure calculations shown in Fig. 5.1f (5.1g). These calculations predicted that the elimination of AF order reduces E_{Gap} by 0.12 eV, closely matching our experimentally measured values in the PM state. Therefore, while it is likely that the short-range AF correlations contribute to the 1.0 eV energy gap in $LaMnPO_{1-x}F_x$, they cannot produce it alone.

Rather, the energy gap is stabilized primarily by the Hubbard U in concert with the Hund's J_H. This stands in stark contrast to theoretical work on the cuprates, where it has been suggested that the energy gap of the insulating parent compounds would not exist without the AF order [131].

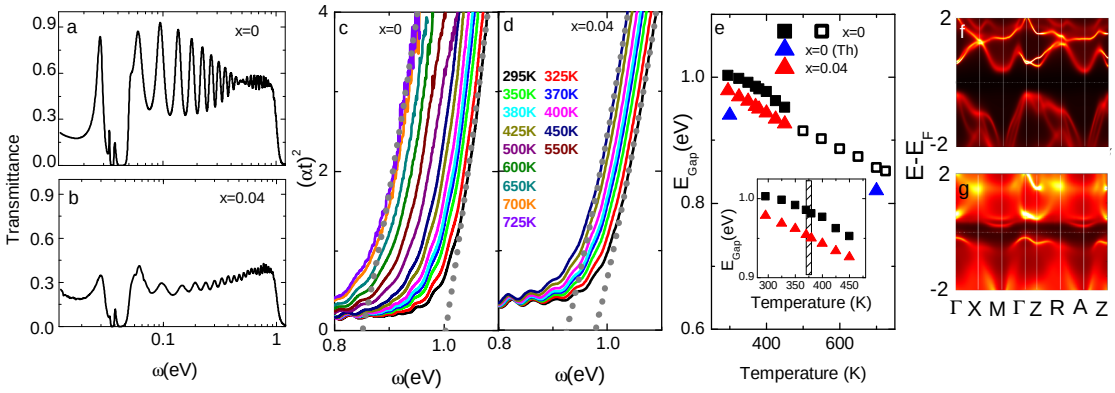

Figure 5.1: High temperature transmittance spectra of $LaMnPO_{1-x}F_x$ for $x = 0.0$ and $x = 0.04$ are plotted in panels (a) and (b), respectively. The corresponding absorption spectra $(\alpha t)^2$ are plotted in (c) for x=0 and (d) for x=0.04. The dashed gray lines plotted on top of the experimental (colored) lines show the linear fit to the $(\alpha t/\omega)^2$ form at the highest and lowest temperatures for each sample. The colored in (d) indicates the measurement temperature of the correspondingly colored spectra for both samples. The x-axis intercept of these linear fits were used to determine the value of the optical gap, E_{Gap}. The value of E_{Gap} extracted from the linear fit is plotted as a function of temperature in (e). We do not observe any anomalies in E_{Gap} upon crossing T_N (shadowed in the inset). The energy gap obtained from transmittance measurements at temperatures greater than 450 K are indicated by the open squares. Band structure calculations are shown for the AF (f) and PM (g) state, revealing a reduced direct energy gap at the Γ point in the PM state. The E_{Gap} values calculated for LaMnPO in the AF and PM states are indicated in (e) by the blue triangles at 300K and 700K, respectively.

5.2.3 High Pressure Measurements

To further explore the role of electron interactions in producing the optical gap, we examined the pressure dependence of the absorption edge in both the undoped and doped LaMnPO samples. In general, the application of pressure increases the electron kinetic energy, and may be expected to reduce the effect of electron correlations [132].

Of additional interest is the tetragonal to orthorhombic structural transition in LaMnPO near 16.2 GPa, and its affect on the electronic structure, which we are able to explore with these high pressure measurements [120]

The high pressure data were obtained using an FTIR spectrometer, coupled to a diamond anvil cell (DAC) in which cryogenically loaded nitrogen was used as the pressure medium [133]. The limited size of the DAC required sample dimensions that were less than $40\times40\times15$ μm^3. Due to limitations imposed by the low energy cut-off of the detector, and the diffraction limit related to the small sample size, energy gap values below 0.12 eV could not be measured. Furthermore, accurate measurement of transmittance was not possible in the region near 0.25 eV, due to absorption in the diamond anvil.

Transmittance spectra near E_{Gap} were obtained at a series of increasing pressures (P). The corresponding $(\alpha t)^2$ spectra are plotted in Fig. 5.2a and 5.2b, for $x = 0.0$ and $x = 0.04$, respectively, where the increase in $(\alpha t)^2$ indicates the onset of interband transitions. The absorption edge is systematically and rapidly suppressed with increasing P. The maximum P, at which a well defined absorption edge is still observable, defined as $P^*_{x=0}$ ($P^*_{x=0.04}$), is 18.8 GPa (15.1 GPa) for the undoped (doped) sample. These pressures are indicated in Fig. 5.2f, 5.2g and 5.2h. At P above P*, the well defined absorption edge is obscured by the appearance of intra-gap absorption features, which will be discussed later in the text. Accordingly, we only extracted a numerical value of E_{Gap} for $P \leq P^*$.

To determine E_{Gap} of the $LaMnPO_{1-x}F_x$ samples under high pressure, we utilized the same method employed for the high temperature data, with linear fits to $(\alpha t/\omega)^2$ indicated by the dashed gray lines in Fig. 5.2a (5.2b) for x=0.0 (x=0.04). The extracted values of E_{Gap} for both undoped and doped samples are plotted as a function of pressure in Fig. 5.2c. For $P < P^*$, the reduction of E_{Gap} obeys an approximately linear relationship with pressure. Assuming this trend continues for $P > P^*$, we performed a linear fit of the lower pressure E_{Gap} values to estimate the pressure at which the gap closes, *i.e.* E_{Gap}=0. These linear fits, indicated for the undoped (doped) sample by the black (red) dotted line in Fig. 5.2a, suggest that gap closure would occur at P=28 GPa (P=25 GPa).

For comparison, DFT+DMFT calculations were carried out for undoped LaMnPO at a series of pressures, with details of the calculations detailed in section 5.4. The

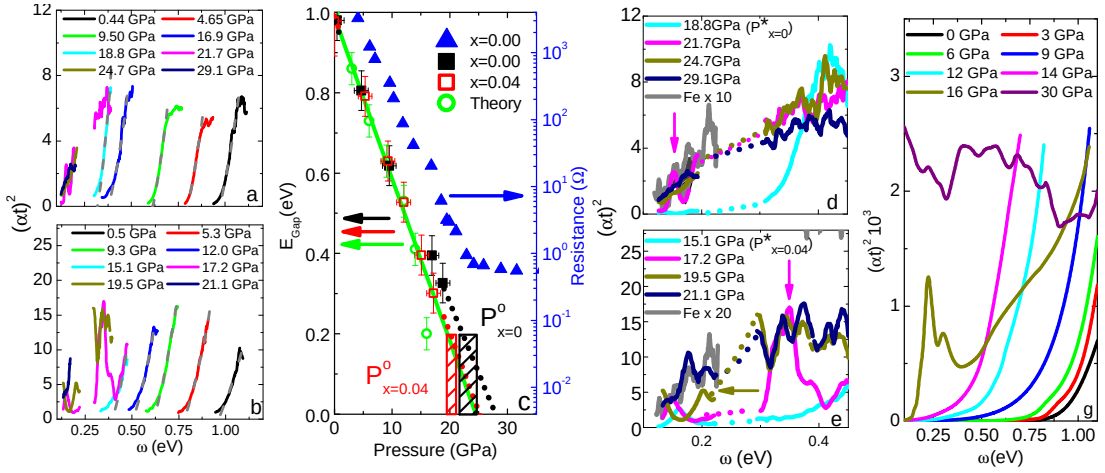

Figure 5.2: Absorption spectra and energy gap extraction of $LaMnPO_{1-x}F_x$ at high pressures. In (a) and (b) we plot the $(\alpha t)^2$ spectra of $LaMnPO_{1-x}F_x$, for x=0.0 and x=0.04 respectively, at a series of increasing pressures. The dashed gray lines indicate the linear fits to $(\alpha t)^2/\omega^2$ which are used to determine the value of E_{Gap}. Above 18.8 GPa in (a), and above 15.1 GPa in (b) peaks appear in the $(\alpha t)^2$ spectra, which are detailed in (f) and (g). In (c) the value of E_{Gap} that we extracted for undoped (doped) LaMnPO are plotted as the black filled squares (red open squares). The black (red) lined rectangles indicate the pressure over which we metallicity emerges in the undoped (doped) sample. Complementary high pressure resistance data for the undoped sample (x=0.00) are plotted in blue, corresponding to the right axis, which was taken from [129]. The green, open circles, indicate the smallest direct energy gap determined from DFT+DMFT electronic structure calculations. The green dotted line shows the linear relationship between the theoretical E_{Gap} and pressure for P$\leq$ 14 GPa. The low ω region of the $(\alpha t)^2$ spectra, of both undoped and doped LaMnPO are highlighted in (f) and (g), where P_x^* is indicated in the legend. In the undoped $(\alpha t)^2$ spectra, where the applied pressure was 21.7 GPa, there appears to be a small peak at 0.15 eV, indicated by the pink arrow. Likewise, in the $(\alpha t)^2$ spectra of the doped sample, there is a pronounced peak at 0.35 eV when P=17.2 GPa (indicated by the pink arrow), and increasing the pressure to 19.5 GPa yields a small peak at 0.19 eV (yellow arrow). The Further application of pressure results in the suppression of these intra-gap features. For further comparison between theory and experiment, in (f) we have plotted the $(\alpha t)^2$ spectra, extracted from DFT+DMFT electronic structure calculations. The 16 GPa and 30 GPa $(\alpha t)^2$ spectra have been scaled by 0.05 and 0.02, respectively, so that they can be seen alongside the lower pressure spectra.

smallest direct energy gap in the calculated band structure is plotted as the green circles in Fig. 5.2c. Below 16.2 GPa, the pressure dependence of the theoretical E_{Gap} is well captured by a linear fit, indicated by the green dotted line in Fig. 5.2c. Increasing the pressure to 16.2 GPa produces a more rapid decrease in E_{Gap}, which deviates from the linear trend found at P$\leq$14 GPa, similar to behavior of the experimentally determined E_{Gap}. Full gap closure is theoretically anticipated to occur by 30 GPa [128], where the corresponding metallic band structure, calculated via DFT+DMFT, is shown in Fig. 5.3c. For direct comparison between the experimental data and theoretical results, the optical conductivity ($\sigma_1(\omega)$) spectra were extracted from the DFT+DMFT calculations. The $\sigma_1(\omega)$ spectra were then converted to $(\alpha t)^2$ (plotted in Fig. 5.2i) via the relationship [82]:

$$\alpha = \frac{4\pi\sigma_1}{n(\omega)c}, \tag{5.2}$$

where a Kramers-Krönig inversion of σ_1 was used to obtain $n(\omega)$, and $t = 5\mu m$. These spectra show a systematic suppression of the absorption edge, similar to the experimentally obtained absorbance spectra shown in Fig. 5.2a and 5.2b. Moreover, absorption peaks in the theoretical $(\alpha t)^2$ spectra appear above the tetragonal to orthorhombic phase transition at 16.2 GPa. These peaks are due to interband transitions at the M-point, which become allowed in the orthorhombic phase as can be seen in Fig. 5.3b, and qualitatively resemble the absorptionfeatures that are experimentally observed, and highlighted in Fig. 5.2d and 5.2e. Also, it is this structural transition that produces the deviation from linearity in the theoretically predicted values of E_{Gap} at 16.2 GPa, described earlier in the text. Interestingly, the intra-gap absorption peaks that indicate the tetragonal to orthorhombic transition in the theoretical absorption spectra at 16.2 GPa, do not appear in our experimental data until pressures greater than 18.8 GPa. We attribute this to differences in the level of uniaxial pressure between the pressure medium used in the x-ray diffraction measurements, and our transmittance measurements. This latter fact, in conjunction with the error bars inherent in high pressure measurements, can account for the difference in the pressures at which the intra-gap peaks emerge.

As stated earlier in the text, the band edge at high pressures is obscured by the intra-gap absorption peaks, which make it difficult to precisely determine the pressure at which the gap collapses. One method to estimate the pressure where the energy gap is

fully closed is to compare our measured absorption spectra, to that obtained for a known metallic sample. Accordingly, we measured the absorbance of an iron (Fe) flake in the same experimental setup used for the high pressure measurements. The absorbance spectra of Fe is plotted alongside the high pressure absorbance spectra of LaMnPO in Fig. 5.2d and 5.2e as the gray solid line. The Fe sample that we used was smaller than either the undoped or doped LaMnPO sample. Thus, it's absorption was notably smaller at low ω due to diffraction of light around the small sample. Regardless, the absorbance of Fe is plotted alongside that of undoped (doped) LaMnPO in Fig. 5.2d and 5.2e, multiplied by an arbitrary factor to make direct comparison the spectra easier. Notably, the Fe absorbance spectrum at low ω linearly increases with ω, as expected when the wavelength of the incident light shifts away from the diffraction limit. Besides this increase, there is no significant feature in the $(\alpha t)^2$ spectra of Fe sample, as would be expected for a metallic, and opaque, material. Accordingly, we consider the $LaMnPO_{1-x}F_x$ sample to be opaque, and E_{Gap}=0, when its lineshape resembles that of the Fe flake, and the spectral features are suppressed. Using this criterion, we conclude that the pressure at which undoped LaMnPO becomes opaque ($P^o_{x=0.00}$) is above 21.7 GPa, where the spectral feature is still visible, but below 24.7 GPa. Likewise, the pressure of opacity for $LaMnPO_{0.96}F_{0.04}$ ($P^o_{x=0.04}$) lies between 19.5 GPa and 21.1 GPa. The decrease in P^o with doping suggests that higher dopings could reduce P^o further, and more highly doped $LaMnPO_{1-x}F_x$ samples could be metallized with relatively small pressures.

Complementary high pressure resistance (R) measurements of LaMnPO were carried out, and reported in [129]. They found that R of undoped LaMnPO is reduced with increasing pressure, until it saturates at pressures above 20 GPa, consistent with the pressure at which we identify E_{Gap}=0. The measured R values are plotted alongside our experimentally determined E_{Gap} in Fig. 5.2c. Generally, opacity at low energies arises from free carriers. Thus the observation of opacity, the saturation in resistance at pressures above 20 GPa, and the systematic reduction in E_{Gap} at lower pressures all suggest a metallic state has been induced via collapse of the band gap.

5.2.4 On the Nature of the High Pressure Metallic State

The calculated band structure is plotted in Fig. 5.3a,b, and c for pressures of 1 bar, 16 GPa, and 30 GPa. At 1 bar, the smallest direct energy gap is at the Γ point, and is 1.0 eV. At 16 GPa, the direct band gap at the Γ point is reduced in energy. However, LaMnPO also undergoes a tetragonal to orthorhombic structural transition which allows interband transitions at the *M* point, which are smaller in energy than those at the Γ point. These newly allowed interband transitions at the *M* point produce the intra-gap features observed in the absorption spectra, and highlighted in Fig. 5.2d and 5.2e. Increasing the pressure to 30GPa results in a fully closed gap, with many bands cross the Fermi energy, yielding a metallic system.

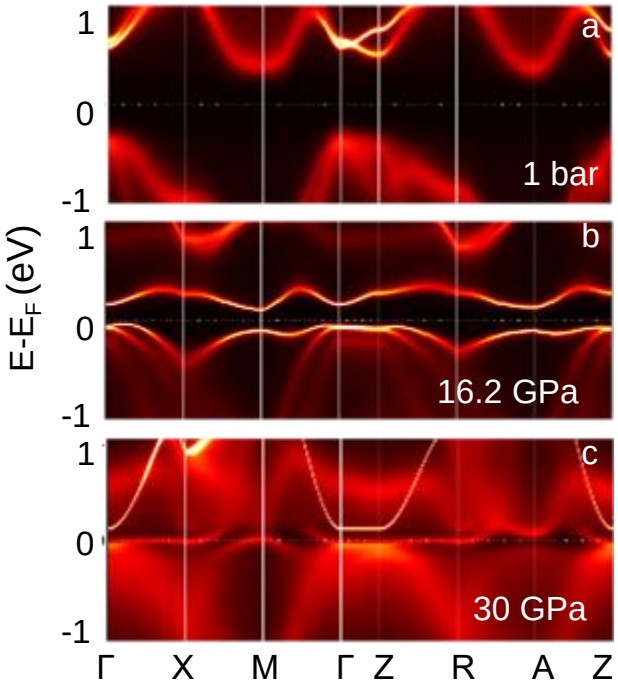

Figure 5.3: The band structure of LaMnPO at 1 bar (a), 16.2 GPa (b) and 30 GPa (c), calculated using DFT+DMFT

Further insight into the correlations in this system can be revealed by examining the partial density of states (PDOS) calculated when correlations are both neglected, and when they are included. Thus, in Fig. 5.4a, 5.4b, and 5.4c, we show the PDOS calculated using DFT. At 1 bar (Fig. 5.4a), the system is strongly metallic, with all or-

bitals possessing a non-zero PDOS at E_F (Energy=0). Increasing the pressure to 16.2 GPa (Fig. 5.4b) reduces the PDOS of most orbitals in the vicinity of E_F, with the exception of the xz and yz orbitals, which develop a sharp peak just below E_F. By 30 GPa (Fig. 5.4c), the PDOS is suppressed for all orbitals, most notably the x^2-y^2 and xy orbitals, which in fact become gapped. The PDOS calculated via DFT+DMFT reveals a significantly different trend. At 1 bar (Fig. 5.4d), DFT+DMFT predicts the PDOS of all orbitals is zero at E_F yielding an insulating system, as verified by experiments in the main text, and in Refs. [120, 121]. The calculation at 16.2 GPa (Fig. 5.4e) indicates that most of the orbitals in LaMnPO develop a significant peak in the PDOS immediately below, and at approximately 0.1 eV above E_F. However, the electron correlations, though reduced by pressure, are still strong enough to sustain the energy gap. Finally, at 30 GPa (Fig. 5.4f), DFT+DMFT finds that the system is highly metallic, where all but the xy orbital has a non-zero PDOS at E_F.

It is particularly interesting to compare the PDOS obtained from DFT at 30 GPa, to the complementary DFT+DMFT PDOS at the same pressure. At this pressure, these two methods of calculation seem to produce qualitatively similar PDOS spectra for all orbitals. Typically, when DFT produces similar results to calculations where correlations are included, it indicates that the effect of the correlations on the electronic system have been largely reduced. However, the electronic bandwidth, corresponding to the width of the peak in PDOS near Energy = 0.0 eV, is still smaller in the DFT+DMFT calculations than those obtained from DFT, indicating correlations are still present. In the case of LaMnPO, this would mean that increasing the pressure from 16.2 GPa, to 30 GPa, tunes the system from a Mott-Hund's insulator to a correlated metal. The intermediate region between these two pressures warrants further study, as moderate correlations often herald a complex and exciting phase diagram, the most salient examples of this being the cuprates and Fe-pnictides [54, 134, 135]. However, this region remains largely unexplored, and the transmission is effectively zero in the metallic state, thus no useful data on the free carrier dynamics can be obtained using the spectroscopic transmission techniques utilized in this work. Future studies, both theoretical and experimental, are required to ascertain the landscape of this moderately correlated region of the phase diagram. One very likely outcome would be the revelation of an orbitally

selective Mott transition, which can be expected when Mott-Hubbard interaction and Hund's coupling are both present, and substantial crystal field splitting differentiates the Mn 3d orbitals, as in this class of material [134, 136–138].

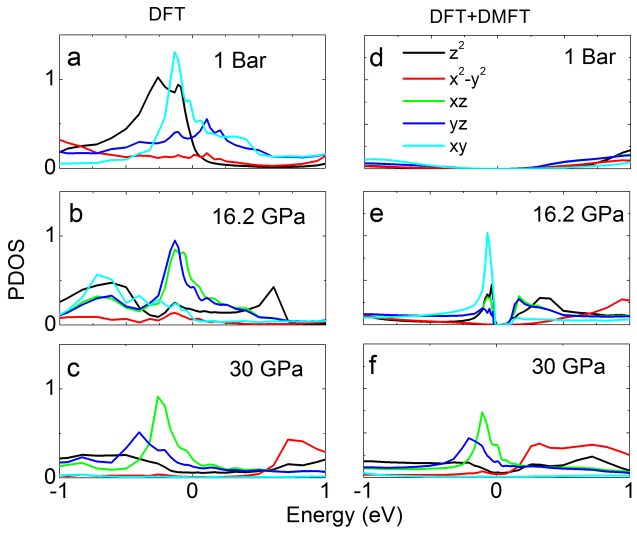

Figure 5.4: The PDOS in LaMnPO is calculated using DFT at 1 bar (a) 16.2 GPa (b) and 30 GPa (c). Likewise, the PDOS extracted from DFT+DMFT at 1 bar (d), 16 GPa (e) and 30 GPa (f) is also shown

5.3 Conclusion

Our data reveal that by applying pressure to LaMnPO, we are able to induce a bulk metallic state, which is not directly caused by the elimination of AF order, or the structural transition. Furthermore, our results can be consistently described using DFT+DMFT, assuming the presence of AF ordering, a Mott-Hubbard U and Hund's rule J_H. The coexistence of these correlations suggest this system resembles the Fe-pnictides, albeit with an insulating ground state. These results also imply that the insulator-metal phase transition is shifted to lower pressures with F-doping. Our findings identify $LaMnPO_{1-x}F_x$ as an exciting playground in which the parameters of pressure and doping may be tuned to reveal a complex phase diagram, as is often found in strongly correlated systems.

Table 5.1: Crystal parameters used in the electronic structure calculations

P (GPa)	Space group	a ()	b ()	c ()	z_{La}	z_P
0	P4/nmm (#129)	4.05786	4.05786	8.84341	0.13879	0.6569
3	P4/nmm (#129)	4.0350	4.0350	8.712	0.1415	0.6526
6	P4/nmm (#129)	4.0122	4.0122	8.581	0.1443	0.6512
9	P4/nmm (#129)	3.9945	3.9945	8.451	0.1425	0.6428
12	P4/nmm (#129)	3.9768	3.9768	8.322	0.1407	0.6345
14	P4/nmm (#129)	3.95344	3.95344	8.34822	0.1416	0.6260
16	Cmma (#67)	5.5937	5.6664	8.169	0.1485	0.612
30	Cmma (#67)	5.20408	5.37473	7.42454	0.1091	0.5676

5.4 Appendix A: Theoretical Calculations

Density functional theory (DFT) band structure calculations were done using the full-potential linear augmented plane wave method implemented in [139] in conjunction with a generalized gradient approximation [140] of the exchange correlation functional. To take into account strong correlation effect, we further carried out first-principles calculations using DFT+DMFT [141] which was implemented on top of WIEN2K and documented in Ref. [142]. In the DFT+DMFT calculations, the electronic charge was computed self-consistently on DFT+DMFT density matrix. The quantum impurity problem was solved by the continuous time quantum Monte Carlo method [143, 144], using Slater form of the Coulomb repulsion in its fully rotational invariant form. We used a Hubbard U=8.0 eV and Hund's rule coupling J=0.9 eV for all the DFT+DMFT calculations at all pressures, consistent with previous publication [127]. The Hamiltonian used for these calculations is:

$$\hat{H} = \sum_i (-\mu \hat{N}_i + \hat{H}_{int}[\hat{d}^\dagger_{i\nu}]) + \sum_{\langle ij\rangle \nu} t \hat{d}^\dagger_{i\nu} \hat{d}_{j\nu},$$

$$\hat{H}_{int}[\hat{d}^\dagger_{i\nu}] = \frac{3}{4} J \hat{N}_i + \frac{1}{2}\left(U - \frac{1}{2}J\right)\hat{N}_i(\hat{N}_i - 1) - J\hat{\mathbf{S}}_i^2.$$

In this Hamiltonian, $d^\dagger_{i\nu}$ is the creation operator on site i for an electron of type ν, where $\nu = (m\sigma)$, with σ and m indicating the electron spin and orbital, respectively[145]. Further details on the Hamiltonian and the theoretical methods can be found in [145]

We used the experimentally determined lattice structures [128], including the internal positions of the atoms as shown in Table 5.1

5.5 Appendix B: Alternative Determination of E_{Gap}

If one has access to the complex dielectric constant ($\hat{\varepsilon} = \varepsilon_1 + i\varepsilon_2$), the magnitude of E_{Gap} can be precisely determined from the x-axis intercept of a linear fit to $(\varepsilon_2)^2$ [55]. Accordingly, we measured the transmittance spectra over a broad range (100 cm^{-1} to 12,000 cm^{-1}) during some of the high temperature measurements, and modelled these spectra to obtain $\hat{\varepsilon}$. Moreover, by simultaneously fitting the periodicity of the interference fringes, along with the transmittance amplitude, we accurately determined the thickness of these crystals to be 5 $(\pm 0.3)\mu m$. An example transmittance spectra, obtained at 295K, is shown in the inset to Fig. 5.5a (black line), along with the corresponding model (gray line). The resulting $(\varepsilon_2)^2$ spectra, which were obtained at temperatures from 295K to 450K, are plotted in Fig. S2a (colored lines), along with the linear extrapolation at each temperature (gray lines). The values of E_{Gap} corresponding to this alternative analysis are plotted in Fig. 5.5b (filled black squares), along with the values of E_{Gap} obtained from the $(\alpha t/\omega)^2$ analysis (open black squares), described in the main text [55]. An inspection of Fig. 5.5a, reveals that the $(\alpha t/\omega)^2$ analysis tends to underestimate the value of E_{Gap} by approximately 300 cm^{-1}, and thus establishes the size of the error bars. Importantly, this difference is small when compared to the magnitude of the E_{Gap}. In addition, the $(\alpha t/\omega)^2$ analysis captures the overall behavior of E_{Gap}. Both of these latter facts confirm the validity of this method for extracting E_{Gap}, and analyzing trends, particularly when one lacks the full ε_2 spectra.

5.6 Acknowledgements

Chapter 5 is a reprint of material published in *Physical Review B* **94**, 045115 (2016). K.W. Post, Alexander F. Goncharov, Z.P. Yin, J.W. Simonson, Jing Guo, Liling Sun, S. Zellman, M.D. Goldflam, H.T. Stinson, B.C. Chapler, D.E. McNally, Zhongxian Zhao, G. Kotliar, M.C. Aronson, and D.N. Basov. The dissertation author was the primary researcher and author of this material.

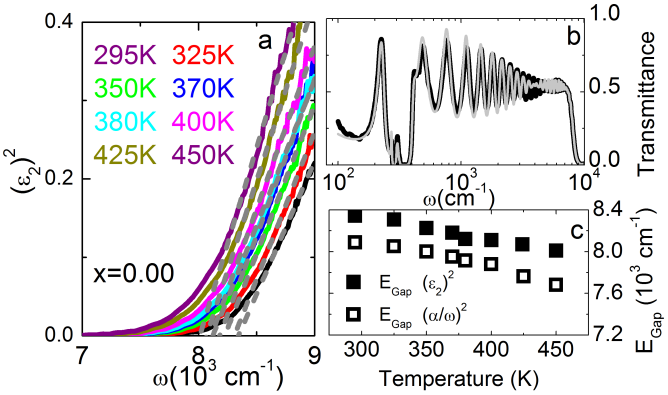

Figure 5.5: Energy gap extraction from $(\varepsilon_2)^2$. (a) The $(\varepsilon_2)^2$ spectra, obtained for undoped LaMnPO at a series of temperatures. The linear fits, which were used to determine E_{Gap} are indicated by the gray lines. (b) An example broadband transmittance spectra at 295K (black line), and the corresponding model fit (gray line) are shown. (c) The energy gap extracted using the linear fit to $(\varepsilon_2)^2$ is plotted vs temperature (filled black squares), along with E_{Gap} obtained from the $(\alpha t/\omega)^2$ analysis (open black squares).

Chapter 6

Coexisting first and second order electronic phase transitions in $NdNiO_3$

Abstract

Understanding phase transitions is a cornerstone of contemporary physics. A landmark insight of Landau was that the Free energy (F) of a system could be described with the addition of an order parameter (Φ). This framework yielded a global classification of phase transitions into first and second order, where the latter corresponds to a continuous evolution of Φ away from zero, whereas in the former, evolves discontinuously. Here we show that the temperature-driven insulator-to-metal transition (IMT) in the prototypical correlated electron system NdNiO3 defies this established classification. By harnessing a nano-scale optical probe of the local electronic conductivity, we observed two physically distinct, yet concurrent phase transitions in different regions of epitaxial films. In the bulk of the material, we observe a discrete, first order phase transition between the paramagnetic metal and the antiferromagnetic (AF) insulator. Additionally, in the AF state we visualized nanoscale domain walls that undergo a continuous IMT with hallmarks of the second order transitions, distinct from the behavior in the rest of our specimens. We examined possible microscopic origins of this unprecedented coexistance using a free energy model consisting of interacting charge and spin orders, which accurately describes both phase transitions, and supports the notion that

AF order drives the first order transition.

6.1 Introduction

The study of correlated electron systems, and the cooperating or competing degrees of freedom that produce phase transitions is an area at the forefront of condensed matter physics[11, 20]. The rare earth nickelates (RNiO$_3$) are a system that exemplifies the complexity of phase transitions, where structural, electronic, and magnetic degrees of freedom all contribute to the insulator to metal phase transition IMT[146, 147]. Recently, the importance of both charge ordering (CO) and the Mott interactions within this system have been uncovered [21, 22, 148, 149], although it has also been proposed that antiferromagnetic ordering drives the first order IMT for certain R [24]. Thus far, investigations into the IMT of RNiO$_3$ have primarily been bulk sensitive, where the modified interplay of the charge and magnetic order parameters, arising from local variations, is masked by the bulk response. Clarification of the intrinsic behavior of the IMT requires probing the electronic structure across the IMT at the relevant, nanometer length scale. Accordingly, we measured the near-field response of NdNiO$_3$ film on an NdGaO$_3$ substrate (NNO/NGO) across the IMT with nanometer resolution using a cryogenically enabled scattering-type scanning near-field optical microscope (s-SNOM), detailed in Ref. [29]. In these measurements, we have found that the bulk IMT is archetypically first order, in that NNO transitions directly between insulating and metallic end phases without accessing any intermediate phases. Additionally, we observed metallic domain walls (DW) in a temperature range proximal to the IMT, which possessed a near-field response that evolves continuously from insulating to metallic. We consistently attribute these DW to the boundary beween different AF domains, where suppressed AF order yields a 2nd order IMT within in an antiferromagnetic insulating matrix. Here, we leverage the observation of these two phase transitions to show the primacy of AF order in the IMT of NdNiO$_3$. These results also highlight the importance of high spatial resolution for unveiling the fundamental character of phase transitions.

6.2 Results

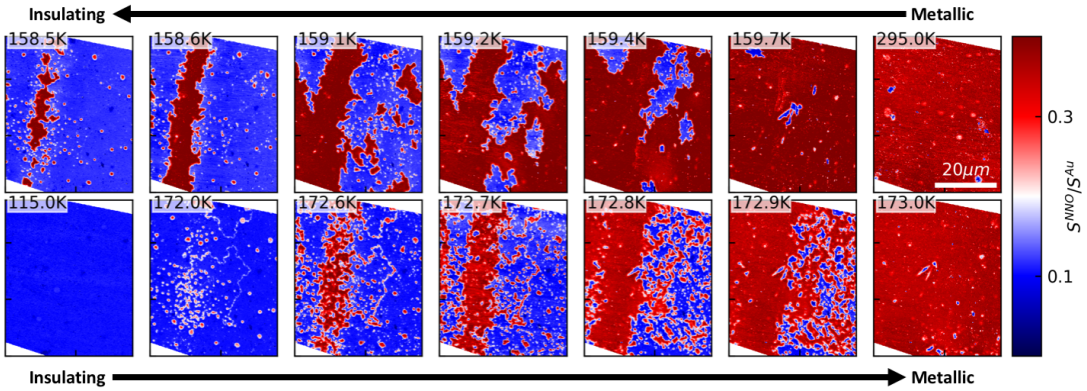

Figure 6.1: Images acquired while cooling (warming) through the IMT are shown in the top (bottom) row. The 100K and 295K images were acquired in a different location than the rest of the images.

Fig. 6.1 presents large area SNOM images that were acquired at 295K, upon cooling through the transition and down to 115K, as well as those acquired while warming through the IMT. The sharpness of the IMT, as evident from $\rho(T)$, necessitated a unique method for acquiring the images of coexisting phases, detailed in [SI]. Several features are evident from these images. First, at high temperatures (295K) the sample is almost entirely metallic and uniform within the FOV. However, within this image there are small puddles with a near field response slightly reduced from the bulk metallic state, which are discussed later in the text. Upon cooling to 159. 7 K, insulating domains appear both in the middle of the FOV, and the upper left corner. After cooling to 159.4 K, the insulating domains expand from the initial insulating puddles. The apparent expansion of the insulating domains continues to 158.7 K leaving a persistent metallic ribbon within the image, which eventually disappears at 158.4 K, although many small metallic puddles are still visible. Some of these are visible, albeit with reduced signal, down to 115 K [SI]. Upon warming from the lowest temperature to 172.0 K, metallic signal is first observed in the puddles that were evident in the cooling image acquired at 158.4 K. Metallic domains expand from these puddles at 172.6 K, eventually coalescing into a continuous ribbon at 172.7 K, like that observed on cooling. Possible origins for these puddles, and their relationship to the ribbon are discussed in [SI]. During the

warming sequence, two DW appeared within the FOV at 172.0K, which became more pronounced at 172.6K and 172.7K. Concurrently, additional metallic domains continue to appear and expand at 172.7K, 172.8K and 172.9K until the $NdNiO_3$ sample is metallic within the FOV at 173.0K. During the phase transition, there was no structure or patterning of the insulating/metallic domains that would indicate a broken symmetry arising from, for instance, strain in the underlying lattice. In contrast, previous measurements of vanadates associated stripe-like metallic and insulating domains with an IMT that was closely related to long range strain interactions arising at the filmâĂŞsubstrate interface[29, 150, 151]. Accordingly, long-range strain interactions amidst the IMT in $NdNiO_3$ are likely unimportant compared to short-range interactions in governing the morphology of emergent domain patterns in these $NdNiO_3$ films.

For quantitative analysis of near field optical response (S), a series of images through the IMT were acquired with an Au reference in the field of view. Using the Au as a reference, the near field response of the NNO (S^{NNO}) could be normalized, line-by-line, to that of gold (S^{NNO}/S^{Au}). In the inset to Figs. 6.2a and 6.2b, Au-normalized images with an approximately 50% insulating âĂŞ 50% metallic (50/50) pf are shown, which were acquired on the cooling and warming IMT, respectively. The entire sequence of images, shown in [SI], from which these two were selected, confirmed the gross trends associated with the images shown in Fig. 6.1c. To elucidate the evolution of the near field signal, histograms of Au-normalized SNOM image are plotted at three temperatures corresponding to primarily insulating, 50/50, and metallic phases, from both the cooling (Fig. 6.2a) and warming (Fig. 6.2b) transitions, with the complete set of histograms shown in [SI]. These histograms count the number of pixels in the image with a given range of S^{NNO}/S^{Au}, and serve as a useful visualization of how the near field response evolves across the IMT. It is immediately obvious that S^{NNO}/S^{Au} on both the cooling and warming IMT are centered in two distinct peaks. We determined the mean signal associated with both the insulating ($\overline{S^{Ins}}$) and metallic ($\overline{S^{Met}}$) peaks from the two minima in the second derivative of the histograms. During the cooling transition, the value of $\overline{S^{Ins}}$ and $\overline{S^{Met}}$ are centered at 0.12 and 0.4, respectively. On warming, $\overline{S^{Ins}}$ is centered at 0.11, similar to the value found on cooling. However, $\overline{S^{Met}}$ is at a slightly lower value of 0.35. Importantly, even at temperatures where there is significant coex-

istence of metallic and insulating phases, there are very few pixels with a signal that resides at values between the two primary peaks. Accordingly, we identify the IMT in NdNiO3 as a binary transition, where the bulk of the sample does not access any states intermediate between the insulating and metallic end states, but rather, switches discretely between them. The binary nature of the transition suggests that the domain formation may be interpreted using the framework of critical endpoints in an Ising model, where a ferromagnetic, nearest neighbor interaction accounts for the tendency of neighboring domains to take the same ordering [152, 153]. Within this framework, there are critical points that give rise to universal, power-law scaling behavior. Accordingly, we have extracted two relevant parameters, the radius of gyration (R_v) and domain size (s), from all the domains within a given image (inset to Fig. 6.2c). Plotting the logarithm of these two quantities reveals power-law scaling, extending across four decades; perhaps the largest range of critical scaling measured in any correlated oxide and strongly indicative of universal first order phase transition behavior, with an essential contribution from electron interactions[152–154].

The binary transition observed in the bulk of the film is strongly contrasted by the behavior observed in the DWs. Before describing this behavior in more detail, it is important to note that the DWs were not pinned to defects, or any topographic features, since they appeared in different positions after repeated thermal cycling, as made apparent from the comparison of Fig. 6.3a with 6.3, which were acquired within the same FOV. However, within a single thermal cycle, the DW remained fixed. Furthermore, these DWs appeared only appeared while warming through the IMT. To elucidate the electronic character associated with these DW, line profiles of a DW within the Au normalized images were extracted at a series of temperatures, with the average line profiles shown in Fig. 6.3c. From these profiles, it is immediately obvious that the signal along the DWs continuously increases from ≈ 0.14 to ≈ 0.35, as temperature increases, in contrast to the discrete behavior observed in the bulk of the sample. For comparison, we acquired the average line profile at the boundary between insulating and metallic domains (IMDW) for temperatures between 171.6K, and 172.4K. The variation of the IMDW line profile within this temperature window is indicated by the gray line in Fig. 6.3c. These line profiles were fit with a $\tanh(x/\zeta)$ lineshape, where $\zeta = 300nm$ captures

the width of the boundary. Notably, over the same temperature range where the DW showed significant evolution, little change is observed in the IMDW. This latter point is affirmed by comparing the mean signal along the DW ($\overline{S^{DW}}$), to the $\overline{S^{Ins}}$ and $\overline{S^{Met}}$, as in Fig. 3g, where continuous evolution of $\overline{S^{DW}}$ is evident, and in sharp contrast to the remarkably constant metallic and insulating signal in the bulk of the material. The continuous variation of near field signal along the DW is a hallmark of second order phase transitions, whereas first order phase transitions show discrete behavior, such as the jump between $\overline{S^{Ins}}$ and $\overline{S^{Met}}$ observed in the bulk of the material.

To understand the origin of these DW, it is import to keep in mind the close relationship between the IMT, charge and AF order within the $R\mathrm{NiO_3}$ system. The IMT is thought to arise from charge order which is associated with orthorhombic to monoclinic transition, and a bond disproportionation in the Ni-O octahedra, with the propation vector (in pseudocubic notation): $\vec{k_{CO}} = (\frac{1}{2}, \frac{1}{2}, \frac{1}{2})$ [149]. The AF also orders along the $[111]$ direction, however, it is unit cell quadrupling, with the momentum vector given by $\vec{k_{AF}} = (\frac{1}{4}, \frac{1}{4}, \frac{1}{4})$. In the generic $R\mathrm{NiO_3}$ phase diagram, the IMT is first order when AF and CO occur simultaneously, but second order when they emerge seperately [146]. In the case of our $\mathrm{NdNiO_3}$ sample, RXS measurements of this sample showed hysteresis in the peak intensity associated with bulk AF order, resistivity **[SI]**, indicating that both IMT and AF transitions are first order. It is possible to switch from a first to second order transition by changing the rare-earth cation, or alternatively the O $2p$-Ni $3d$ orbital overlap. To clarify the interplay between AF and CO, we considered the Landau free energy description of this system in local order parameters related to AF (ψ_{AF}) and charge (ϕ_{CO}), as well as their mutual coupling [24]:

$$F(\psi_{AF}, \phi_{CO}) = r \cdot \frac{\tilde{T} - T_N}{T_N} \cdot \psi_{AF}^2 + \psi_{AF}^4 - \lambda \cdot \psi_{AF}^2 \cdot \phi_{CO} + \tilde{r} \cdot \frac{\tilde{T} - T_{CO}}{T_{CO}} \cdot \phi_{CO}^2 + \phi_{CO}^4 + \frac{\tilde{\zeta}^2}{6}(\nabla \phi_{CO})^2 + \frac{\zeta^2}{6}(\nabla \psi_{AF})^2. \quad (6.1)$$

In this equation r parametrizes the energy of AF order, T_N indicates the AF ordering temperature, and ζ corresponds to the energy cost associated with changes in AF ordering, such as at the boundary between different domains. Likewise, $\tilde{r}$, T_{CO}, and $\tilde{\zeta}$ are associated with the energy of CO, the temperature of CO, and the energy cost as-

sociated with changing CO, respectively. Importantly, coupling between the two order parameters (ϕ_{CO} and ψ_{AF}) is governed by the coefficient λ, which is symmetry allowed in systems where $\vec{k_{CO}} = 2 \cdot \vec{k_{AF}}$, as in $R\mathrm{NiO_3}$, yielding a cubic term in the free energy expansion[155]. Thus, a finite λ dictates that AF order necessarily induces a local minimum in free energy at ϕ_{CO} through a first order phase transition [24]. Alternatively, if $T_{CO} > T_N$, CO emerges in the absence of AF through a second order phase transition; a situation that is physically realized in the $R\mathrm{NiO_3}$ materials where the rare-earth ion is smaller than Nd. Frustration or modification of magnetic order is naturally expected at the boundary between domains of different AF propagation, in the form of domain walls [156], where the $\vec{k_{CO}} = 2 \cdot \vec{k_{AF}}$ condition may be broken. In this latter case, CO may emerge through a second order phase transition. We have explored this possibility by minimizing the free energy expansion of this system (Eqn. 6.1) with respect to $\psi_{AF}(x)$ and $\phi_{CO}(x)$, assuming that ψ_{AF} goes to zero at $x = 0$. The temperature dependence along the boundary was captured by considering a range of $\tilde{T}$, where $r = \tilde{r} = 8$, $T_{CO} = T_N = 170K$, and $\zeta = \tilde{\zeta} = 300nm$, where ζ was extracted from the IMDW profiles. Since $\phi_{CO} = 0$ is associated with the metallic state, where S is maximized, we can infer an inverse relationship between ϕ_{CO} and S. Thus, for qualitative comparison, we considered $1 - \phi_{CO}$, which may be expected to show trends similar to the near field response. The lineshapes of $1 - \phi_{CO}$, resulting from the minimization of free energy across the boundary between AF domains, are plotted in Fig. 6.3d. At $x = 0$, $\psi_{AF} = 0$, and there is a concurrent enhancement of $1 - \phi_{CO}$, which becomes larger and wider as $\tilde{T}$ increases, in close agreement with the experimentally acquired line profiles of Fig. 6.3c. Consistently, in the absence of DW, solving Eqn. 6.1 when T_N is sufficiently smaller than T_{CO} yields a continuous evolution of ϕ_{CO} away from zero,whereas setting $T_N = T_{CO}$ produces discontinuities in ϕ_{CO}.

Thus, a likely explanation for these DW is that they arise at boundaries between AF domains, where AF ordering is suppressed, yielding a second order IMT, manifesting as a continuous variation in the observable SNOM signal. Additionally, since second order transitions are not hysteretic, the temperature at which this phase transition occurs would not be expected to be different upon warming and cooling cycles. Therefore, the absence of these channels on cooling can be explained by the fact that the bulk of the

material is PM and metallic, and there are no regions of frustrated AF at the temperature associated with the emergence of the DW ($\approx 173K$). Accordingly, these DW can be ascribed to regions of frustrated AF order arising at the boundary between two distinct AF domains. These results confirm the primacy of AF ordering in the IMT of $NdNiO_3$, and it's stabilization of the charge ordered insulating state described in Ref. [24].

Recently, numerous studies have explored the exotic phases that emerge when broken symmetry is imposed by the interface of two different materials [157–160]. However, this work, in addition recent to reports, have shown that the broken symmetry within a material is a similarly fertile arena for the observation of exotic phases [161, 162]. For instance, mobile domain walls observed in the pyrochlore iridates, which were also associated boundaries between AF domains [161], and are likely topological in origin [163, 164]. Here we have shown that the complex interplay of charge and AF ordering in $NdNiO_3$ induces a novel DW confined, second order, temperature driven IMT, coexisting with the bulk phase transition. Possibly, similar phases may be a common feature within correlated oxides, where there are often numerous active degrees of freedom related to the phase transion. Notably, complimentary nanoscale probes of $NdNiO_3$ samples found that the IMT morphology was dictated by topographic features [165], which likely masked the emergent DW. Here, the observed scaling behavior associated with the insulating and metallic domains indicates that we are probing fundamental physics of the phase transition within $NdNiO_3$.

6.3 Conclusions

The SNOM images acquired in this study have identified that the IMT in $NdNiO_3$ is ideally first-order. Additionally, within the near field images, we identified the emergence of DW, associated with boundaries between AF domains. These DW undergo a host 2nd order IMT, which coexists with the 1st order transition to the metallic phase of $NdNiO_3$. The accurate description of this coexistence with Landau free energy analysis implies the importance of AF order in this IMT. By itself, the IMT bound to a domain wall is a novel finding within the broad field of insulator to metal transitions. However, this is perhaps the first observation of simultaneously occurring first and second order

phase transitions within the same material; an observation which should motivate future theoretical investigations into phase transitions. Importantly, the macroscopic measurements of both the AC and DC conductivity for this material, which are representative of those for correlated oxides in general, masked the exotic behavior revealed in this work. Thus, these results show the necessity of microscopic information for clarifying electronic behavior, in the broader class of correlated oxides, especially amidst phase transitions.

Materials and Methods

A schematic of the nano-optical imaging setup is shown in Fig. 6.4a. Focused infrared light is incident upon, and scattered from the metallic tip of an atomic force microscope (AFM) probe, oscillating at frequency , near the sample surface. The back-scattered radiation from the probe encodes information about the complex optical constants of a sample at the frequency of the laser source . In the first approximation, the detected amplitude of back-scattered radiation modulated at high harmonics (n$\geq$2) of the cantilever oscillation frequency provides a measure of the local âĂIJnear-fieldâĂİ optical response of the sample and, by implication, its optical conductivity resolved at the 20-nm scale [29]. Throughout this work, we utilized this nano-scale optical probe to evaluate the low energy ($\omega = 900cm^{-1}$) optical response associated with free carriers (Drude conductivity) in the metallic state of the NNO film, or the bulk energy gap of the insulating state. The ex-situ resistivity across the IMT is plotted in Fig. 6.4b, where the sharpness of these curves attests to the quality of these epitaxial samples.

6.4 Acknowledgements

Chapter 6 is a reprint of material in preparation for publication. K.W. Post, A.S. McLeod, M. Hepting, M. Blushke, Yifan Wang, G. Cristiani, G. Logvenov, A. Charnukha, A. Pasupathy, A.V. Boris, E. Benckiser, K.A. Dahmen, E.W. Carlson, B. Keimer, and D.N. Basov. The dissertation author was the primary researcher and author of this material.

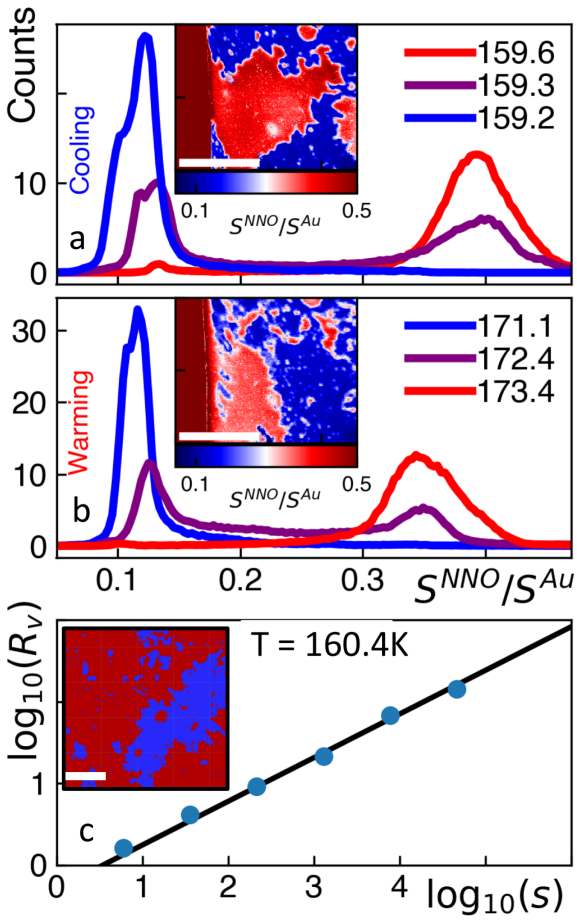

Figure 6.2: Histogram analysis of Au-normalized near field images. (a), (b) Near field images were acquired with an Au strip in the field of view on cooling (warming), with example images shown in insets. Histograms of these Au normalized images at a subset of temperatures on cooling and warming are plotted in (a) and (b), respectively. The logarithmically binned radius of gyration is plotted against the domain size in (c), revealing critical scaling, with a linear fit indicated by the black line. The inset shows the binarized image from which the scaling was extracted. In all images, the scale bar indicates $10\mu m$

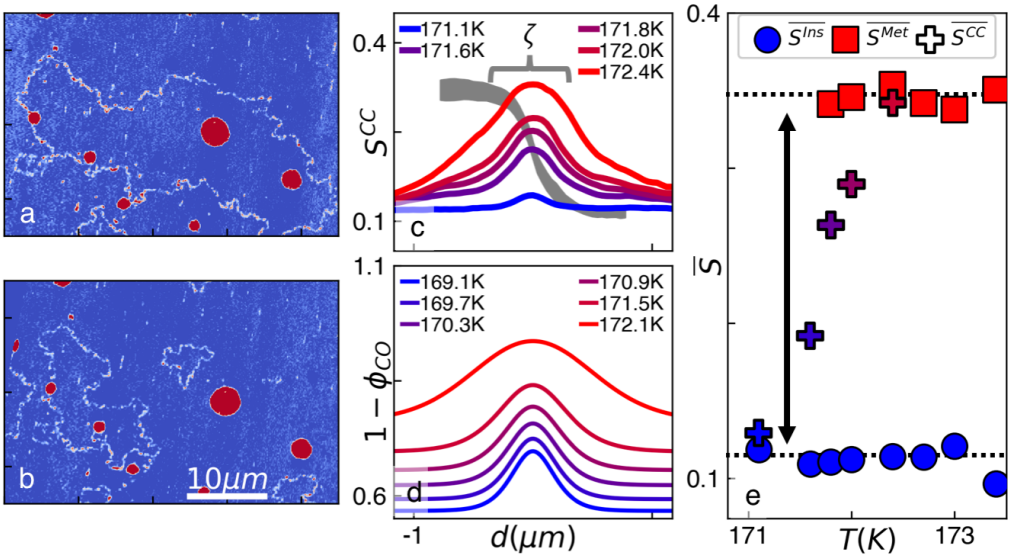

Figure 6.3: Analysis of the domain walls observed within the near field images. Panels (a) and (b) show large area images of NNO in the same spatial location, but during different thermal cycles at T=173.1K. The domain walls (DW) manifest within these images as the lines of enhanced contrast. Panel c: the average line profile along a DW was extracted at a series of increasing temperatures. The gray line indicates the range of signal values acquired from average profiles along the boundary between insulating and metallic domains. Panels (d): the form of charge ordering amplitude $(1-\phi)$ that minimizes the free energy F across a boundary between domains with different AF orderings is plotted at a series of increasing values of temperature $\tilde{T}$. Panel e: the average signal value corresponding to the insulating (blue), and metallic (red) domains from the entire FOV are plotted as a function of temperature along with the average value of the signal along the DW acquired from the same images. The crosses in (e) are colored to match their corresponding average line profile in (c). The black arrow indicates the range of signal values that separate the average insulating and metallic signals in bulk NNO.

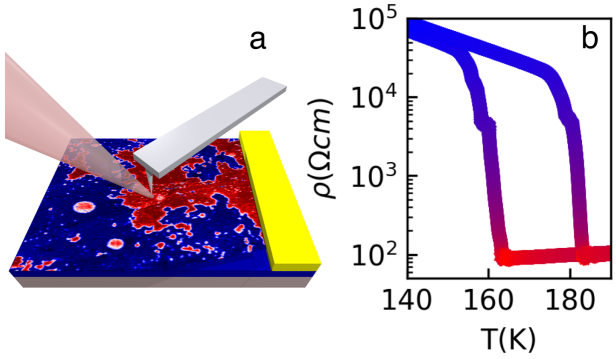

Figure 6.4: A schematic of the near field setup is shown in (a). In (b) the temperature dependence of the resistivity is plotted as a function of temperature across the IMT.

Bibliography

1. Niu, Q., Thouless, D. J. & Wu, Y.-S. Quantized Hall conductance as a topological invariant. *Physical Review B* **31,** 3372–3377 (Mar. 1985).

2. Hasan, M. Z. & Kane, C. L. Colloquium. *Reviews of Modern Physics* **82,** 3045–3067 (Nov. 2010).

3. Moore, J. E. The birth of topological insulators. en. *Nature* **464,** 194–198. ISSN: 0028-0836 (Mar. 2010).

4. Haldane, F. D. M. Model for a Quantum Hall Effect without Landau Levels: Condensed-Matter Realization of the "Parity Anomaly". *Physical Review Letters* **61,** 2015–2018 (Oct. 1988).

5. Kane, C. L. & Mele, E. J. Quantum Spin Hall Effect in Graphene. *Physical Review Letters* **95,** 226801 (Nov. 2005).

6. Fu, L., Kane, C. L. & Mele, E. J. Topological Insulators in Three Dimensions. *Physical Review Letters* **98,** 106803 (Mar. 2007).

7. Xia, Y., Qian, D., Hsieh, D., Wray, L., Pal, A., Lin, H., Bansil, A., Grauer, D., Hor, Y. S., Cava, R. J. & Hasan, M. Z. Observation of a large-gap topological-insulator class with a single Dirac cone on the surface. en. *Nature Physics* **5,** 398–402. ISSN: 1745-2473 (June 2009).

8. Hsieh, D., Xia, Y., Qian, D., Wray, L., Meier, F., Dil, J. H., Osterwalder, J., Patthey, L., Fedorov, A. V., Lin, H., Bansil, A., Grauer, D., Hor, Y. S., Cava, R. J. & Hasan, M. Z. Observation of Time-Reversal-Protected Single-Dirac-Cone Topological-Insulator States in Bi_2Te_3 and Sb_2Te_3. *Physical Review Letters* **103,** 146401 (Sept. 2009).

9. Hsieh, D., Xia, Y., Wray, L., Qian, D., Pal, A., Dil, J. H., Osterwalder, J., Meier, F., Bihlmayer, G., Kane, C. L., Hor, Y. S., Cava, R. J. & Hasan, M. Z. Observation of Unconventional Quantum Spin Textures in Topological Insulators. en. *Science* **323,** 919–922. ISSN: 0036-8075, 1095-9203 (Feb. 2009).

10. König, M., Wiedmann, S., Brüne, C., Roth, A., Buhmann, H., Molenkamp, L. W., Qi, X.-L. & Zhang, S.-C. Quantum Spin Hall Insulator State in HgTe Quantum Wells. en. *Science* **318,** 766–770. ISSN: 0036-8075, 1095-9203 (Nov. 2007).

11. Dagotto, E. Complexity in Strongly Correlated Electronic Systems. en. *Science* **309,** 257–262. ISSN: 0036-8075, 1095-9203 (July 2005).

12. Bednorz, J. G. & Müller, K. A. Possible highTc superconductivity in the Ba- La- Cu- O system. *Zeitschrift für Physik B Condensed Matter* **64,** 189–193 (1986).

13. Keimer, B., Kivelson, S. A., Norman, M. R., Uchida, S. & Zaanen, J. From quantum matter to high-temperature superconductivity in copper oxides. en. *Nature* **518,** 179–186. ISSN: 0028-0836 (Feb. 2015).

14. Takahashi, H., Igawa, K., Arii, K., Kamihara, Y., Hirano, M. & Hosono, H. Superconductivity at 43 K in an iron-based layered compound $LaO_{1-x}F_xFeAs$. *Nature* **453,** 376–378 (2008).

15. Kamihara, Y., Hiramatsu, H., Hirano, M., Kawamura, R., Yanagi, H., Kamiya, T. & Hosono, H. Iron-based layered superconductor: LaOFeP. *Journal of the American Chemical Society* **128,** 10012–10013 (2006).

16. Kamihara, Y., Watanabe, T., Hirano, M. & Hosono, H. Iron-Based Layered Superconductor La O_{1-x} F_xFeAs (x= 0.05- 0.12) with T_c= 26 K. *Journal of the American Chemical Society* **130,** 3296–3297 (2008).

17. Ge, J.-F., Liu, Z.-L., Liu, C., Gao, C.-L., Qian, D., Xue, Q.-K., Liu, Y. & Jia, J.-F. Superconductivity above 100 K in single-layer FeSe films on doped SrTiO3. en. *Nature Materials* **14,** 285–289. ISSN: 1476-1122 (Mar. 2015).

18. Qazilbash, M. M., Hamlin, J. J., Baumbach, R. E., Zhang, L., Singh, D. J., Maple, M. B. & Basov, D. N. Electronic correlations in the iron pnictides. en. *Nature Physics* **5,** 647–650. ISSN: 1745-2473 (Sept. 2009).

19. Basov, D. N. & Chubukov, A. V. Manifesto for a higher Tc. *Nature Physics* **7,** 272–276 (2011).

20. Imada, M., Fujimori, A. & Tokura, Y. Metal-insulator transitions. *Reviews of Modern Physics* **70,** 1039–1263 (Oct. 1998).

21. Stewart, M. K., Liu, J., Kareev, M., Chakhalian, J. & Basov, D. N. Mott Physics near the Insulator-To-Metal Transition in $NdNiO_3$. *Physical Review Letters* **107,** 176401 (Oct. 2011).

22. Park, H., Millis, A. J. & Marianetti, C. A. Site-Selective Mott Transition in Rare-Earth-Element Nickelates. *Physical Review Letters* **109,** 156402 (Oct. 2012).

23. Upton, M., Choi, Y., Park, H., Liu, J., Meyers, D., Chakhalian, J., Middey, S., Kim, J.-W. & Ryan, P. J. Novel Electronic Behavior Driving $NdNiO_3$ Metal-Insulator Transition. *Physical Review Letters* **115,** 036401 (July 2015).

24. Lee, S., Chen, R. & Balents, L. Landau Theory of Charge and Spin Ordering in the Nickelates. *Physical Review Letters* **106,** 016405 (Jan. 2011).

25. Middey, S., Chakhalian, J., Mahadevan, P., Freeland, J. W., Millis, A. J. & Sarma, D. D. Physics of Ultrathin Films and Heterostructures of Rare-Earth Nickelates. *Annual Review of Materials Research* **46,** 305–334 (2016).

26. Hansmann, P., Yang, X., Toschi, A., Khaliullin, G., Andersen, O. K. & Held, K. Turning a Nickelate Fermi Surface into a Cupratelike One through Heterostructuring. *Physical Review Letters* **103,** 016401 (June 2009).

27. Xiao, D., Zhu, W., Ran, Y., Nagaosa, N. & Okamoto, S. Interface engineering of quantum Hall effects in digital transition metal oxide heterostructures. en. *Nature Communications* **2,** ncomms1602. ISSN: 2041-1723 (Dec. 2011).

28. Wang, F. & Ran, Y. Nearly flat band with Chern number $C=2$ on the dice lattice. *Physical Review B* **84,** 241103 (Dec. 2011).

29. McLeod, A. S., van Heumen, E., Ramirez, J. G., Wang, S., Saerbeck, T., Guenon, S., Goldflam, M., Anderegg, L., Kelly, P., Mueller, A., Liu, M. K., Schuller, I. K. & Basov, D. N. Nanotextured phase coexistence in the correlated insulator V2O3. en. *Nature Physics* **13,** 80–86. ISSN: 1745-2473 (Jan. 2017).

30. Qazilbash, M. M., Brehm, M., Chae, B.-G., Ho, P.-C., Andreev, G. O., Kim, B.-J., Yun, S. J., Balatsky, A. V., Maple, M. B., Keilmann, F., Kim, H.-T. & Basov, D. N. Mott Transition in VO2 Revealed by Infrared Spectroscopy and Nano-Imaging. en. *Science* **318,** 1750–1753. ISSN: 0036-8075, 1095-9203 (Dec. 2007).

31. Bernevig, B. A. & Zhang, S.-C. Quantum Spin Hall Effect. *Physical Review Letters* **96,** 106802 (Mar. 2006).

32. Fu, L. & Kane, C. L. Superconducting Proximity Effect and Majorana Fermions at the Surface of a Topological Insulator. *Physical Review Letters* **100,** 096407 (Mar. 2008).

33. Hsieh, D., Qian, D., Wray, L., Xia, Y., Hor, Y. S., Cava, R. J. & Hasan, M. Z. A topological Dirac insulator in a quantum spin Hall phase. en. *Nature* **452,** 970–974. ISSN: 0028-0836 (Apr. 2008).

34. Chen, Y. L., Analytis, J. G., Chu, J.-H., Liu, Z. K., Mo, S.-K., Qi, X.-L., Zhang, H. J., Lu, D. H., Dai, X., Fang, Z. & others. Experimental realization of a three-dimensional topological insulator, Bi_2Te_3. *Science* **325,** 178–181 (2009).

35. Alpichshev, Z., Analytis, J. G., Chu, J.-H., Fisher, I. R., Chen, Y. L., Shen, Z. X., Fang, A. & Kapitulnik, A. STM Imaging of Electronic Waves on the Surface of Bi_2Te_3: Topologically Protected Surface States and Hexagonal Warping Effects. *Physical Review Letters* **104,** 016401 (Jan. 2010).

36. Zhang, H., Liu, C.-X., Qi, X.-L., Dai, X., Fang, Z. & Zhang, S.-C. Topological insulators in Bi_2Se_3, Bi_2Te_3 and Sb_2Te_3 with a single Dirac cone on the surface. *Nature physics* **5,** 438–442 (2009).

37. Horák, J., Stary, Z., Lošt'ák, P. & Pancíř, J. Anti-site defects in n-Bi2Se3 crystals. *Journal of Physics and Chemistry of Solids* **51,** 1353–1360 (1990).

38. Brahlek, M., Kim, Y. S., Bansal, N., Edrey, E. & Oh, S. Surface versus bulk state in topological insulator Bi_2Se_3 under environmental disorder. *Applied Physics Letters* **99,** 012109 (2011).

39. Bansal, N., Kim, Y. S., Brahlek, M., Edrey, E. & Oh, S. Thickness-independent transport channels in topological insulator Bi_2Se_3 thin films. *Physical review letters* **109,** 116804 (2012).

40. He, L., Xiu, F., Wang, Y., Fedorov, A. V., Huang, G., Kou, X., Lang, M., Beyermann, W. P., Zou, J. & Wang, K. L. Epitaxial growth of Bi2Se3 topological insulator thin films on Si (111). *Journal of Applied Physics* **109,** 103702 (2011).

41. Kou, X. F., He, L., Xiu, F. X., Lang, M. R., Liao, Z. M., Wang, Y., Fedorov, A. V., Yu, X. X., Tang, J. S., Huang, G. & others. Epitaxial growth of high mobility Bi 2 Se 3 thin films on CdS. *Applied Physics Letters* **98,** 242102 (2011).

42. He, L., Xiu, F., Yu, X., Teague, M., Jiang, W., Fan, Y., Kou, X., Lang, M., Wang, Y., Huang, G. & others. Surface-dominated conduction in a 6 nm thick Bi2Se3 thin film. *Nano letters* **12,** 1486–1490 (2012).

43. Lang, M., He, L., Kou, X., Upadhyaya, P., Fan, Y., Chu, H., Jiang, Y., Bardarson, J. H., Jiang, W., Choi, E. S. & others. Competing weak localization and weak antilocalization in ultrathin topological insulators. *Nano letters* **13,** 48–53 (2012).

44. Kim, Y. S., Brahlek, M., Bansal, N., Edrey, E., Kapilevich, G. A., Iida, K., Tanimura, M., Horibe, Y., Cheong, S.-W. & Oh, S. Thickness-dependent bulk properties and weak antilocalization effect in topological insulator Bi_2Se_3. *Physical Review B* **84,** 073109 (2011).

45. LaForge, A. D., Frenzel, A., Pursley, B. C., Lin, T., Liu, X., Shi, J. & Basov, D. N. Optical characterization of Bi_2Se_3 in a magnetic field: Infrared evidence for magnetoelectric coupling in a topological insulator material. *Physical Review B* **81,** 125120 (2010).

46. Di Pietro, P., Vitucci, F. M., Nicoletti, D., Baldassarre, L., Calvani, P., Cava, R., Hor, Y. S., Schade, U. & Lupi, S. Optical conductivity of bismuth-based topological insulators. *Physical Review B* **86,** 045439 (2012).

47. Qazilbash, M. M., Schafgans, A. A., Burch, K. S., Yun, S. J., Chae, B. G., Kim, B. J., Kim, H.-T. & Basov, D. N. Electrodynamics of the vanadium oxides V O_2 and V_2O_3. *Physical Review B* **77,** 115121 (2008).

48. Tompkins, H. & Irene, E. A. *Handbook of ellipsometry* (2017) (William Andrew, 2005).

49. Burch, K. S., Stephens, J., Kawakami, R. K., Awschalom, D. D. & Basov, D. N. Ellipsometric study of the electronic structure of $Ga_{1-x}Mn_xAs$ and low-temperature GaAs. *Physical Review B* **70,** 205208 (2004).

50. Stewart, M. K., Chetry, K. B., Chapler, B., Qazilbash, M. M., Schafgans, A. A., Gupta, A., Tiwald, T. E. & Basov, D. N. Ellipsometric study of the electronic band structure of CrO_2 across the ferromagnetic transition. *Physical Review B* **79,** 144414 (2009).

51. Aguilar, R. V., Stier, A. V., Liu, W., Bilbro, L. S., George, D. K., Bansal, N., Wu, L., Cerne, J., Markelz, A. G., Oh, S. & others. Terahertz response and colossal Kerr rotation from the surface states of the topological insulator Bi_2Se_3. *Physical review letters* **108,** 087403 (2012).

52. Wu, L., Brahlek, M., Aguilar, R. V., Stier, A. V., Morris, C. M., Lubashevsky, Y., Bilbro, L. S., Bansal, N., Oh, S. & Armitage, N. P. A sudden collapse in the transport lifetime across the topological phase transition in $(Bi_{1-x}In_x)_2Se_3$. *Nature Physics* **9,** 410–414 (2013).

53. Basov, D. N. & Timusk, T. Electrodynamics of high-T c superconductors. *Reviews of modern physics* **77,** 721 (2005).

54. Basov, D. N., Averitt, R. D., van der Marel, D., Dressel, M. & Haule, K. Electrodynamics of correlated electron materials. *Reviews of Modern Physics* **83,** 471–541 (June 2011).

55. Yu, P. & Cardona, M. *Fundamentals of semiconductors: physics and materials properties* (2017) (Springer Science & Business Media, 2010).

56. Li, Z. & Carbotte, J. P. Hexagonal warping on optical conductivity of surface states in topological insulator Bi_2Te_3. *Physical Review B* **87,** 155416 (Apr. 2013).

57. Schafgans, A. A., Post, K. W., Taskin, A. A., Ando, Y., Qi, X.-L., Chapler, B. C. & Basov, D. N. Landau level spectroscopy of surface states in the topological insulator $Bi_{0.91}Sb_{0.09}$ via magneto-optics. *Physical Review B* **85,** 195440 (2012).

58. Tse, W.-K. & MacDonald, A. H. Giant magneto-optical Kerr effect and universal Faraday effect in thin-film topological insulators. *Physical review letters* **105,** 057401 (2010).

59. Maciejko, J., Qi, X.-L., Drew, H. D. & Zhang, S.-C. Topological quantization in units of the fine structure constant. *Physical review letters* **105,** 166803 (2010).

60. Bianchi, M., Hatch, R. C., Mi, J., Iversen, B. B. & Hofmann, P. Simultaneous Quantization of Bulk Conduction and Valence States through Adsorption of Nonmagnetic Impurities on Bi_2Se_3. *Physical Review Letters* **107,** 086802 (Aug. 2011).

61. King, P. D. C., Hatch, R. C., Bianchi, M., Ovsyannikov, R., Lupulescu, C., Landolt, G., Slomski, B., Dil, J. H., Guan, D., Mi, J. L. & others. Large tunable Rashba spin splitting of a two-dimensional electron gas in Bi 2 Se 3. *Physical Review Letters* **107,** 096802 (2011).

62. Bianchi, M., Guan, D., Bao, S., Mi, J., Iversen, B. B., King, P. D. C. & Hofmann, P. Coexistence of the topological state and a two-dimensional electron gas on the surface of Bi_2Se_3. en. *Nature Communications* **1,** ncomms1131. ISSN: 2041-1723 (Nov. 2010).

63. Bahramy, M. S., King, P. D. C., De La Torre, A., Chang, J., Shi, M., Patthey, L., Balakrishnan, G., Hofmann, P., Arita, R., Nagaosa, N. & others. Emergent quantum confinement at topological insulator surfaces. *arXiv preprint arXiv:1206.0564.* (2017) (2012).

64. Benia, H. M., Lin, C., Kern, K. & Ast, C. R. Reactive chemical doping of the Bi_2Se_3 topological insulator. *Physical Review Letters* **107,** 177602 (2011).

65. Kittel, C. *Introduction to solid state physics* (2017) (Wiley, 2005).

66. Analytis, J. G., Chu, J.-H., Chen, Y., Corredor, F., McDonald, R. D., Shen, Z. X. & Fisher, I. R. Bulk Fermi surface coexistence with Dirac surface state in

Bi_2Se_3: A comparison of photoemission and Shubnikov de Haas measurements. *Physical Review B* **81,** 205407 (May 2010).

67. Reijnders, A. A., Tian, Y., Sandilands, L. J., Pohl, G., Kivlichan, I. D., Zhao, S. F., Jia, S., Charles, M. E., Cava, R. J., Alidoust, N. & others. Optical evidence of surface state suppression in Bi-based topological insulators. *Physical Review B* **89,** 075138 (2014).

68. Akrap, A., Tran, M., Ubaldini, A., Teyssier, J., Giannini, E., Van Der Marel, D., Lerch, P. & Homes, C. C. Optical properties of Bi_2Se_2Te at ambient and high pressures. *Physical Review B* **86,** 235207 (2012).

69. Bernevig, B. A., Hughes, T. L. & Zhang, S.-C. Quantum spin Hall effect and topological phase transition in HgTe quantum wells. *Science* **314,** 1757–1761 (2006).

70. Kane, C. L. & Mele, E. J. Z_2 topological order and the quantum spin Hall effect. *Physical review letters* **95,** 146802 (2005).

71. Taskin, A. A. & Ando, Y. Quantum oscillations in a topological insulator $Bi_{1-x}Sb_x$. *Physical Review B* **80,** 085303 (2009).

72. Nishide, A., Taskin, A. A., Takeichi, Y., Okuda, T., Kakizaki, A., Hirahara, T., Nakatsuji, K., Komori, F., Ando, Y. & Matsuda, I. Direct mapping of the spin-filtered surface bands of a three-dimensional quantum spin Hall insulator. *Physical Review B* **81,** 041309 (2010).

73. Ando, Y. Topological Insulator Materials. *Journal of the Physical Society of Japan* **82,** 102001. ISSN: 0031-9015 (Sept. 2013).

74. Qi, X.-L. & Zhang, S.-C. Topological insulators and superconductors. *Reviews of Modern Physics* **83,** 1057–1110 (Oct. 2011).

75. Essin, A. M., Moore, J. E. & Vanderbilt, D. Magnetoelectric polarizability and axion electrodynamics in crystalline insulators. *Physical review letters* **102,** 146805 (2009).

76. Tse, W.-K. & MacDonald, A. H. Magneto-optical Faraday and Kerr effects in topological insulator films and in other layered quantized Hall systems. *Physical Review B* **84,** 205327 (2011).

77. Taskin, A. A., Ren, Z., Sasaki, S., Segawa, K. & Ando, Y. Observation of Dirac holes and electrons in a topological insulator. *Physical Review Letters* **107,** 016801 (2011).

78. Kim, D., Cho, S., Butch, N. P., Syers, P., Kirshenbaum, K., Adam, S., Paglione, J. & Fuhrer, M. S. Surface conduction of topological Dirac electrons in bulk insulating Bi_2Se_3. en. *Nature Physics* **8,** 459–463. ISSN: 1745-2473 (June 2012).

79. Ren, Z., Taskin, A. A., Sasaki, S., Segawa, K. & Ando, Y. Optimizing $Bi_{2-x}Sb_xTe_{3-y}Se_y$ solid solutions to approach the intrinsic topological insulator regime. *Physical Review B* **84,** 165311 (Oct. 2011).

80. Neupane, M., Xu, S.-Y., Wray, L. A., Petersen, A., Shankar, R., Alidoust, N., Liu, C., Fedorov, A., Ji, H., Allred, J. M., Hor, Y. S., Chang, T.-R., Jeng, H.-T., Lin, H., Bansil, A., Cava, R. J. & Hasan, M. Z. Topological surface states and Dirac point tuning in ternary topological insulators. *Physical Review B* **85,** 235406 (June 2012).

81. Jia, S., Beidenkopf, H., Drozdov, I., Fuccillo, M. K., Seo, J., Xiong, J., Ong, N. P., Yazdani, A. & Cava, R. J. Defects and high bulk resistivities in the Bi-rich tetradymite topological insulator $Bi_{2+x}Te_{2-x}Se$. *Physical Review B* **86,** 165119 (Oct. 2012).

82. Dressel, M. & Grüner, G. *Electrodynamics of Solids: Optical Properties of Electrons in Matter* en. ISBN: 978-0-521-59726-5 (Cambridge University Press, Jan. 2002).

83. Ren, Z., Taskin, A. A., Sasaki, S., Segawa, K. & Ando, Y. Large bulk resistivity and surface quantum oscillations in the topological insulator Bi_2Te_2Se. *Physical Review B* **82,** 241306 (Dec. 2010).

84. Lautenschlager, P., Garriga, M., Logothetidis, S. & Cardona, M. Interband critical points of GaAs and their temperature dependence. *Physical Review B* **35,** 9174–9189 (June 1987).

85. Arakane, T., Sato, T., Souma, S., Kosaka, K., Nakayama, K., Komatsu, M., Takahashi, T., Ren, Z., Segawa, K. & Ando, Y. Tunable Dirac cone in the topological insulator $Bi_{2-x}Sb_xTe_{3-y}Se_y$. en. *Nature Communications* **3,** ncomms1639. ISSN: 2041-1723 (Jan. 2012).

86. Jenkins, G. S., Sushkov, A. B., Schmadel, D. C., Butch, N. P., Syers, P., Paglione, J. & Drew, H. D. Terahertz Kerr and reflectivity measurements on the topological insulator Bi_2Se_3. *Physical Review B* **82,** 125120 (Sept. 2010).

87. Valdés Aguilar, R., Stier, A. V., Liu, W., Bilbro, L. S., George, D. K., Bansal, N., Wu, L., Cerne, J., Markelz, A. G., Oh, S. & Armitage, N. P. Terahertz Response and Colossal Kerr Rotation from the Surface States of the Topological Insulator Bi_2Se_3. *Physical Review Letters* **108,** 087403 (Feb. 2012).

88. Palik, E. D. & Furdyna, J. K. Infrared and microwave magnetoplasma effects in semiconductors. en. *Reports on Progress in Physics* **33,** 1193. ISSN: 0034-4885 (1970).

89. Liu, C.-X., Qi, X.-L., Zhang, H., Dai, X., Fang, Z. & Zhang, S.-C. Model Hamiltonian for topological insulators. *Physical Review B* **82,** 045122 (July 2010).

90. Cheng, P., Song, C., Zhang, T., Zhang, Y., Wang, Y., Jia, J.-F., Wang, J., Wang, Y., Zhu, B.-F., Chen, X., Ma, X., He, K., Wang, L., Dai, X., Fang, Z., Xie, X., Qi, X.-L., Liu, C.-X., Zhang, S.-C. & Xue, Q.-K. Landau Quantization of Topological Surface States in Bi_2Se_3. *Physical Review Letters* **105,** 076801 (Aug. 2010).

91. Johnston, D. C. The puzzle of high temperature superconductivity in layered iron pnictides and chalcogenides. *Advances in Physics* **59,** 803–1061 (2010).

92. Qi, X.-L., Li, R., Zang, J. & Zhang, S.-C. Inducing a Magnetic Monopole with Topological Surface States. en. *Science* **323,** 1184–1187. ISSN: 0036-8075, 1095-9203 (Feb. 2009).

93. Butch, N. P., Kirshenbaum, K., Syers, P., Sushkov, A. B., Jenkins, G. S., Drew, H. D. & Paglione, J. Strong surface scattering in ultrahigh-mobility Bi_2Se_3 topological insulator crystals. *Physical Review B* **81,** 241301 (June 2010).

94. Basov, D., Fogler, M., Lanzara, A., Wang, F. & Zhang, Y. Colloquium: Graphene spectroscopy. *Reviews of Modern Physics* **86,** 959–994 (July 2014).

95. Castro Neto, A. H., Guinea, F., Peres, N. M. R., Novoselov, K. S. & Geim, A. K. The electronic properties of graphene. *Reviews of Modern Physics* **81,** 109–162 (Jan. 2009).

96. Xu, S.-Y., Neupane, M., Liu, C., Zhang, D., Richardella, A., Andrew Wray, L., Alidoust, N., Leandersson, M., Balasubramanian, T., Sánchez-Barriga, J., Rader, O., Landolt, G., Slomski, B., Hugo Dil, J., Osterwalder, J., Chang, T.-R., Jeng, H.-T., Lin, H., Bansil, A., Samarth, N. & Zahid Hasan, M. Hedgehog spin texture and Berry/'s phase tuning in a magnetic topological insulator. en. *Nature Physics* **8,** 616–622. ISSN: 1745-2473 (Aug. 2012).

97. Hashibon, A. & Elsässer, C. First-principles density functional theory study of native point defects in Bi_2Te_3. *Physical Review B* **84,** 144117 (Oct. 2011).

98. Chapler, B. C., Post, K. W., Richardella, A. R., Lee, J. S., Tao, J., Samarth, N. & Basov, D. N. Infrared electrodynamics and ferromagnetism in the topological

semiconductors Bi_2Te_3 and Mn-doped Bi_2Te_3. *Physical Review B* **89,** 235308 (June 2014).

99. Jiang, Y., Sun, Y. Y., Chen, M., Wang, Y., Li, Z., Song, C., He, K., Wang, L., Chen, X., Xue, Q.-K., Ma, X. & Zhang, S. B. Fermi-Level Tuning of Epitaxial Sb_2Te_3 Thin Films on Graphene by Regulating Intrinsic Defects and Substrate Transfer Doping. *Physical Review Letters* **108,** 066809 (Feb. 2012).

100. Kong, D., Chen, Y., Cha, J. J., Zhang, Q., Analytis, J. G., Lai, K., Liu, Z., Hong, S. S., Koski, K. J., Mo, S.-K., Hussain, Z., Fisher, I. R., Shen, Z.-X. & Cui, Y. Ambipolar field effect in the ternary topological insulator $(Bi_xSb_{1-x})_2Te_3$ by composition tuning. en. *Nature Nanotechnology* **6,** 705–709. ISSN: 1748-3387 (Nov. 2011).

101. Zhang, J., Chang, C.-Z., Zhang, Z., Wen, J., Feng, X., Li, K., Liu, M., He, K., Wang, L., Chen, X., Xue, Q.-K., Ma, X. & Wang, Y. Band structure engineering in $(Bi_{1-x}Sb_x)_2Te_3$ ternary topological insulators. en. *Nature Communications* **2,** ncomms1588. ISSN: 2041-1723 (Dec. 2011).

102. Sabio, J., Nilsson, J. & Castro Neto, A. H. f-sum rule and unconventional spectral weight transfer in graphene. *Physical Review B* **78,** 075410 (Aug. 2008).

103. Gusynin, V. P., Sharapov, S. G. & Carbotte, J. P. Sum rules for the optical and Hall conductivity in graphene. *Physical Review B* **75,** 165407 (Apr. 2007).

104. Tang, C. S., Xia, B., Zou, X., Chen, S., Ou, H.-W., Wang, L., Rusydi, A., Zhu, J.-X. & Chia, E. E. M. Terahertz conductivity of topological surface states in $Bi_{1.5}Sb_{0.5}Te_{1.8}Se_{1.2}$. en. *Scientific Reports* **3,** srep03513. ISSN: 2045-2322 (Dec. 2013).

105. Wu, L., Tse, W.-K., Brahlek, M., Morris, C. M., Aguilar, R. V., Koirala, N., Oh, S. & Armitage, N. P. High-Resolution Faraday Rotation and Electron-Phonon Coupling in Surface States of the Bulk-Insulating Topological Insulator $Cu_{0.02}Bi_2Se_3$. *Physical Review Letters* **115.** ISSN: 0031-9007, 1079-7114. (2017) (Nov. 2015).

106. Kulbachinskii, V. A., Dashevskii, Z. M., Inoue, M., Sasaki, M., Negishi, H., Gao, W. X., Lostak, P., Horak, J. & de Visser, A. Valence-band changes in $Sb_{2-x}In_xTe_3$ by transport and Shubnikov-de Haas effect measurements. *Physical Review B* **52,** 10915–10922 (Oct. 1995).

107. Kulbachinskii, V. A., Kytin, V. G., Tarasov, P. M. & Yuzeeva, N. A. Anomalous increase of the thermopower and thermoelectric figure of merit in Ga-doped p-$(Bi_{0.5}Sb_{0.5})_2Te_3$ single crystals. en. *Physics of the Solid State* **52,** 1830–1835. ISSN: 1063-7834, 1090-6460 (Sept. 2010).

108. Garate, I. & Glazman, L. Weak localization and antilocalization in topological insulator thin films with coherent bulk-surface coupling. *Physical Review B* **86,** 035422 (July 2012).

109. Li, Z. Q., Henriksen, E. A., Jiang, Z., Hao, Z., Martin, M. C., Kim, P., Stormer, H. L. & Basov, D. N. Dirac charge dynamics in graphene by infrared spectroscopy. en. *Nature Physics* **4,** 532–535. ISSN: 1745-2473 (July 2008).

110. Horng, J., Chen, C.-F., Geng, B., Girit, C., Zhang, Y., Hao, Z., Bechtel, H. A., Martin, M., Zettl, A., Crommie, M. F., Shen, Y. R. & Wang, F. Drude conductivity of Dirac fermions in graphene. *Physical Review B* **83,** 165113 (Apr. 2011).

111. Jenkins, G. S., Schmadel, D. C., Sushkov, A. B., Drew, H. D., Bichler, M., Koblmueller, G., Brahlek, M., Bansal, N. & Oh, S. Dirac cone shift of a passivated topological Bi_2Se_3 interface state. *Physical Review B* **87,** 155126 (Apr. 2013).

112. Wunsch, B., Stauber, T., Sols, F. & Guinea, F. Dynamical polarization of graphene at finite doping. en. *New Journal of Physics* **8,** 318. ISSN: 1367-2630 (2006).

113. Richter, W. & Becker, C. R. A Raman and far-infrared investigation of phonons in the rhombohedral V2–VI3 compounds Bi_2Te_3, Bi_2Se_3, Sb_2Te_3 and $Bi_2(Te_{1-x}Se_x)_3$ ($0 < x < 1$), $(Bi_{1-y}Sb_y)_2Te_3$ ($0 < y < 1$). en. *physica status solidi (b)* **84,** 619–628. ISSN: 1521-3951 (Dec. 1977).

114. Kuzmenko, A. B. Kramers–Kronig constrained variational analysis of optical spectra. *Review of Scientific Instruments* **76,** 083108. ISSN: 0034-6748 (July 2005).

115. Averitt, R. D. & Taylor, A. J. Ultrafast optical and far-infrared quasiparticle dynamics in correlated electron materials. en. *Journal of Physics: Condensed Matter* **14,** R1357. ISSN: 0953-8984 (2002).

116. Post, K. W., Lee, Y. S., Chapler, B. C., Schafgans, A. A., Novak, M., Taskin, A. A., Segawa, K., Goldflam, M. D., Stinson, H. T., Ando, Y. & Basov, D. N. Infrared probe of the bulk insulating response in $Bi_{2-x}Sb_xTe_{3-y}Se_y$ topological insulator alloys. *Physical Review B* **91,** 165202 (Apr. 2015).

117. Pandey, A., Ueland, B. G., Yeninas, S., Kreyssig, A., Sapkota, A., Zhao, Y., Helton, J. S., Lynn, J. W., McQueeney, R. J., Furukawa, Y., Goldman, A. I. & Johnston, D. C. Coexistence of Half-Metallic Itinerant Ferromagnetism with Local-Moment Antiferromagnetism in $Ba_{0.60}K_{0.40}Mn_2As_2$. *Physical Review Letters* **111,** 047001 (July 2013).

118. Pandey, A., Anand, V. K. & Johnston, D. C. Large miscibility gap in the $Ba(Mn_xFe_{1-x})As_2$ system. *Physical Review B* **84,** 014405 (July 2011).

119. Satya, A. T., Mani, A., Arulraj, A., Shekar, N. V. C., Vinod, K., Sundar, C. S. & Bharathi, A. Pressure-induced metallization of BaMn${}_{2}$As${}_{2}$. *Physical Review B* **84,** 180515 (Nov. 2011).

120. Simonson, J. W., Smith, G. J., Post, K., Pezzoli, M., Kistner-Morris, J. J., McNally, D. E., Hassinger, J. E., Nelson, C. S., Kotliar, G., Basov, D. N. & Aronson, M. C. Magnetic and structural phase diagram of $CaMn_2Sb_2$. *Physical Review B* **86,** 184430 (Nov. 2012).

121. Simonson, J. W., Post, K., Marques, C., Smith, G., Khatib, O., Basov, D. N. & Aronson, M. C. Gap states in insulating LaMnPO 1- x F x (x= 0–0.3). *Physical Review B* **84,** 165129 (2011).

122. Sun, Y.-L., Bao, J.-K., Luo, Y.-K., Feng, C.-M., Xu, Z.-A. & Cao, G.-H. Insulator-to-metal transition and large thermoelectric effect in La1- xSrxMnAsO. *EPL (Europhysics Letters)* **98,** 17009 (2012).

123. Jungwirth, T., Novák, V., Martí, X., Cukr, M., Máca, F., Shick, A. B., Mašek, J., Horodyská, P., Němec, P., Holỳ, V. & others. Demonstration of molecular beam epitaxy and a semiconducting band structure for I-Mn-V compounds. *Physical Review B* **83,** 035321 (2011).

124. Johnston, D. C., McQueeney, R. J., Lake, B., Honecker, A., Zhitomirsky, M. E., Nath, R., Furukawa, Y., Antropov, V. P. & Singh, Y. Magnetic exchange interactions in BaMn 2 As 2: A case study of the J 1-J 2-J c Heisenberg model. *Physical Review B* **84,** 094445 (2011).

125. Cheng, J.-G., Matsubayashi, K., Wu, W., Sun, J. P., Lin, F. K., Luo, J. L. & Uwatoko, Y. Pressure induced superconductivity on the border of magnetic order in MnP. *Physical review letters* **114,** 117001 (2015).

126. Georges, A., Medici, L. d. & Mravlje, J. Strong correlations from Hund's coupling. *Annu. Rev. Condens. Matter Phys.* **4,** 137–178 (2013).

127. McNally, D. E., Simonson, J. W., Post, K. W., Yin, Z. P., Pezzoli, M., Smith, G. J., Leyva, V., Marques, C., DeBeer-Schmitt, L., Kolesnikov, A. I. & others. Origin of the charge gap in LaMnPO. *Physical Review B* **90,** 180403 (2014).

128. Simonson, J. W., Yin, Z. P., Pezzoli, M., Guo, J., Liu, J., Post, K., Efimenko, A., Hollmann, N., Hu, Z., Lin, H.-J., Chen, C.-T., Marques, C., Leyva, V., Smith, G., Lynn, J. W., Sun, L. L., Kotliar, G., Basov, D. N., Tjeng, L. H. & Aronson, M. C. From antiferromagnetic insulator to correlated metal in

pressurized and doped LaMnPO. en. *Proceedings of the National Academy of Sciences* **109,** E1815–E1819. ISSN: 0027-8424, 1091-6490 (July 2012).

129. Guo, J., Simonson, J. W., Sun, L., Wu, Q., Gao, P., Zhang, C., Gu, D., Kotliar, G., Aronson, M. & Zhao, Z. Observation of antiferromagnetic order collapse in the pressurized insulator LaMnPO. *arXiv preprint arXiv:1305.5426.* (2017) (2013).

130. Katsidis, C. C. & Siapkas, D. I. General transfer-matrix method for optical multilayer systems with coherent, partially coherent, and incoherent interference. *Applied optics* **41,** 3978–3987 (2002).

131. Comanac, A., de'Medici, L., Capone, M. & Millis, A. J. Optical conductivity and the correlation strength of high-temperature copper-oxide superconductors. *Nature Physics* **4,** 287–290 (2008).

132. Kotliar, G. & Vollhardt, D. Strongly correlated materials: Insights from dynamical mean-field theory. *Physics Today* **57,** 53–59 (2004).

133. Goncharov, A. F., Struzhkin, V. V., Hemley, R. J., Mao, H. K. & Liu, Z. Science and Technology of High Pressure (2000).

134. De'Medici, L., Giovannetti, G. & Capone, M. Selective Mott Physics as a Key to Iron Superconductors. *Physical Review Letters* **112,** 177001 (Apr. 2014).

135. Qazilbash, M. M., Brehm, M., Andreev, G. O., Frenzel, A., Ho, P.-C., Chae, B.-G., Kim, B.-J., Yun, S. J., Kim, H.-T., Balatsky, A. V., Shpyrko, O. G., Maple, M. B., Keilmann, F. & Basov, D. N. Infrared spectroscopy and nano-imaging of the insulator-to-metal transition in vanadium dioxide. *Physical Review B* **79,** 075107 (Feb. 2009).

136. De'Medici, L. Hund's coupling and its key role in tuning multiorbital correlations. *Physical Review B* **83,** 205112 (May 2011).

137. De'Medici, L., Hassan, S. R., Capone, M. & Dai, X. Orbital-Selective Mott Transition out of Band Degeneracy Lifting. *Physical Review Letters* **102,** 126401 (Mar. 2009).

138. Yin, Z. P., Haule, K. & Kotliar, G. Kinetic frustration and the nature of the magnetic and paramagnetic states in iron pnictides and iron chalcogenides. en. *Nature Materials* **10,** 932–935. ISSN: 1476-1122 (Dec. 2011).

139. Blaha, P., Schwarz, K., Madsen, G. K. H., Kvasnicka, D. & Luitz, J. wien2k. *An augmented plane wave+ local orbitals program for calculating crystal properties.* (2017) (2001).

140. Perdew, J. P., Burke, K. & Ernzerhof, M. Generalized Gradient Approximation Made Simple. *Physical Review Letters* **77,** 3865–3868 (Oct. 1996).

141. Kotliar, G., Savrasov, S. Y., Haule, K., Oudovenko, V. S., Parcollet, O. & Marianetti, C. A. Electronic structure calculations with dynamical mean-field theory. *Reviews of Modern Physics* **78,** 865–951 (Aug. 2006).

142. Haule, K., Yee, C.-H. & Kim, K. Dynamical mean-field theory within the full-potential methods: Electronic structure of $CeCoIn_5$ and $CeRhIn_5$. *Physical Review B* **81,** 195107 (May 2010).

143. Haule, K. Quantum Monte Carlo impurity solver for cluster dynamical mean-field theory and electronic structure calculations with adjustable cluster base. *Physical Review B* **75,** 155113 (Apr. 2007).

144. Werner, P., Comanac, A., de'Medici, L., Troyer, M. & Millis, A. J. Continuous-Time Solver for Quantum Impurity Models. *Physical Review Letters* **97,** 076405 (Aug. 2006).

145. Stadler, K., Yin, Z., von Delft, J., Kotliar, G. & Weichselbaum, A. Dynamical Mean-Field Theory Plus Numerical Renormalization-Group Study of Spin-Orbital Separation in a Three-Band Hund Metal. *Physical Review Letters* **115,** 136401 (Sept. 2015).

146. Medarde, M. L. Structural, magnetic and electronic properties of perovskites (R = rare earth). *Journal of Physics: Condensed Matter* **9,** 1679–1707. ISSN: 0953-8984, 1361-648X (Feb. 1997).

147. Catalan, G. Progress in perovskite nickelate research. en. *Phase Transitions* **81,** 729–749. ISSN: 0141-1594, 1029-0338 (July 2008).

148. Johnston, S., Mukherjee, A., Elfimov, I., Berciu, M. & Sawatzky, G. A. Charge Disproportionation without Charge Transfer in the Rare-Earth-Element Nickelates as a Possible Mechanism for the Metal-Insulator Transition. *Physical Review Letters* **112,** 106404 (Mar. 2014).

149. Mandal, B., Sarkar, S., Pandey, S. K., Mahadevan, P., Franchini, C., Millis, A. J. & Sarma, D. D. The driving force for charge ordering in rare earth nickelates. *arXiv:1701.06819 [cond-mat].* (2017) (Jan. 2017).

150. Liu, M. K., Wagner, M., Abreu, E., Kittiwatanakul, S., McLeod, A., Fei, Z., Goldflam, M., Dai, S., Fogler, M. M., Lu, J., Wolf, S. A., Averitt, R. D. & Basov, D. N. Anisotropic Electronic State via Spontaneous Phase Separation in Strained Vanadium Dioxide Films. *Physical Review Letters* **111,** 096602 (Aug. 2013).

151. Liu, M., Wagner, M., Zhang, J., McLeod, A., Kittiwatanakul, S., Fei, Z., Abreu, E., Goldflam, M., Sternbach, A. J., Dai, S. & others. Symmetry breaking and geometric confinement in VO2: Results from a three-dimensional infrared nano-imaging. *Applied Physics Letters* **104,** 121905 (2014).

152. Liu, S., Phillabaum, B., Carlson, E., Dahmen, K., Vidhyadhiraja, N., Qazilbash, M. & Basov, D. Random Field Driven Spatial Complexity at the Mott Transition in ${\mathrm{VO}}_{2}$. *Physical Review Letters* **116,** 036401 (Jan. 2016).

153. Phillabaum, B., Carlson, E. W. & Dahmen, K. A. Spatial complexity due to bulk electronic nematicity in a superconducting underdoped cuprate. en. *Nature Communications* **3,** 915. ISSN: 2041-1723 (June 2012).

154. Perković, O., Dahmen, K. & Sethna, J. P. Avalanches, Barkhausen Noise, and Plain Old Criticality. *Physical Review Letters* **75,** 4528–4531 (Dec. 1995).

155. Zachar, O., Kivelson, S. A. & Emery, V. J. Landau theory of stripe phases in cuprates and nickelates. *Physical Review B* **57,** 1422–1426 (Jan. 1998).

156. Catalan, G., Seidel, J., Ramesh, R. & Scott, J. F. Domain wall nanoelectronics. *Reviews of Modern Physics* **84,** 119–156 (Feb. 2012).

157. Caviglia, A. D., Gariglio, S., Reyren, N., Jaccard, D., Schneider, T., Gabay, M., Thiel, S., Hammerl, G., Mannhart, J. & Triscone, J.-M. Electric field control of the LaAlO3/SrTiO3 interface ground state. en. *Nature* **456,** 624–627. ISSN: 0028-0836 (Dec. 2008).

158. Ohtomo, A. & Hwang, H. Y. A high-mobility electron gas at the LaAlO3/SrTiO3 heterointerface. en. *Nature* **427,** 423–426. ISSN: 0028-0836 (Jan. 2004).

159. Reyren, N., Thiel, S., Caviglia, A. D., Kourkoutis, L. F., Hammerl, G., Richter, C., Schneider, C. W., Kopp, T., Rüetschi, A.-S., Jaccard, D., Gabay, M., Muller, D. A., Triscone, J.-M. & Mannhart, J. Superconducting Interfaces Between Insulating Oxides. en. *Science* **317,** 1196–1199. ISSN: 0036-8075, 1095-9203 (Aug. 2007).

160. Valencia, S., Crassous, A., Bocher, L., Garcia, V., Moya, X., Cherifi, R. O., Deranlot, C., Bouzehouane, K., Fusil, S., Zobelli, A., Gloter, A., Mathur, N. D., Gaupp, A., Abrudan, R., Radu, F., Barthélémy, A. & Bibes, M. Interface-induced room-temperature multiferroicity in BaTiO3. en. *Nature Materials* **10,** 753–758. ISSN: 1476-1122 (Oct. 2011).

161. Ma, E. Y., Cui, Y.-T., Ueda, K., Tang, S., Chen, K., Tamura, N., Wu, P. M., Fujioka, J., Tokura, Y. & Shen, Z.-X. Mobile metallic domain walls in an

all-in-all-out magnetic insulator. en. *Science* **350,** 538–541. ISSN: 0036-8075, 1095-9203 (Oct. 2015).

162. Seidel, J., Martin, L. W., He, Q., Zhan, Q., Chu, Y.-H., Rother, A., Hawkridge, M. E., Maksymovych, P., Yu, P., Gajek, M., Balke, N., Kalinin, S. V., Gemming, S., Wang, F., Catalan, G., Scott, J. F., Spaldin, N. A., Orenstein, J. & Ramesh, R. Conduction at domain walls in oxide multiferroics. en. *Nature Materials* **8,** 229–234. ISSN: 1476-1122 (Mar. 2009).

163. Yamaji, Y. & Imada, M. Modulated helical metals at magnetic domain walls of pyrochlore iridium oxides. *Physical Review B* **93,** 195146 (May 2016).

164. Yamaji, Y. & Imada, M. Metallic Interface Emerging at Magnetic Domain Wall of Antiferromagnetic Insulator: Fate of Extinct Weyl Electrons. *Physical Review X* **4,** 021035 (May 2014).

165. Mattoni, G., Zubko, P., Maccherozzi, F., van der Torren, A., Boltje, D. B., Hadjimichael, M., Manca, N., Catalano, S., Gibert, M., Liu, Y., Aarts, J., Triscone, J.-M., Dhesi, S. S. & Caviglia, A. D. Striped nanoscale phase separation at the metal–insulator transition of heteroepitaxial nickelates. *Nature Communications* **7.** ISSN: 2041-1723. (2017) (Nov. 2016).